6-23-2015

Theory, Multiscale Simulations, and Experiments on Mesoscale Multifunctional Systems

Lance Edward Edens

Lance Edward Edens
Candidate

Chemistry and Chemical Biology
Department

This dissertation is approved, and it is acceptable in quality and form for publication:

Approved by the Dissertation Committee:

Dr. David J. Keller, Chairperson

Dr. Stephen E. Cabaniss

Dr. Hua Guo

Dr. James A. Brozik

Dr. David G. Whitten

THEORY, MULTISCALE SIMULATIONS, AND EXPERIMENTS ON MESOSCALE MULTIFUNCTIONAL SYSTEMS

by

LANCE EDWARD EDENS

B.S. Astrophysics, University of New Mexico, 2006

DISSERTATION

Submitted in Partial Fulfillment of the
Requirements for the Degree of

Doctor of Philosophy

Chemistry

The University of New Mexico
Albuquerque, New Mexico

May, 2015

ACKNOWLEDGEMENTS

I would like to thank my advisor, Dr. David Keller, for his knowledge, guidance, patience, and throughout my graduate program. I would also like to thank Dr. James Brozik for convincing me to start work in physical chemistry. I wish to thank Dr. David Whitten for allowing me to work with him and his group. To Dr. Stephen Cabaniss and Dr. Hua Guo, I would like to express my sincere gratitude for being a part of my committee.

This research received support from the Defense Threat Reduction Agency-Joint Science and Technology Office for Chemical and Biological Defense (Grant number HDTRA1-11-1-0004). In addition, many people made this work possible. I am very grateful to Dr. Ying Wang for his help and collaboration on many projects, to Dr. Linnea Ista for her help with understanding bacteria, and to Harry Pappas for sharing his reports and unpublished data. I also wish to acknowledge current and former members of the Whitten Group, including Dr. Liping Ding, Dr. Tom Corbitt, Dr. Eric Hill, Dr. Eunkyung Ji, Dr. Yanli Tang, Dr. Zhijun Zhou, and Patrick Donabedian.

I would like to thank Dr. Kirk Schanze and his synthesis team at the University of Florida, especially Dr. Katsu Ogawa, Dr. Anand Parthasarathy, and Samantha Phan for all their work. And I would like to extend a thank you to Dr. Gabriel López and Dr. Qian Yu for their work with the patterned samples.

I appreciate the assistance from Adam Goler, Adam Delora, and Chris Larson on the TM2 program. I wish to thank James Kaminski for his help in the lab. I am very grateful for the help Karen McElveny provided in navigating through the graduate program. And I thank Suhyun Yoon for continuing on with this research.

Last, but by no means least, I would like to thank my family for providing me with love and support all my life. To my mom, Debe, and my sister, Chelsea, this work would not exist without their help.

THEORY, MULTISCALE SIMULATIONS, AND EXPERIMENTS ON MESOSCALE MULTIFUNCTIONAL SYSTEMS

by

Lance Edens

B.S. in Astrophysics, University of New Mexico, 2006

Ph.D. Chemistry, University of New Mexico, 2015

ABSTRACT

Computational simulations use theoretical models to reproduce, as accurately as possible, the observed real-world behavior of complex structures. Guided by experimental observations, many multiscale/coarse-grained simulations seek to explore increasingly complicated systems. Here, a multiscale/coarse-grained simulation program (called TM2) is developed with applications to 1) properties and mechanisms of DNA and DNA polymerases, and 2) adhesion between whole bacterial cells and patterned surfaces. Results from the bacterial adhesion application form a part of a larger collaborative effort aimed at creating multifunctional, controllable surfaces to capture and kill pathogenic bacteria.

The application of TM2 is first demonstrated by a coarse-grained model for DNA where the qualitative properties of real B-form DNA arise naturally from local interactions. A preliminary model for small DNA polymerases was also developed which uses the medial axis transform concept to efficiently represent the protein body potential.

In another application of TM2, a program named PWA Simulator uses a general free energy functional to simulate the dynamic process of initial cellular attachment to a

patterned surface. Another related program (PWA Integrator) integrates a partition function to obtain the equilibrium potential of mean force between a bacterium and a surface.

PWA Simulator and PWA Integrator are part of a larger project to build materials with temperature-switchable adhesion properties to capture bacteria, and then to kill them using light-activated biocidal materials. Several deposition and characterization techniques are utilized to fabricate and define complex surfaces with both a temperature-switchable poly(N-isopropylacrylamide) (PNIPAAm) polymer and light-activated biocides (conjugated phenylene ethynylenes, OPEs and PPEs).

AFM images of *Escherichia coli* were able to resolve the physical structure of bacterial surfaces as they were exposed to OPEs and PPEs. The cells show noticeable surface morphology changes, suggesting that the materials directly disrupt outer membrane integrity. *Escherichia coli* and *Staphylococcus aureus* were also allowed to adhere to a mixed surface containing PNIPAAm and PPEs. AFM imaging revealed that these surfaces contain randomly mixed areas of both PNIPAAm and biocide. Biocidal testing showed that the addition of PNIPAAm does not decrease the surface's biocidal potency in the light, suggesting inactivation is caused by light-induced singlet oxygen generation.

TABLE OF CONTENTS

LIST OF FIGURES

LIST OF TABLES

Table Page

1. INTRODUCTION

1.1 Overview

Computational simulations utilize theoretical models to reproduce and help explain observed real-world behaviors of complex systems. In this dissertation, a multiscale/coarse-grained simulation program (called TM2) is developed with intent to provide a general system that can be utilized for a variety of applications. Movement in TM2 is simulated by Brownian dynamics without hydrodynamic coupling. Resolution is determined by variably sized "units" that interact via adjustable, phenomenological potentials that are not reliant on pre-determined force fields. To demonstrate the versatility of the program, two applications of TM2 are presented: 1) the properties and mechanisms of DNA and DNA polymerases, and 2) the adhesion between whole bacterial cells and patterned surfaces. Simulations of bacterial attachment form a part of a larger collaborative effort aimed at creating complex, controllable surfaces to capture and kill pathogenic bacteria.

For the first application of TM2, a DNA modeled from the base pair level is presented where the qualitative properties of real DNA arise naturally from local interactions. The model DNA forms stable, complementary double helices over long runs (~10 μs) at or near room temperature with structural parameters close to those of B-form DNA. Most regions where the bases are mispaired become disordered and long-range fluctuations and elastic properties are close to experimental values. A preliminary model for the DNA polymerase Human Immunodeficiency Virus Reverse Transcriptase (HIV RT) was also developed which uses the medial axis transform concept to efficiently

represent the protein body potential. This creates a reasonable and reproducible coarse-grained polymerase structure that roughly follows the solvent excluded surface of the original protein.

The second application of TM2 focuses on quantifying bacterial attachment as a function of surface composition and pattern in order to create a predictive model for both dynamic and equilibrium bacterial surface binding. A new program (PWA Simulator), derived from TM2, uses a general free energy functional for the interaction between a cell and a target surface to simulate the dynamic process of initial cellular attachment. Surface compositions are represented by fractional areas of pure materials whose surface attachment energies can be independently obtained through experiment. The potential of mean force for rotationally free cells is calculated and used to determine the equilibrium constant for cell-to-target attachment. A second, related program (PWA Integrator) calculates the equilibrium potential of mean force between a bacterium and a surface via rotational integration of a partition function. Direct comparison of bound cell concentration per unit area between the model and experimental results can further parameterize and refine the program.

The results above are part of a larger project to build materials with temperature-switchable adhesion properties to capture bacteria, and then to kill them using light-activated biocidal materials. Using layer-by-layer deposition, surface polymerization, and interferometric lithography, complex surfaces were fabricated that contain both temperature-switchable poly(N-isopropylacrylamide) (PNIPAAm) and biocidal polymers and oligomers with conjugated phenylene ethynylene backbones (OPEs and PPEs).

A combination of Atomic Force Microscopy (AFM), light microscopy, bacterial adhesion measurements, and bacterial live/dead assays were used to characterize the properties of these surfaces. AFM images of *Escherichia coli* were able to resolve the physical structure of bacterial surfaces. Bacteria exposed to OPEs and PPEs showed noticeable surface morphology changes, suggesting the materials directly disrupt outer membrane integrity. *Escherichia coli* and *Staphylococcus aureus* were also allowed to adhere to a mixed surface containing PNIPAAm and PPEs. AFM imaging revealed that these surfaces contain randomly mixed areas of both PNIPAAm and biocide. Biocidal testing showed that the addition of PNIPAAm does not decrease the surface's biocidal potency in the light, suggesting inactivation is caused by light-induced singlet oxygen generation.

1.2 Motivation

The field of molecular simulations could be said to have its genesis in the 1960s with the first development of intramolecular potentials by three independent groups. Norman Allinger at Wayne State University (Detroit, Michigan) developed code to optimize molecular geometries using classical, empirical potentials. Concurrently, George Némety and Harold Scheraga at Cornell University focused on simplified potentials and statistical mechanics to generate energy minimized molecular geometries of protein structures. In addition Shneior Lifson and Arieh Warshel (and later joined by Michael Levitt) at the Weizmann Institute of Science worked on the construction of inter- and intramolecular potentials for complex systems utilizing experimental data such as spectroscopic information.[1-6] In the early 1970s, Warshel visited Martin Karplus at Harvard where the two developed the first multiscale modeling approach, initially used to

calculate the π-electron spectra and the vibration spectra of several planar molecules.[1, 7] In 1975 Levitt and Warshel published the first coarse-grained protein model, which used convergent energy minimization and normal mode analysis on a coarse-grained bovine pancreatic trypsin inhibitor (BPTI) protein to find a series of intermediation conformations between an unfolded state and a near-native folded structure.[3, 8, 9] The first molecular dynamics simulation of a biological process, also focusing on BPTI (run for 9.2 ps in vacuum), came from the Karplus group two years later.[1, 10] The work done by these groups would form the foundation of molecular modeling and simulations as the field expanded in the following decades. For the "development of multiscale models for complex chemical systems," Martin Karplus, Michael Levitt, and Arieh Warshel were awarded the Nobel Prize in Chemistry in 2013.[1-3]

Since those early days of development, molecular modeling has continued to expand rapidly in both scope and complexity[2]. Varying techniques, ranging from highly detailed quantum mechanical calculations to large scale fluid dynamics, have been developed to address a wide array of topics.[2, 5, 11-26] The choice of technique is determined by weighing the required accuracy against the computational cost. Here accuracy is defined as how well a model or simulation mimics real-life behavior by matching known experimental values. Generally, more complex interactions yield more accurate results. An infinitely complex simulation would calculate the full quantum mechanical interactions between every elementary particle within a given system. But increasing complexity comes at the price of increasing computational cost. The computational cost of a model is determined mainly by a) the number of particles being simulated, b) the complexity of interactions between those particles, and c) the number of times the

interaction calculations will be performed. Depending on the computational resources available, the limit in increasing computational cost will be the overall calculation time.

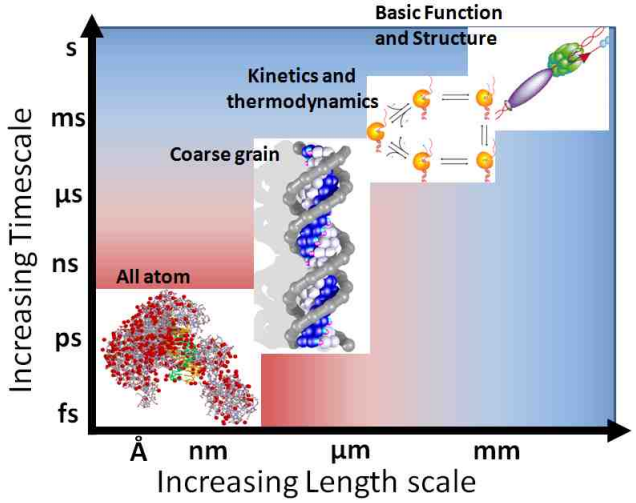

Figure 1: In biochemistry simulations, a division of standard techniques has developed that spans a large spectrum of target size and simulation time

On the more precise, computationally expensive side of the scale, there exist all-atom techniques. These techniques include methodologies like the structurally coupled quantum mechanical-molecular mechanics (QM/MM), which takes a region (e.i. an active site) where quantum mechanical calculations determine the positions and velocities of particles and combines it with a surrounding environment where such values evolve according to classical physics.[26, 27] The majority of all-atom simulations are performed using commercially available software packages such as CHARMM, AMBER, NAMD, or GROMACS.[28-31] In biological applications, enzymatic reactions and small protein folding runs are frequent targets of all-atom calculations. The need to compute many atom-atom interactions on every time step usually limits all-atom simulations to relatively small systems (biologically speaking) and nanosecond time scales.[32] Currently, the longest simulation time for an all-atom calculation is an approximately 1 millisecond calculation of the BPTI protein in water (equaling 17,758 particles). This calculation was

made at a rate of 9.8 μs/day by Anton, a massively parallel computer purpose built from the processor level for all-atom simulations[27, 33, 34]. Results from this specialized computer represent the near limit in size and timescale for all-atom simulations.

The size and time restrictions of all-atom simulations make it difficult to use otherwise powerful simulation methods to investigate, say, global mechanisms and turnover events for protein or nucleic acid molecular machines. In response, many coarse-grained (CG) approaches have been developed where individual atoms are replaced with a smaller number of pseudo-atoms or "beads."[12, 15, 21-23, 32, 35-71] The beads reduce the number of required calculations, allowing for larger systems to be simulated for longer times. Interactions among the beads are modeled to match (as closely as possible) the behavior of groups of atoms.[15, 32, 35, 45, 51, 63] This has led to the development of a variety of coarse grain techniques that cover many orders of magnitude both in size and time. Instead of standardized packages, most CG models utilize a set of standard techniques and adjust their resolution scale to the particular problem at hand. Larger units may be treated as elastic bodies[22, 38], and solvents or membranes may be treated as continua[36, 66], though decreased resolution entails the loss of molecular detail and (perhaps) of predictive ability.[2, 60, 63] But by choosing an appropriate resolution for each feature, very large biological systems can be modeled over long times.

2. MULTISCALE/COARSE-GRAINED SIMULATION

2.1 Introduction

Here we report the development of a CG simulation which has been given the name TM2. The program was developed in the context of a DNA/DNA polymerase model, but the program itself is designed to be much more general. The goal is to develop a software system that could simulate a full cycle of DNA and DNA polymerase, but remain versatile enough to be used in simulating completely different systems. The basic structures from which the system is built, "units", are quite complex compared to the atoms in standard all-atom simulations. Units can represent objects at various resolution levels from a single atom to an entire protein. Many units (each one possibly representing a different resolution) interact with each other to create a system. The potentials that determine the interaction between these CG elements are adjustable and not reliant on resolution-dependent, pre-determined force fields. TM2 can also incorporate continuum models, as is demonstrated below with an implicit solvent model. Movement within the program is Brownian dynamics in both the center of mass and orientation coordinates of the units. As a CG program, the focus is not on replicating precise kinetics at every time step, but instead on reproducing equilibrium (Boltzmann) statistics. Physical accuracy is balanced against computational cost with an emphasis on simulating (relatively) long periods of time (μs or longer). In addition, TM2 has been parallelized to allow for multiple-input parameter techniques, such as Replica Exchange Molecular Dynamics (REMD), to be run simultaneously across multiple central processing units (CPUs).

2.2 Units

TM2 constructs coarse grain models by placing a collection of "units" in a specific arrangement. A unit contains points that define its shape and interactions with other units. These points do not change during the simulation and do not interact with each other. Units can also change shape by means of a set of normal modes. As the basic building blocks of the program, these elements can represent any number of atoms required by the system. For example, when modeling DNA/DNA polymerase, a single DNA residue is a unit (representing tens of atoms). Within the same system, the DNA polymerase is also considered a single unit (representing thousands of atoms). These CG elements interact with each other and the environment via specific interaction points classified as "bead points" or "shell points." Bead points interface with all other beads via a set of point-to-point pairwise additive potentials. Shell points are used to represent space-filling bodies within the model and interface with other bead or shell points via a repulsive "shape" potential. Figure 2 shows three examples of a unit; a DNA residue composed of only bead points, a protein composed of only shell points, and a protein with both bead and shell points.

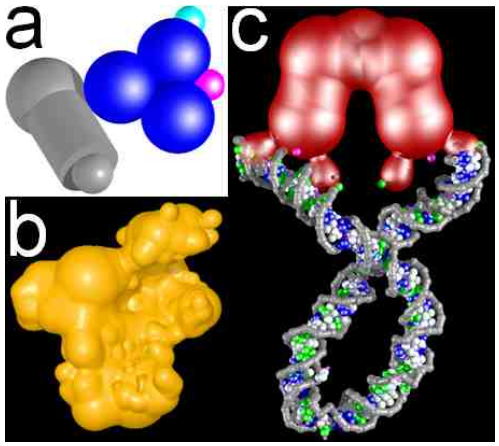

Figure 2: Examples of a unit within the TM2 program. (a) DNA residue unit composed of only bead points, (b) polymerase unit composed of only shell points. (c) Lac repressor DNA protein unit with shell points and bead points interacting with a short DNA strand.

2.2.1 Bead Points

Within the basic unit, beads are single points responsible for interactions with the rest of the simulation environment and primarily interact with bead points on other units. The potential associated with a particular bead determines its *type* and dictates how it will respond to other bead points. Currently, vacuum interactions among all beads are described by three pairwise additive potential functions.

$$V_{vac} = V_{bond} + V_{sc} + V_{Q4}$$

Equation 1

where V_{bond} is a harmonic bonding potential, V_{SC} is a screened Coulomb charge potential and V_{Q4} is an adjustable potential with both repulsive and attractive parts. In principle, more potentials could be developed (the Q4 potential already covers several cases); however, this set has proven sufficient for the DNA/DNA polymerase system.

At every step of the program, the forces between bead pairs are tabulated. Bead-to-bead pair forces are only calculated for pairs that fall within the shortest cutoff distance (where the cutoff distance is determined by the type of potential on each bead). Currently, bead potentials do not change during a simulation, though future development of TM2 will involve the inclusion of potentials that can be created and destroyed.

2.2.1.1 COVALENT BONDS

Covalent bonds between units are approximated by a harmonic pair potential shared between two bead points. The bond potential is

$$V_{bond} = \frac{1}{2} k r^2$$

Equation 2

where k is the bond force constant and r is the distance between the beads. Since TM2 currently does not simulate chemical reactions, this first-level approximation for chemical bonds is sufficient for simulating DNA.

2.2.1.2 CHARGED BEADS

Charged beads carry a screened coulomb potential

$$V_{sc} = \begin{cases} \frac{q^2}{\varepsilon}\frac{e^{-r/d}}{r}, & r < r_{cut} \\ 0, & r \geq r_{cut} \end{cases}$$

Equation 3

where q, ε, and d are the (effective) bead charge, the dielectric constant, and the Debye length, respectively. The distance between the beads is r while r_{cut} is the cutoff distance. The Debye-Hückel approximation is used to represent physiologically relevant salt concentrations.[21] Currently the dielectric constant is equal to its value for water at room temperature (80) and the cutoff distance is currently set to 2.56 nm.

2.2.1.3 Q4 POTENTIAL

Early trial simulations showed that the common generic interaction potentials (e.g., 6-12 Lennard-Jones and similar potentials) were inadequate for our purposes. This is mainly because their hard cores tended to make long time steps unstable and because their range of possible functional shapes was too limited (e.g., we want beads with large core radii but surrounded by a thin attractive skin). The third potential, V_{Q4}, was therefore chosen to be soft and flexible enough to cover a wide range of sizes and interaction length scales (see Figure 3). It is a piecewise quadratic function with a harmonic minimum at R_0 and a tail that begins at R_1 and that goes smoothly to zero at R_2:

$$V_{Q4} = \begin{cases} \frac{1}{2}k_0(r - R_0)^2 - V_0 & 0 < r < R_1 \\ -\frac{1}{2}k_1(r - R_2)^2 & R_1 < r < R_2 \\ 0 & r > R_2 \end{cases}$$

Equation 4

where V_0 is the well depth, and k_0 and k_1 are the stiffness of the minimum and the stiffness of the tail regions, respectively. The dividing point, R_1, and cutoff distance, R_2, are defined so that the function and its first derivative are continuous at R_1 for given values of V_0, k_0, k_1:

$$R_2 = R_0 + \sqrt{2V_o\left(\frac{1}{k_0} + \frac{1}{k_1}\right)} \qquad R_1 = \frac{k_0R_0 + k_1R_2}{k_0 + k_1}$$

Equations 5,6

The four parameters of V_{Q4} , R_0, V_0, k_1, k_0 allow the position of the minimum, the depth and width of the minimum, and the length of the tail to be adjusted independently and directly.

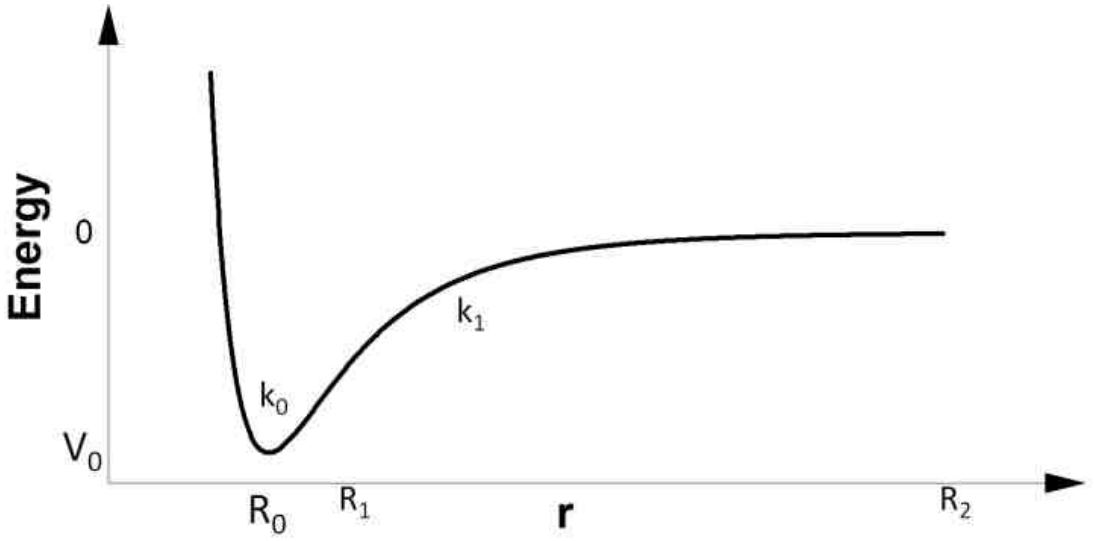

Figure 3: Graph of the Q4 potential. V_0 is the energy well depth (at distance R_0), k_0 and k_1 are the curvatures of the minimum and the tail regions that switch at distance R_1 , and R_2 is the potential cutoff distance.

2.2.1.4 SOLVENT MODEL

The bead-to-bead potentials described above represent vacuum interactions. Early results from the DNA model (see Chapter 3) showed that when the potentials were adjusted to match estimates for stacking energy and hydrogen-bonding energies in vacuum, the double-stranded DNA had good structure and local order, but very high mechanical (bending, torsion) stiffness and very high melting temperature. Reducing the strength of attractions (to crudely account for solvent effects) produced helices with reasonable long-range stiffness but high local disorder. To get both good local structure and reasonable mechanical properties (and also reasonable vacuum energies for stacking and H-bonding), we added a simple implicit solvent model. The model is a version of the Effective Energy Function (EEF1) approach[72], which assigns energies (and forces) depending on the degree to which a bead is exposed to solvent.

The EEF1 implicit solvent model[72] is useful for our purposes because it generates a pair-wise additive force that has a low computational cost and is easily generalized to beads of several sizes and properties. EEF1 assigns a normalized solvent exclusion field,

$$\left(\frac{2}{4\pi\sqrt{\pi}\lambda_i}\right)\frac{e^{-\left(\frac{r-R_i}{\lambda_i}\right)^2}}{r^2}$$

Equation 7

to each bead i, where R_i is the effective radius of bead i, and λ_i is the effective size of a solvent molecule. Let $\rho_j(r)$ be the density for bead j at position r relative to bead i, normalized to unity over all space,

$$\int d\Omega \int_0^\infty \rho_j(r)\, r^2 dr = 1$$

Equation 8

and let V_j be the volume of bead j . Then

$$v(r) = \frac{1}{4\pi} \int \left\{ \sum_{j \neq i} V_j \rho_j(r) \right\} d\Omega$$

Equation 9

is the fraction of volume in the spherical layer at distance r from bead i that is occupied by other beads, and the integral

$$\int_{R_i}^\infty \left(\frac{2}{\sqrt{\pi}\lambda_i} \right) e^{-\left(\frac{r-R_i}{\lambda_i}\right)^2} v(r) dr = \int d\Omega \int_{R_i}^\infty \left(\frac{2}{4\pi\sqrt{\pi}\lambda_i} \right) \frac{e^{-\left(\frac{r-R_i}{\lambda_i}\right)^2}}{r^2} \left\{ \sum_{j \neq i} V_j \rho_j(r) \right\} r^2 dr$$

Equation 10

can be interpreted as the fraction of volume in the first solvation shell of bead i that is occupied by neighboring beads. Therefore, define the burial fraction for bead i as

$$f_i = f_{0i} + \sum_{j \neq i} f_{ij}$$

Equation 11

where

$$f_{ij} = V_j \left\{ \int d\Omega \int_{R_i}^\infty \left(\frac{2}{4\pi\sqrt{\pi}\lambda_i} \right) \frac{e^{-\left(\frac{r-R_i}{\lambda_i}\right)^2}}{r^2} \rho_j(r) r^2 dr \right\} \cong V_j \left(\frac{2}{4\pi\sqrt{\pi}\lambda_i} \right) \frac{e^{-\left(\frac{r_{ij}-R_i}{\lambda_i}\right)^2}}{r_{ij}^2}$$

Equation 12

is the fraction of the volume of the first solvation shell of bead i that is occupied by bead j. Here f_{0i} is the (fixed) burial fraction due to beads in the same unit as bead i, r_{ij} is the distance from bead i to bead j, and the sum is over beads in other units only. The last expression on the right for f_{ij} makes the approximation that the densities $\rho_j(r)$ are sharply localized. This is the approximation used in EEF1[72] and for all results reported here. Note that the functional form of f_i allows it to be greater than 1 in principle, though it will be less than 1 for reasonable values of the V_j and reasonable packing arrangements of the beads. In principle, only the addition of the burial fraction variables, f_i and f_{ij}, differentiates this version of EEF1 from Lazaridis et al.[72]

Solvent forces on bead i are gradients of $\Delta G_i^{solv} = \Delta G_i^{free}(1 - f_i)$ plus reaction forces from other beads, and EEF1 generates a pair-additive force,

$$F_i^{solv} = -\left[\Delta G_i^{free} V_j \left(\frac{2}{4\pi\sqrt{\pi}\lambda_i}\right) + \Delta G_j^{free} V_i \left(\frac{2}{4\pi\sqrt{\pi}\lambda_j}\right)\right] \nabla_i \left\{\frac{e^{-\left(\frac{r_{ij}-R_i}{\lambda_i}\right)^2}}{r_{ij}^2}\right\}$$

Equation 13

that depends only on the burial of each bead by its partner, independent of the positions of other beads. The EEF1 solvation model requires five parameters per bead: ΔG_i^{free}, R_i, V_i, f_{0i}, and λ_i. Following Lazaridis et al., we set the value of λ_i, the effective width of the first solvation shell, to 0.35 nm for all beads. The effective radius, R_i, was set to the Q4 radius, R0, for each bead. The volumes V_i were calculated from the bead radius using $V_i = \left(8/\sqrt{2}\right){R_i}^3$, which is the volume occupied by a sphere in a hexagonally close packed lattice. This choice means that the burial fraction will be unity for beads surrounded by other beads of the same type in an HCP lattice, and effectively defines the

reference state for the solvation free energy. The fixed burial fractions due to solvent screening by other beads in the same unit, f_{0i}, merely add a constant to the solvent energy and do not affect solvent forces. This leaves ΔG_i^{free} as the only adjustable solvation parameter. When the "hydrophobicity" (the terms in square brackets in Equation 13 above) is positive the force is attractive; when the hydrophobicity is negative the force is repulsive. The fact that EEF1 generates an additive force is an advantage for simplicity and speed, but a disadvantage for accuracy and realism. True solvent forces are not pair-additive.

2.2.2 Shell Points

While the bead points exist to determine point-to-point interactions between units, shell points determine the repulsive body shape of a unit. It is worth noting that the bead points can carry repulsive potentials, and therefore in some cases beads can completely describe a unit, and shell points are not required. This can be seen in the DNA residues, which are composed entirely of beads (see Chapter 3). The shell potential, defined by the shell points, can describe a solid, elastic body, usually at low resolution. If a protein has a local region where high resolution is needed (e.g. the active site) in a otherwise large structure, then bead points are only needed for that region while the rest of the protein can be represented by a few shell points. The use of shell points to create a coarse-grained protein model is covered in more detail in Chapter 4.2

Shell points interact via a repulsive, body potential V_{body} that functions as a volume-exclusion force field. Each shell point is the source of a local density field. The

sum of these local densities creates a density field for the full body. Isosurfaces of this body density field serve as isosurfaces for the potential V_{body}.

$$V_{body} = V_0(\rho/\rho_0)^n$$

Equation 14

The density, ρ, is the sum of local functions mentioned above and ρ0 is the threshold isosurface. The density is defined as

$$\rho = \begin{cases} \sum_i [1-(r_i/R_i)^2]^2, & r_i \le R_i \\ 0, & r_i > R_i \end{cases}$$

Equation 15

where r_i is the distance to bead or shell point, and R_i is the cutoff distance. The R_i values set the scales of the local densities; points with large R_i are used for regions where the body shape needs low resolution only while points with small R_i are used in regions where higher surface detail is required. When ρ equals ρ0, the potential rises rapidly, and therefore this isosurface represents the repulsive surface, or boundary surface, of the protein. The width of this potential, which controls the surface "hardness," is set by the exponent n.

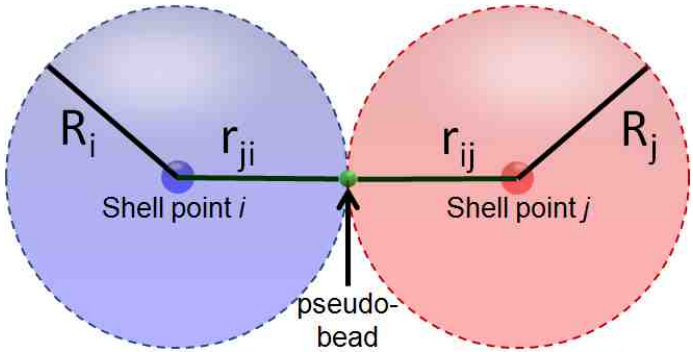

Figure 4: Shell point to shell point interaction. Shell point i with an isosurface at distance R_i crosses with shell point j with a repulsive surface at distance R_j. A pseudo-bead is created to determine the forces felt by point i due to shell j (r_{ij}) and by point j due to shell i (r_{ji}).

In the shell potential, forces are determined by the distance (r) between the initial shell point and an incoming bead. In the case of two interacting shell points, the situation is more complicated (see Figure 4). Consider two shell points (i and j) that are close enough for their respective boundary surfaces to be interpenetrating each other (i.e. $r < (R_i + R_j)$). To find the repulsion felt by point i due to shell j, shell point i is temporarily replaced by a pseudo-bead. This pseudo-bead is created at the location where shell i's boundary surface is the closest to point j. Forces felt by this pseudo-bead from shell j are then calculated as a standard bead-to-shell point interaction and then applied to shell point i. The pseudo-bead technique is then repeated in the reverse case to find the repulsion felt by point j due to shell i.

2.2.3 Eigenmodes

Molecular structures are not static, and often their functionality depends on their ability to change shape.[11] In TM2, single units are allowed to deform according to a set of their normal modes of oscillation. The modes of oscillation for a unit can be determined, for example, by the Elastic Network Model[22, 73, 74] or from short-time atomistic simulations. Once the main modes of oscillation are determined, they are included as an inherent property of the unit. At each time step, the bead and shell points are moved according to the (Brownian) motion along each normal mode.

2.3 Movement Dynamics

At each time step units move by Brownian rigid body translations and rotations[75]:

$$\Delta x = \frac{\Delta t}{\gamma}(F_{Total} + R)$$

Equation 16

where Δx is displacement of a spatial or angular coordinate, γ is a friction coefficient, Δt is the time step, F_{Total} is the sum of all external forces acting on beads or shell points of the units (or torques about the centroid), and R is a Langevin (time-uncorrelated Gaussian) random force (or torque) from the implicit thermal bath, with variance

$$\langle R^2 \rangle = 2\gamma k_B T / \Delta t$$

Equation 17

where T is temperature and k_B is Boltzmann's constant. Mass and rotational inertia are not included because friction is dominant at this size scale and inertial relaxation times are very short (of order 0.1 ps, one time step or less). Positions (and orientations) are computed by multiplying an inverse friction tensor by the relevant summed forces and torques.

In the current program, the translational and rotational friction matrices are independent of spatial coordinates and isotropic. Not included is hydrodynamic coupling,[75, 76] which is the flow field forces felt by neighboring moving particles in solution. The evaluation of hydrodynamic interactions is usually one of the most computationally expensive elements of a simulation,[77] and therefore many coarse grain programs do not include hydrodynamic calculations. All units are assumed to be frictionally independent, which eliminates the need for complex calculations, e.g. Oseen-tensors, greatly reducing the overall calculation time.[2, 21, 49] Similarly to other common coarse-grain models, TM2 will not necessarily reproduce the correct kinetics or fluctuation dynamics (though these seem to be qualitatively reasonable). However, the equilibrium probability distribution of a Brownian system is the Boltzmann distribution for the potential energy function[75, 78], so the simulation will produce the correct equilibrium statistical and thermodynamic properties (for the given force fields).

2.4 Parallel Processing

A version of TM2 has been setup to handle multiple CPUs and is currently optimized for REMD calculations. The Message Passage Interface (MPI) is a C/C++ Library that allows for multiple instances of the basic TM2 program to be run simultaneously across several CPUs. The MPI code works as an overlay program that calls instances (known as "threads") of TM2 with specialized inputs. This allows TM2 to run on all cores of, for example, a single desktop computer. It also allows many TM2 simulations to be conducted simultaneously on supercomputer clusters, making longer runs and larger systems more feasible.

Multiple, simultaneous thread calculation is required in order to utilize Replica Exchange Molecular Dynamics (REMD), an algorithm developed by Sugita and Okamoto[79] that improves the efficiency of certain simulations by allowing larger conformational sampling than is possible in single runs.[79-83] Long-lived metastable states that represent a local (but not global) energy minimum present a difficulty for simulations, as the model can often become trapped in these states for long periods of time. As computer resources are limited, the amount of conformational sampling of a particular state is also limited. A model that becomes trapped in a metastable state can easily spend the rest of a run in this state and never reach a true energy minimized conformation. In REMD, several simulation threads are run in parallel and each thread has a unique temperature. At regular intervals, comparisons are performed that yield a probability for threads to switch temperatures. This allows a single run to sample different temperatures during a long simulation. The probability (P) to switch between two replicas (1and 2) is

$$P = \begin{cases} 1, & E_1 \geq E_2 \\ e^{-\left(\frac{1}{k_B T_1} - \frac{1}{k_B T_2}\right)(E_2 - E_1)}, & E_1 < E_2 \end{cases}$$

Equation 18

where T is the simulation temperature, k_B is the Boltzmann constant, and E is the total system energy for each replica. A particular thread will always seek the lowest energy, but the Boltzmann factor allows for possible shifts to higher energies, providing the means to escape possible local minimum energy wells. Figure 5 shows a simplified diagram of replica switching and the ability of the technique to better sample conformations.[80]

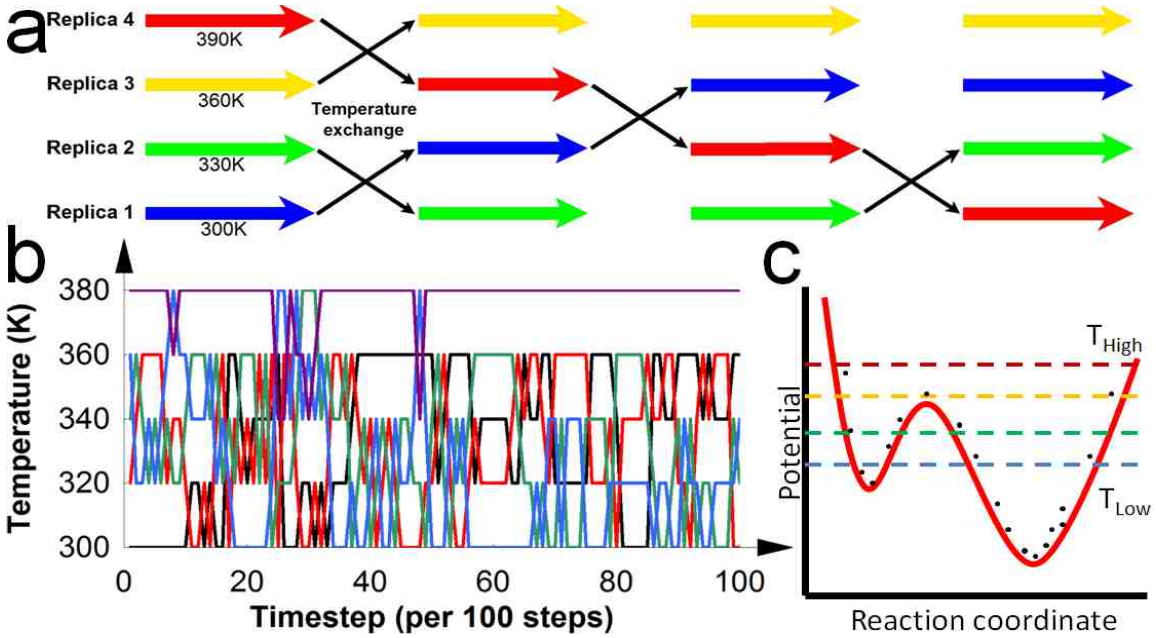

Figure 5: REMD (a) A simplified REMD temperature switching for a 4 thread calculation. Some threads, such as 1 (blue) and 4 (red), can move across a large number of temperatures while others, such as 2 (green) and 3 (yellow), can remain relatively stable. (b) A more realistic example of temperature switching from a 5 thread run of TM2 that shows a better relationship between the length of the run (10,000 steps in this case) and the number of possible temperature switches (100). (c) A simple energy landscape with a local energy minimum separated by an energy barrier from the true global minimum. The dotted lines correspond to the temperature threads from (a) and show how higher temperatures allow sampling along the reaction coordinate (black dots) the ability to overcome the energy barrier and reach the local minimum.

The TM2 program is still in the process of refining its implementation of REMD. Exact parameters (such as the ideal temperature distribution and the number of runs) are being optimized, but initial runs have been tested (see Figure 6). Implementation has also begun on the Weighted Histogram Analysis Method (WHAM).[84] This method is commonly used in conjunction with REMD as it reweights the outputs to provide parameters such as the energy probability distribution. For the DNA model, this can be used to determine the melting curve of the model and directly compare it to experimental results.

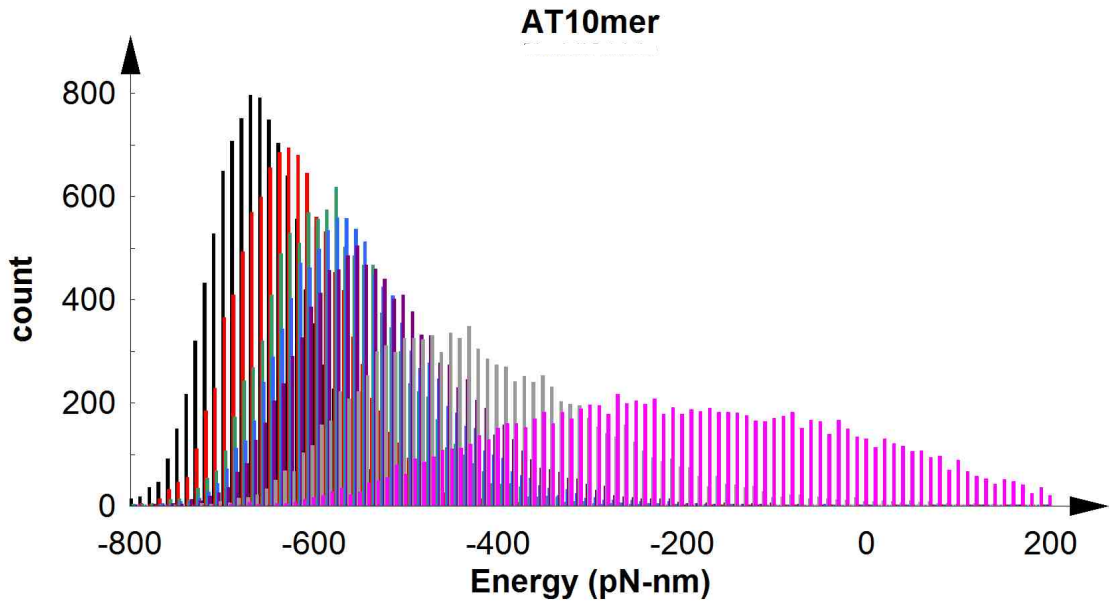

Figure 6: Histogram showing the energy distributions for each thread of a 10 μs, 7 thread REMD melting simulation of an $A_{10}T_{10}$ DNA model (see Chapter 3). Threads correspond to temperatures 380 K (black), 405 K (red), 430 K (green), 440 K (blue), 450 K (purple), 475 K (gray), and 500 K (pink). Global conformational energy values for the DNA strand from each thread were collected for the last two thirds of the run and analyzed using WHAM. While energy overlap is required for the REMD approach, our preliminary results show more overlap than necessary, especially at lower temperatures. This indicates that our temperature spacing should be broader at those temperatures.

2.5 Conclusion

The TM2 course grain simulation program has been constructed with the purpose of simulating molecular machines. The program builds system models from units, a variable-resolution representation of the system's atomic structures. These units interact via general, adjustable potentials with parameters determined by the specific model being reproduced. Forces generated by these potentials affect how the units move under Brownian dynamics. Parallelization allows for multiple, simultaneous instances of TM2 across several CPUs, greatly increasing the speed of some calculations. The development of TM2 was done in the context of coarse graining the DNA/DNA polymerase system. While the program itself is designed to be much more general, specific potential parameters were set to fit this system. In modeling DNA and DNA polymerase, the former structure provides a much greater challenge to simulate as it contains many more degrees of freedom. The next chapter details the creation and parameterization of a coarse-grained DNA model.

3. THE DNA MODEL

3.1 Introduction

The DNA coarse-grained (CG) model is intended to function realistically with protein models, especially DNA polymerases and other DNA-recognizing molecular machines. We require the model to be capable of "natural" double helix formation, so that DNA complementation and hybridization arise from the structure and interactions of the residues alone. We also require that chains of such residues are stabilized by base stacking and hydrogen bonding, as in real DNA. These features, in turn, require higher resolution and more beads per residue than in most previous CG DNA models. The modified EEF solvent model described above in Chapter 2.2.1.4 was found to be necessary for qualitatively correct base-base interaction energies, helix elasticity, and mismatch melting properties.

The results below illustrate the behavior of this model in a variety of special cases: double-stranded straight DNA (sometimes with mismatched base pairs), single-stranded DNA, covalently closed double-stranded loops, and a DNA hairpin. In all cases, chains with complementary sequences form stable base paired double helices at or near room temperature, and the helical parameters (twist, rise, buckle, propeller, etc) are close to canonical B-form DNA. Most mismatched sequences are unstable at room temperature. On longer length scales, the elastic properties of double helices (bending and twisting persistence lengths) are close to experimental values. Single-stranded DNA with no self-complementary regions are highly disordered, with backbone bending angles fluctuating rapidly over a wide range. Locally, the bases transiently stack and unstack,

and show a weak statistical tendency to form helical conformations. Closed loops of double-stranded DNA form statistically flat, untwisted circles when the net linking number is zero, or twist into supercoils when the net linking number is non-zero. A single-stranded DNA hairpin melts at a high temperature and becomes a disordered chain. By careful cooling, the correctly base paired hairpin can be reformed. The complementary double helix thus appears to be the true thermodynamic ground state for the model.

3.2 DNA Setup

3.2.1 Residue Geometry

Nucleotides, or residues, are the basic building blocks of DNA. In TM2, DNA is represented by many units where each residue is a single unit. Each unit is composed of several bead points. Coordinates of the beads in each unit are listed in Table 1. Figure 7 shows a generic residue with all beads labeled and in the local frame as used in Table 1. The atoms of the residue that form the backbone are represented by two beads (denoted P and T in Figure 7) located on the z axis. These beads act as linking sites between residues where the T bead on the n^{th} residue is covalently bonded to the P bead of residue n+1 on the same strand. The P bead carries two additional interactions: a screened coulomb potential to account for charge-charge repulsions between phosphates, and a Q4 potential (see Chapter 2.2.1.3) to give the backbone some bulk and dispersion-like interactions with other beads. The atoms of the residue that form the bases are represented by either five beads (for adenine or thymine) or six beads (for guanine or

cytosine). The flat plane of a base is represented by three "base body" beads (denoted by B in Figure 7 and Figure 8). The beads carry Q4 potentials with a repulsive core that gives the base its shape and sets the interbase stacking distance. The Q4 potential's attractive minimum creates the (vacuum) stacking interaction between bases. The base beads positions were generated by: i) placing all beads so as to create the base structure in the local xy plane, ii) rotating the base about the x axis, and iii) rotating the base about its normal vector. The first rotation angle (about the x axis) is given by

$$sin\theta = rise/\sqrt{(rise)^2 + 4(rad)^2 * sin^2(twist/2)}$$

Equation 19

which orients the base plane perpendicular to the axis for a helix of radius *rad*, with translation of *rise* per reside along the axis, and rotation of *twist* per residue about the axis. For *rad* = 1 nm, *rise* = 0.34 nm, and *twist* = 36° (the values used in the model, equivalent to ideal B-form DNA), θ = 61.2°. The second rotation angle (about the base plane normal), φ, creates an angle between the backbone chains of a double-stranded DNA in the plane perpendicular to the helix axis. The major groove angle is π - 2φ; the minor groove angle is π + 2φ; and φ = -20° in the model. Hydrogen bonding interactions are represented by either two (A and T) or three (G and C) beads, labeled as H-bond donors and acceptors (D or A in Figure 7). These beads also have a Q4 potential, but with a much smaller repulsive core than the base-body beads. Hydrogen bonding beads can only bond to the opposite partner, i.e., acceptors are attracted only to donors and vice versa. The body and H-bonding beads are set at positions close to the corresponding groups in real DNA bases. To account for their larger size in real DNA, the body and H-bonding beads in the purine bases A and G are set further from the backbone than those of the pyrimidine bases T and C (see Figure 8). For example, the line where an A base

meets its complementary T base on the opposite strand is slightly off-center from the helix axis. The hydrogen bonding beads are arranged to create a lock-and-key relationship between complementary base pairs. This arrangement makes non-Watson Crick base pairing energetically less favorable.

Table 1: Coordinates of all beads in each residue in the local residue coordinate frame

	Base Type			
Bead	A	T	G	C
T	(0.000, 0.000, 0.300)*	(0.000, 0.000, 0.300)	(0.000, 0.000, 0.300)	(0.000, 0.000, 0.300)
P	(0.000, 0.000, -0.406)	(0.000, 0.000, -0.406)	(0.000, 0.000, -0.406)	(0.000, 0.000, -0.406)
B_0	(0.510, 0.083, -0.152)	(0.416, 0.100, -0.182)	(0.510, 0.083, -0.152)	(0.416, 0.100, -0.182)
B_1	(0.903, 0.117, -0.213)	(0.809, 0.133, -0.243)	(0.903, 0.117, -0.213)	(0.809, 0.133, -0.243)
B2	(0.767, -0.064, 0.117)	(0.673, -0.048, 0.087)	(0.767, -0.064, 0.117)	(0.673, -0.048, 0.087)
A_0 ‡	(0.938, 0.008, -0.015)	-	-	(0.844, -0.025, -0.045)
A_1	-	(0.985, 0.210, -0.383)	(1.079, 0.194, -0.353)	(0.768, -0.147, 0.266)
D_0 ‡	-	(0.938, 0.008, -0.015)	(1.032, -0.008, 0.015)	-
D_1	(1.173, 0.177, -0.323)	-	(0.862, -0.163, 0.296)	(1.079, 0.194, -0.353)

*All (x,y,z) coordinates are given in nm

‡ The subscript 0 indicates the central bead only

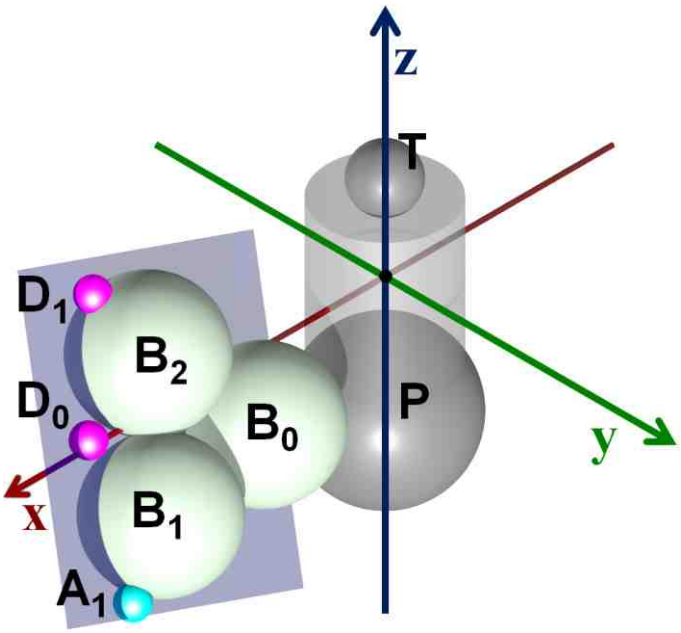

Figure 7: Structure of a residue in its local coordinate frame. Beads labeled P and T correspond to the sugar-phosphate backbone; beads labeled B0 through B2 represent the body of the base; A and D beads are acceptor/donor hydrogen bonding sites. The cylinder connecting beads P and T is for appearances only. The gray square represents the plane of the base.

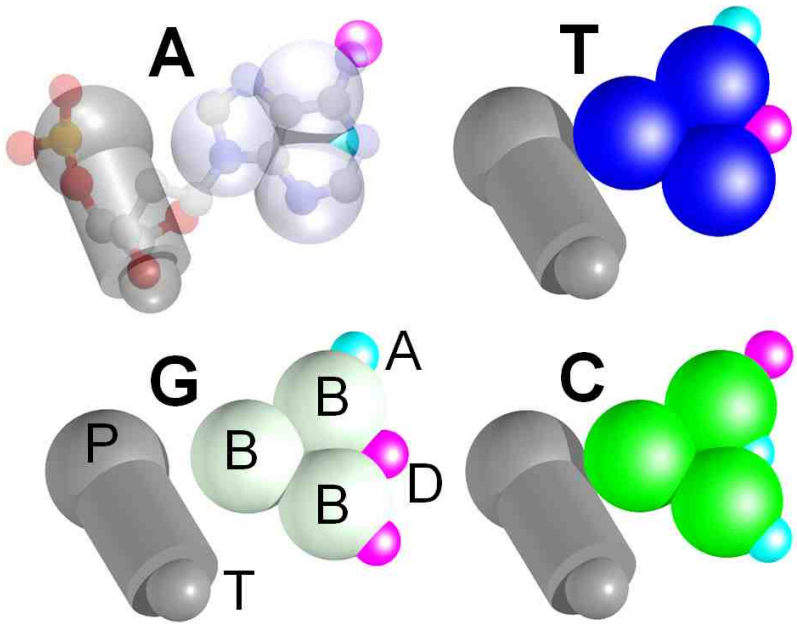

Figure 8: Coarse-grained representation of the DNA residues. The course grained model for adenine is superimposed on a ball and stick model from B-form DNA. Purine bases A and G are set at a larger distance from the backbone than the pyrimidine bases T and C. Each base also has a unique placement of hydrogen bonding acceptor and donor beads, designed to create a lock-and-key relationship with the complementary base

3.2.2 DNA Structure

The double-stranded model DNA is built from two complementary strands of rigid residue units (Figure 9). The base beads lie in a plane that is attached to the backbone at a fixed angle corresponding to the base-plane-to-backbone angle of a roughly B-form right-handed helix. The base body atoms are arranged so bases on the same strand prefer to stack on each other near a 36° twist angle about the helix axis. Finally, the bases are rotated within their planes so that when they are ideally stacked and base paired in a double-stranded helix they create a major and minor groove. (The axis-to-backbone angle is about 220° for the major groove and 140° for the minor groove.) As is apparent from above, much of the preferred structure of the double-stranded coarse-grained DNA helix is built into the geometry of the residues.

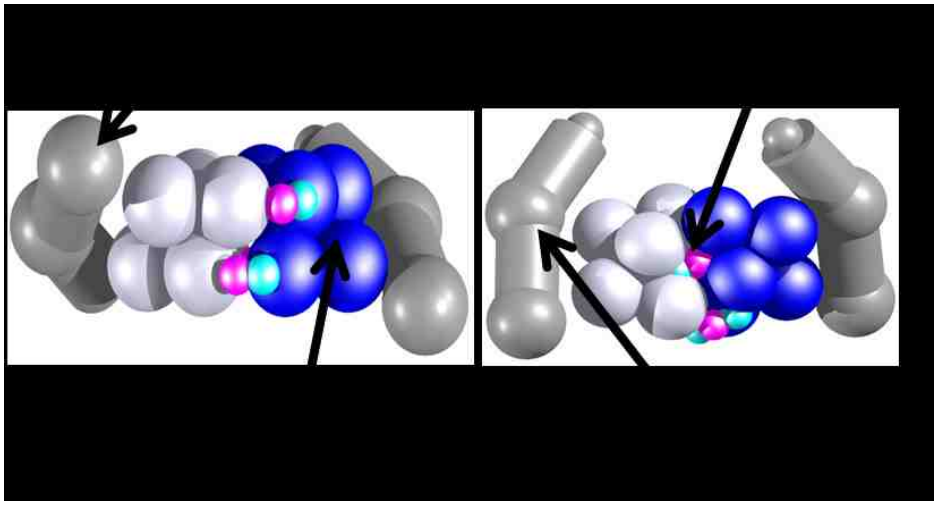

Figure 9: Coarse-grained representation of the stacked DNA residues. A four residue stack that demonstrates the four main potentials; screened coulomb, bonding, stacking, and hydrogen bonding. The same-strand 36˚ twist angle about the helix axis can be seen.

Figure 10 shows several components of the total energy during relaxation at zero temperature. For a DNA of this size, zero-temperature mechanical equilibrium is reached in about 250,000 time steps (25 ns). By construction, the main stabilizing forces are base stacking (green, dotted line) and hydrogen bonding (red, long dashed line). The principal destabilizing energy comes from the solvent model (not shown separately here), which favors solvated residues. (The ΔG_i^{free} values are negative for all base beads, which means that solvation free energy decreases with increasing exposure to solvent.) Smaller destabilizing contributions result from repulsion between phosphates (blue, dash-dot line) and backbone stretching (purple, short dashed line). Zero-temperature relaxation is mainly driven by small adjustments of structure that optimize hydrogen bonding, causing the overall structure to elongate and unwind slightly.

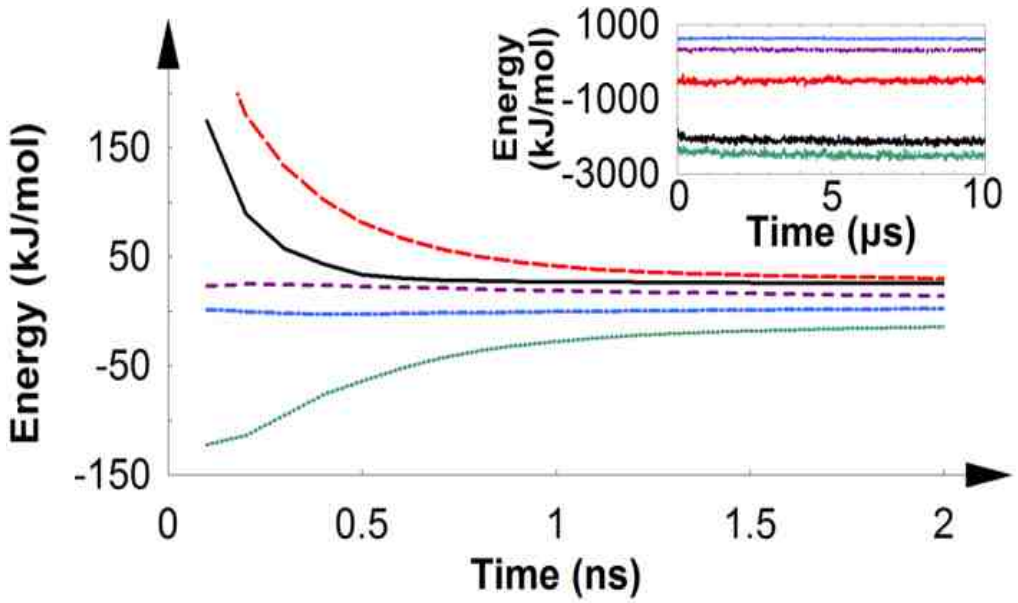

Figure 10: Energy components for $A_{50}T_{50}$ DNA during the first 20,000 steps (2 ns) of a simulation at 0 K. The curves represent the backbone bond stretching energy (purple, short dashed line), the screened Coulombic interaction of the phosphates (blue, dash-dotted line), the sum of the stacking vacuum and solvation energies (green, dotted line), the sum of the hydrogen-bond vacuum and solvation energies (red, long dashed line), and the sum of all interaction energies (black, solid line). For easier viewing, the curves have been shifted so they approach zero energy at equilibrium. The inset shows energy components for the same molecule for a 10-μs simulation at 300 K. The colors are the same as in the main figure, but the curves have not been shifted in energy.

At finite temperature (300K) the structure fluctuates both locally and globally, but remains stable at long times with no sign of metastability in either structure or energy. Figure 10 (insert) shows the main energy components over a 10 μs run. The average value of the H-bonding energy is about -500 kJ/mol, which corresponds roughly to -5 kJ/mol per H-bond, in reasonable agreement with published values for the difference in free energy between a stacked, H-bonded base and a solvated base[85]. Similarly the average stacking energy is about -2500 kJ/mol, corresponding to about -50 kJ/mol per stack. We estimate about -20 kJ/mol in backbone configurational entropic free energy is gained when a base melts, so the free energy difference between a stacked and melted base would be about -30 kJ/mol, also in reasonable agreement with results.[86]

3.2.3 Helix Coordinate System and DNA Geometries

Average DNA geometries at 300K for six representative complementary nucleotide sequences— $A_{20}T_{20}$, $(AT)_{10}(AT)_{10}$, $G_{20}C_{20}$, $(GC)_{10}(GC)_{10}$, $(CT)_{10}(GA)_{10}$, $(CA)_{10}(GT)_{10}$— are shown in Figure 11b,c and Table 4 (images of four of these sequences are shown in Figure 11a). The helix parameters are defined in close analogy to the Olson parameters[87]. To compare the structure of the model to standard DNA structures we used a version of the helix parameters of Babcock et al[88]. These parameters include three displacement lengths (shear, stretch, stagger) and three orientation angles (buckle, propeller, opening) between the two bases within a single base pair, and three displacements (shift, slide, rise) and three orientations (tilt, roll, twist) between nearest-neighbor base pairs along the helix. The helix parameters (including the helix tangent and perpendicular vectors that are needed to find persistence lengths), are defined using the coordinate frames shown in Figure 12, which are close equivalents (for the model DNA) to the frames defined in Babcock et al. (for real DNA).

Each individual base has a local frame that moves with that base. The local origin for this frame is defined so it would be midway between bases in an ideal base pair, that is, midway between the centers of the triangles of base body beads for a base that is part of an ideal B-form base pair. The x axis is along the line that joins the two front-edge base body beads, and points toward the major groove; the y axis bisects the triangle of base beads and points toward the backbone; the z axis is perpendicular to the base plane and points along the 5' to 3' direction (Figure 12a).

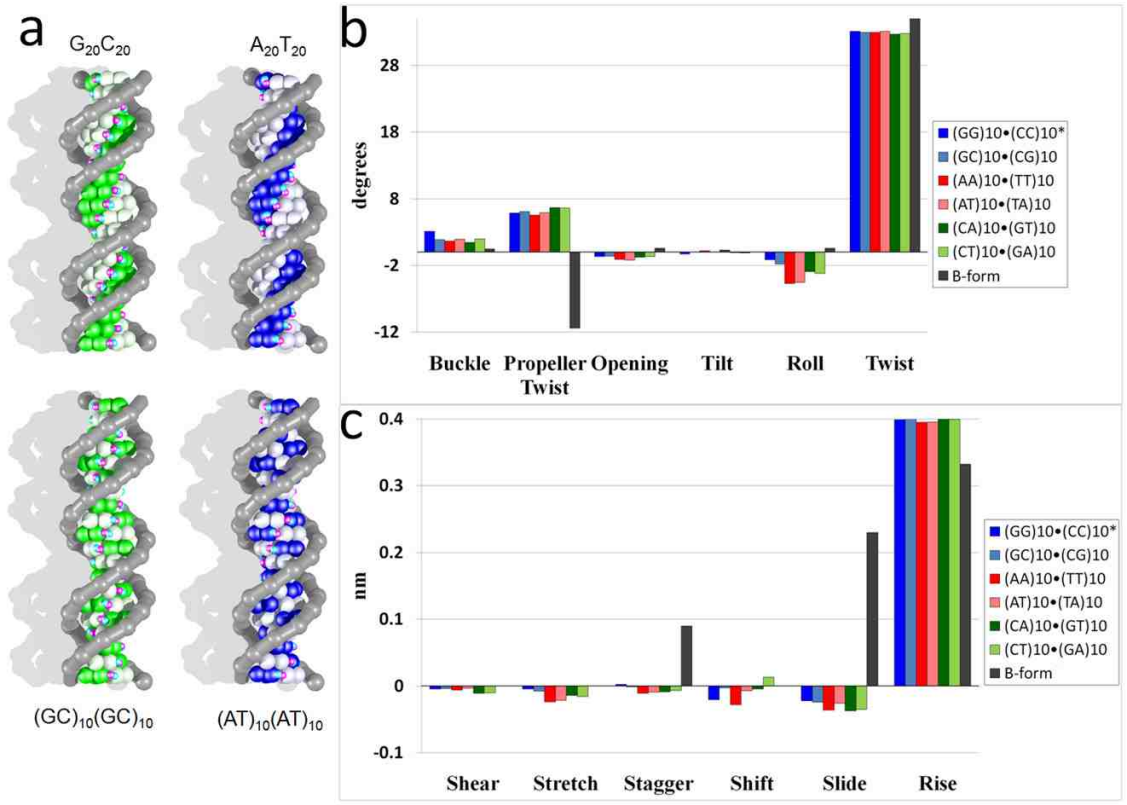

Figure 11: DNA sequences and geometries. (a) Four 20-bp DNA sequences. (b,c) DNA helix parameters for six model 20mer DNA sequences, compared to standard B-form geometries

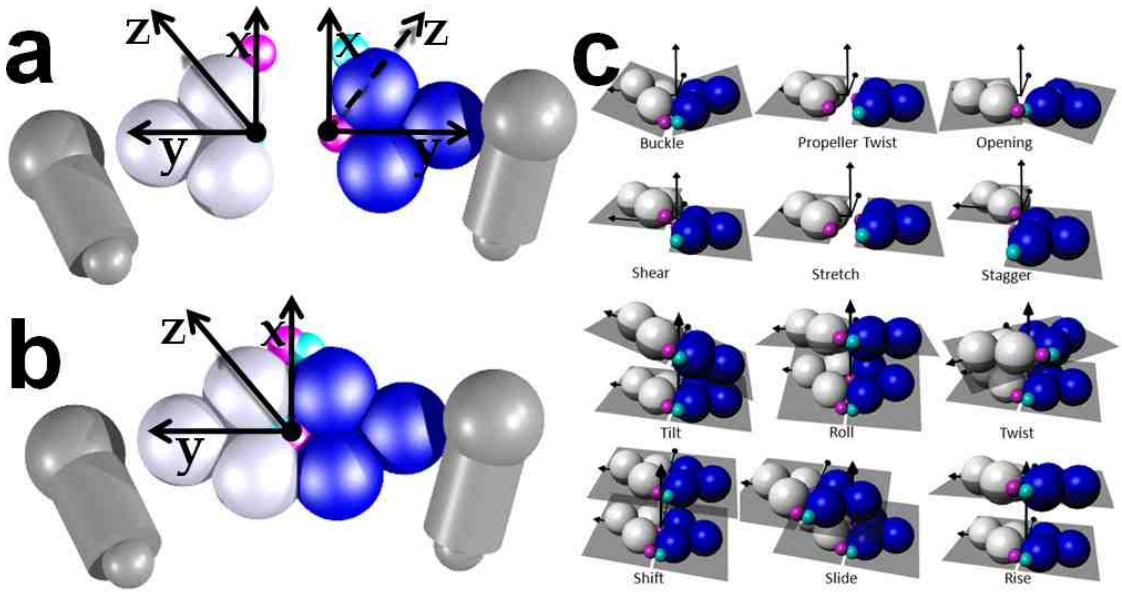

Figure 12: DNA geometry definitions. (a) Coordinate frame for the individual bases. Positive z is in the 5' to 3' direction (b) Basepair coordinate frame. (c) Olsen parameters[87, 88] for model DNA base pair geometries.

Following Babcock et al., the x axis and origin of the base pair frame (Figure 12b) are defined such that a rotation about the base pair x axis (usually by nearly 180 degrees), and a translation along the same axis, takes the base frame on the primary strand into coincidence with the base frame on the template strand. The base pair z axis is perpendicular to the x axis, and is at an angle half way between the z axes of the two base frames. The base pair y axis is z cross x. This definition puts the base pair origin approximately midway between the two bases, with the x axis roughly in the base pair plane and pointing toward the major groove. The z axis is roughly parallel to the helix axis along the 5' to 3' direction for the primary strand, and the y axis is in the base pair plane and pointing toward the backbone of the primary strand.

Table 2: DNA geometries for six simulated sequences

Geometries (deg)	$G_{20}C_{20}$	$(GC)_{10}$ *	$A_{20}T_{20}$	$(AT)_{10}$	$(CA)_{10}$	$(CT)_{10}$	B-form‡
Buckle	3.566	2.194	0.977	1.809	1.603	1.622	0.5 ± 6.7
Propeller Twist	6.852	6.817	4.547	5.564	6.875	6.000	–11.4 ± 5.3
Opening	0.159	0.121	0.362	-0.067	0.240	2.375	0.6 ± 3.1
Tilt	-0.495	0.022	0.234	0.001	0.355	0.116	–0.1 ± 2.5
Roll	-1.323	-3.150	-4.914	-4.560	-2.632	-2.122	0.6 ± 5.2
Twist	32.394	32.094	32.743	32.566	32.172	32.170	36.0 ± 6.8
Geometries (nm)							
Shear	-0.019	-0.014	-0.010	0.025	-0.006	0.013	0.00 ± 0.21
Stretch	-0.009	-0.025	-0.017	-0.010	-0.005	-0.002	–0.15 ± 0.12
Stagger	0.005	0.022	0.045	0.004	0.012	0.009	0.09 ± 0.19
Shift	-0.012	0.000	-0.016	-0.002	-0.005	0.011	–0.02 ± 0.45
Slide	-0.029	-0.037	-0.037	-0.030	-0.040	-0.037	0.23 ± 0.81
Rise	0.385	0.394	0.377	0.381	0.386	0.369	.332 ± 0.19

All sequences were simulated for 5μs ($5x10^7$ steps) at 300 K.
*The sequence notation gives the repeat pattern of the primer strand (5'-3')
‡ Olsen parameters[13]

Finally, the location and tangent vector of the helix axis (which is used to find inter-base pair parameters such as rise and twist, and also the bending persistence length) are defined such that a rotation and translation along the tangent vector take the frame on base pair n into coincidence with the frame on base pair n+1. The x axis for this frame (which is used to find the torsional persistence length) is perpendicular to the tangent vector at an angle half way between the x axes of the two base pair frames; the *y* axis is the tangent vector cross *x*.

Averages were calculated over the last 60% of a 5 μs, 300K run. All sequences are stable with very little conformational variation between them. Their common geometry has a somewhat larger rise per base pair (about 0.40 nm vs 0.34 nm) and smaller twist angle (about 32 degrees vs 36 degrees) than canonical B-form DNA. The large rise is caused by the core size of base-body beads, which is necessary to reduce the size of the hollow at the center of the base-body triangle and allow the bases to stack reasonably flat on one another. The large rise does not affect the mechanical or thermodynamic properties reported here, but may become an issue for interactions between the model DNA and proteins or other molecules.

3.2.4 Residue Potentials

3.2.4.1 Q4 POTENTIAL

The three body beads of the bases account for the size and stacking energy of the bases. To get base stacking distances close to the canonical value of 0.34 nm, the Q4 radius, R_0, for B beads must be close to 0.21 nm. The stiffness parameters k_0 and k_1 were chosen to be soft enough to allow a small amount of bead clash (but no large overlaps) at

finite temperatures, and to limit the range of the Q4 potentials to nearest-neighbor bases. According to Sponer et al.[89] base stacking energy in vacuum is about 50-59 kJ/mol for four stacked bases in two pairs. Calculations show that a Q4 well depth for base body beads of about 5.9 kJ/mol yields about 59 kJ/mol per stack (with variations depending on sequence).

Several sources[90, 91] give the H-bonding energy at about 29 kJ/mol vs vacuum. Since the H-bonding beads are set up to be close to their minima in the equilibrated DNA, the Q4 well depth for D-A pairs was set to about 29 kJ/mol. Parameters for the Q4 potential (see Equation 4) are listed in Table 2.

Table 3: Quad-4 Parameters

Bead Type	Role	B	D	A	P
B	base shape	V_0: 9.03 R_0: 0.42 k_0: 4.10 k_1: 0.82	V_0: 0.0 R_0: 0.26 k_0: 4.10 k_1: 4.10	V_0: 0.0 R_0: 0.26 k_0: 4.10 k_1: 4.10	V_0: 6.62 R_0: 0.51 k_0: 4.23 k_1: 0.85
D	H-bond donor	V_0: 0.0 R_0: 0.26 k_0: 4.10 k_1: 4.10	V_0: 0.0 R_0: 0.10 k_0: 4.10 k_1: 4.10	V_0: 30.1 R_0: 0.10 k_0: 4.10 k_1: 4.10	V_0: 12.0 R_0: 0.35 k_0: 4.23 k_1: 1.44
A	H-bond acceptor	V_0: 0.0 R_0: 0.26 k_0: 4.10 k_1: 4.10	V_0: 30.1 R_0: 0.10 k_0: 4.10 k_1: 4.10	V_0: 0.0 R_0: 0.10 k_0: 4.10 k_1: 4.10	V_0: 12.0 R_0: 0.35 k_0: 4.23 k_1: 1.44
P	backbone shape	V_0: 6.62 R_0: 0.51 k_0: 4.23 k_1: 0.85	V_0: 12.0 R_0: 0.35 k_0: 4.23 k_1: 1.44	V_0: 12.0 R_0: 0.35 k_0: 4.23 k_1: 1.44	V_0: 4.82 R_0: 0.60 k_0: 4.37 k_1: 0.88

Units: V_0: kJ/mol R_0:nm $k_{0,1}$:N/m

3.2.4.2 COVALENT BONDS

In the DNA residues, bead T serves only as a backbone bonding site and has no interactions except a harmonic link to the P bead on the next residue in the chain. Smith et al.[92] estimated the stretch modulus of ssDNA at about 400 pN by fitting data from laser tweezers stretching of DNA to the Extensible Freely Jointed Chain model (though this value seems to be quite model-dependent)[93]. The backbone force constant (see Equation 2) was set to k ≅ 1000 pN/nm = 602 kJ/mol/nm^2, which corresponds to a stretch modulus of $k_{sm} = k \cdot d_0 \cong 1000$ pN/nm x 0.7 nm ≅ 700 pN. This value is within the experimental range and produced a good match to experiment for both bending and torsional persistence lengths.

3.2.4.3 CHARGED BEADS

The P bead is the only charged site. From Tan and Chen[94, 95] the electrostatic repulsion energy is roughly 8 kJ/mol per base pair for dsDNA in 0.1M NaCl. This energy is also roughly proportional to length of helix, especially for longer helices. With a dielectric of 80, a charge of -1 on the phosphate, and a Debye length of 1 nm (corresponding to about 0.1 M NaCl), the electrostatic energy of the model DNA is about 4 kJ/mol per base pair (see Equation 3). Two charges in high dielectric medium (water), both near a plane interface with a lower dielectric medium (like the interior of the DNA), interact as if they had higher effective charge. The effective charge is $q_{eff} = \frac{2\varepsilon_1}{\varepsilon_1 + \varepsilon_2} q$, where ε_1 is the high dielectric and ε_2 is low, and q is the real charge. The geometry of the DNA is quite different from a simple dielectric interface, but the qualitative effect should be in the same direction and not too different in magnitude. For $\varepsilon_1 \cong 80$, and $\varepsilon_2 \cong 4$, q_{eff} is

$2q$. This suggests we change the effective phosphate charge and/or dielectric constant, with corresponding changes in Debye length, to give another factor of 2 to the repulsion energy. A reasonable compromise seems to be a dielectric constant of about 50, a Debye length of about 0.8, and a charge of about -1.6e.

3.2.4.4 FRICTION COEFFICIENTS

Translational and rotational friction coefficients (see Equation 16) needed for this Brownian simulation were estimated using Stokes law(s). The translational friction is $\gamma_{trans} = 6\pi\eta R_{\text{and}}$ $\gamma_{rot} = 8\pi\eta R^3$ is the rotational friction, with an effective residue radius, R, of about 0.3 nm and viscosity, η, of 1 cP (water). Centers of friction are calculated as a weighted average of beads and shell points.

3.2.4.5 SOLVENT MODEL

The solvation values (ΔG_i^{free}, see Equation 13) for the DNA residues were initially estimated by comparing the average model solvation energy differences for stacking and H-bonding to reported values. For an equilibrated $A_{50}T_{50}$ dsDNA, the (calculated and measured) literature value is about 17 kJ/mole per base pair stack[86] and 4.2 kJ/mol per H bond[85], respectively. Initial model values were adjusted in two ways: 1) The interaction energies for $A_{20}T_{20}$ DNA were time averaged for a 5 μs run at 300K. (With a time step of 0.1 ps, 25 ns was long enough for the CG model to reach equilibrium. See Figure 10 for a graphical example). These energies were then compared with experimental results,[85, 86] and interaction parameters were adjusted to obtain as close a match as possible without sacrificing model stability. 2) Thermal bending and twisting fluctuations were collected in long runs (100 ns to 10 μs) with long dsDNA (50 to 200

bp). The fluctuations were then used to compute bending and torsional persistence lengths. The ΔG_i^{free} values were systematically varied to bring both lengths as close as possible to the measured values while keeping the base-to-base interaction potential curves within limits. Parameters for the solvent model are listed in Table 3.

Table 4: EEF1 Parameters

Bead Type	Role	ΔG^{free} (kJ/mol)	V (nm^3)	R (nm)	f_0	λ (nm)
B	Base Body	-30.1	0.0524	0.21	0.20	0.35
D	H-bond donor	-72.2	0.000	0.05	0.366	0.35
A	H-bond acceptor	-72.2	0.000	0.05	0.366	0.35
P	backbone shape	-42.1	0.153	0.30	0.135	0.35

3.2.5 Intrastrand and Interstrand Energies from All-Atom Molecular Dynamics

As a test of the important energies of the coarse-grained model, a series of simulations were carried out on DNA with full atomic detail using NAMD and the CHARMM force field[24, 31, 96]. The simulations were carried out only after the parameter values for the coarse-grained model had been determined by independent means, without adjustment of the all-atom force fields.

A series of 11 short double-stranded DNA molecules— $A_{10}T_{10}$ through $A_{20}T_{20}$— were simulated in explicit TIP3P water in the NVT ensemble, using periodic boundary conditions (5.3 nm x 5.3 nm x 8.5 nm box) and particle mesh Ewald electrostatics with distance-dependent dielectric. After initial energy minimization and equilibration, the interaction energy between residues on the same strand ("intrastrand energy"), and the interaction energy between residues on opposite strands ("interstrand energy"), were

collected over runs of 212.5 ps each. To facilitate comparison with the coarse-grained model, the energies include only through-space (van der Waals and electrostatic) interactions between atoms on different residues. Bonding forces, forces between atoms on the same residue, and forces due to solvent were included in the simulations but their energies were excluded from the reported values. The intrastrand energy is due mostly to stacking interactions, and the interstrand energy is due mostly to base pair hydrogen bonds.

Plots of average intrastrand and interstrand energies vs helix length (in base pairs) gave excellent straight lines (see Figure 13). Their slopes give intrastrand energy per base pair of -73.0 kJ/mol and interstrand energy per base pair of -58.2 kJ/mol. For comparison, coarse-grained DNA with the same sequences as above were run for 2 μs. Averaging equivalent intrastrand and interstrand energies (backbone stretching energy and solvent energy excluded) produced plots with -70.3 kJ/mol/bp and -76.5 kJ/mol/bp for intrastrand and interstrand energies, respectively. Both numbers match as well as can be expected, given the differences in residue geometries and properties between the all-atom and coarse-grained models. The agreement suggests that these energies are qualitatively set by the common requirement for double-helical/base pair local order and long-range elastic properties.

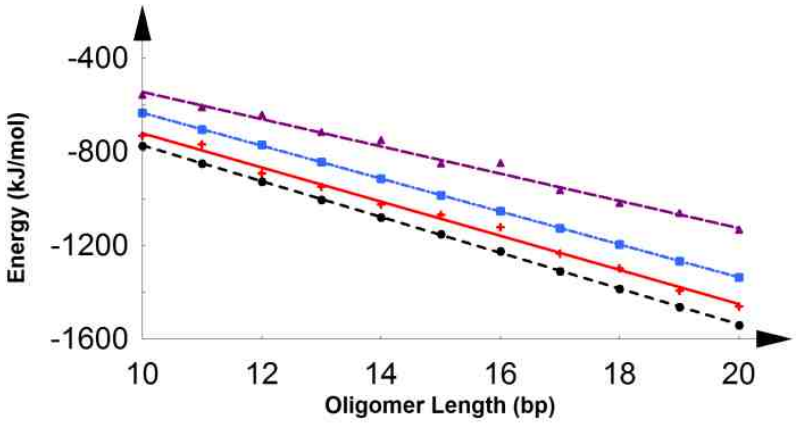

Figure 13: Average intrastrand and interstrand energies vs base pair length. Solid line (red): all-atom molecular dynamics, intrastrand energy. Long dashes (purple): all-atom molecular dynamics, interstrand energy. Dash-dotted line (blue): coarse-grained model, intrastrand energy. Short dashes (black): coarse-grained model, interstrand energy.

3.3 DNA Simulation Results

3.3.1 Persistence Length of dsDNA

Figure 14 a shows a fifty base pair model DNA (sequence $A_{50}T_{50}$) at three time points over the course of a 10 μs run (10^8 steps, 0.1 ps per step) at 300 K. The initial conformation, shown in the first frame, is ideal B-form (rise per base pair 0.34 nm, twist 36 degrees, 10 bp per turn). The main features of the structure are visible: the bases are set at a fixed angle to the backbone, stacked flat and perpendicular to the helix axis. In this conformation the base-body beads of stacked bases interlock in a roughly close-packed arrangement, and the H-bond donors and acceptors are paired in the base plane and visible along the major groove. During the simulation, the individual base pairs jostle their neighbors as their hydrogen bonds and stacking contacts lengthen or compress. On longer length scales the double-helix exhibits bending and twisting fluctuations, while the entire DNA molecule slowly diffuses both translationally and rotationally.

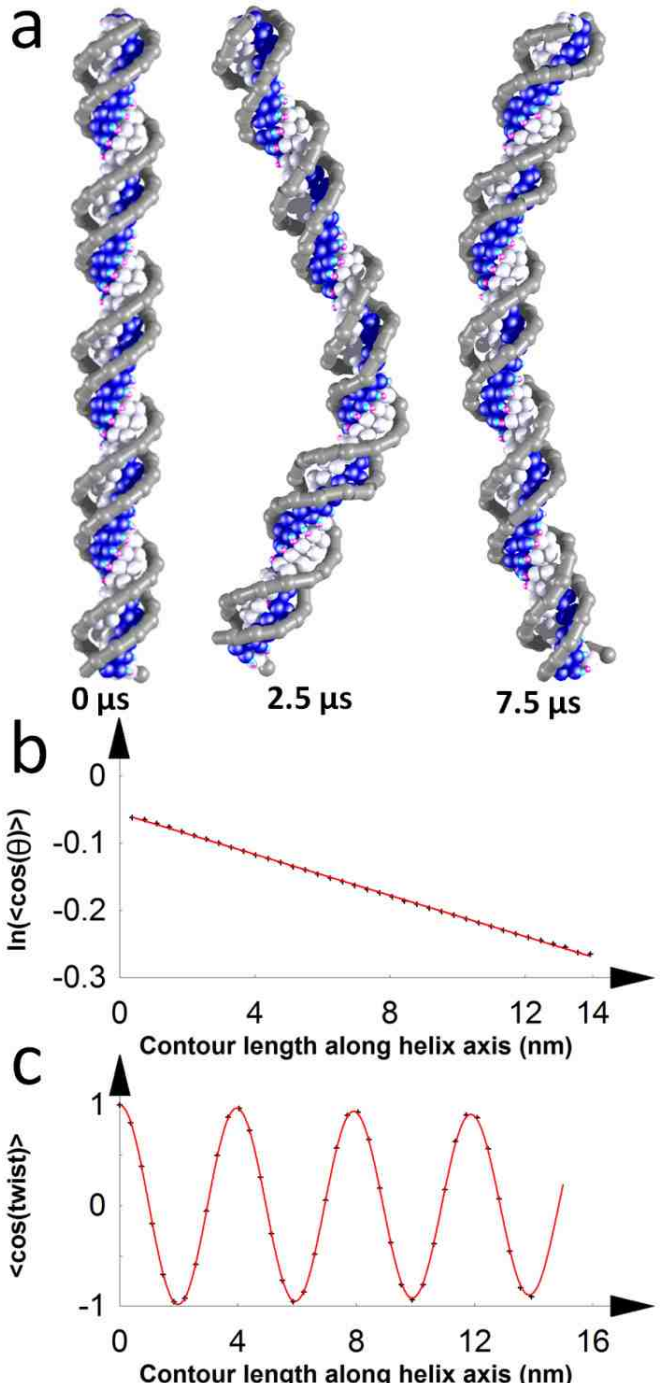

Figure 14: Persistence lengths of DNA (a) Still frames from a 10 µs (10^8 step) run for an $A_{50}T_{50}$ DNA sequence. The initial conformation, shown in the first frame, is ideal B-DNA. (b) Logarithmic plot of the bending-angle correlation function for $A_{50}T_{50}$, for a 5 µs (5×10^7 step) simulation. The negative slope is the bending persistence length. (c) Logarithmic plot of the torsion angle correlation function for $A_{50}T_{50}$, for a 5 µs (5×10^7 step) simulation. Red (solid) line is $\cos\left[\frac{2\pi * \text{contour length(nm)}}{\text{helical pitch (3.96 nm)}}\right] e^{\left[\frac{-\text{contour length (nm)}}{\text{torsional persistence length (120 nm)}}\right]}$

The bending and torsional persistence lengths are measures of the long-length-scale mechanical stiffness of a polymer. The bending persistence length, P, is defined by the equilibrium correlation function $\langle \hat{t}(0) \cdot \hat{t}(s) \rangle_{eq} = e^{-\frac{s}{P}}$, where $\hat{t}(0)$ and $\hat{t}(s)$ are unit tangent vectors separated by a distance s along the helical axis curve of the DNA. Similarly, we define the torsional persistence length, τ, by a correlation function $\langle \hat{n}(0) \cdot \hat{n}(s) \rangle_{eq} = cos(2\pi s/L) e^{-s/\tau}$, where $\hat{n}$ is the x axis of the frame in which the nth base pair and the n+1 base pair are related by a rotation about $\hat{t}$ and translation along $\hat{t}$ (see Chapter 3.2.3) and L is helical pitch. The cosine factor accounts for helical rotation of the base pairs, and the exponential factor represents decay of twisting correlations.

Figure 14b shows a graph of log correlation function for an $A_{50}T_{50}$ sequence. The slope gives the persistence length. Correlation functions for 50 bp double helices were determined by collecting bending and twisting fluctuations over $2x10^7$ time steps (2 μs), yielding an average bending persistence length of 55 ± 6 nm across all 6 sequences. (Runs of 1 μs were not fully equilibrated; runs of 5 μs gave the same answers as the 2 μs runs.) The persistence length depends quite strongly on sequence, with P = 66 nm for $G_{50}C_{50}$ and P = 50 nm for $A_{50}T_{50}$. All values are sensitive to the parameters of the model force field, including the strength and stiffness of the basic stacking and H-bonding potentials, the spring constant of the harmonic links in the backbone, and the free energies of solvation. The experimentally measured bending persistence length for long double-stranded DNA is about 50 nm, depending somewhat on sequence, temperature, and buffer conditions.[92, 97, 98] The average torsional persistence length of 120 ± 42 nm was obtained by fitting the torsional correlation function for $A_{50}T_{50}$ for double helices

that were allowed to equilibrate at 300 K for $5x10^7$ time steps (5 μs, Figure 14c). (Runs of 10 μs yielded very similar persistence length values.)

3.3.2 Mismatches

By design, non-complementary base pairings are disfavored by their size, by clashes between donor-donor or acceptor-acceptor pairs, and/or by non-optimal hydrogen bonding distances. Thermal stability for matched pairs and instability for mismatched pairs is a necessary, but not sufficient, condition for a DNA model that is capable of full sequence recognition, and hence capable of transmitting genetic information (the fundamental function of real DNA). Mismatch stability is part of the larger issue of the general melting properties of the model (melting temperature, enthalpy, entropy and structural properties), which are not yet fully developed or optimized.

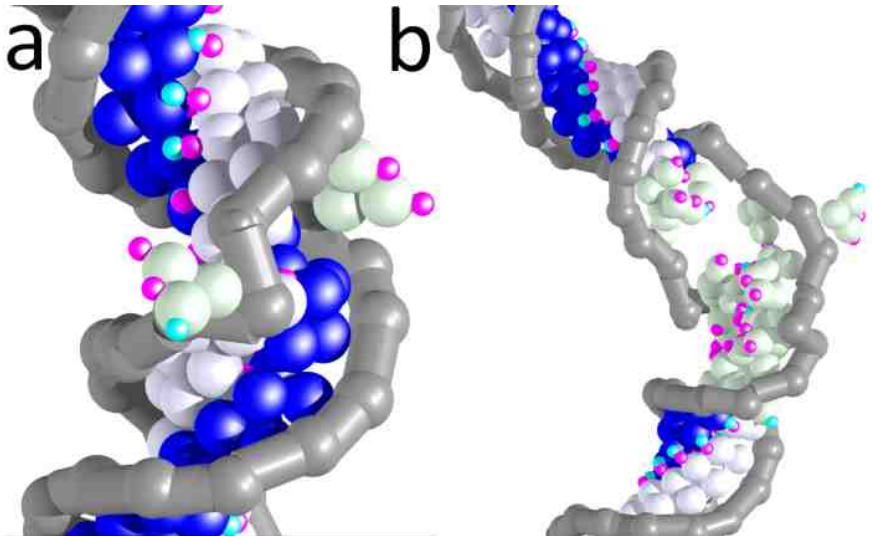

Figure 15: DNAs containing G-G mismatches. (a) DNA with 49 correctly paired bases and a single G−G mismatch. The frame shown is about 250 ns into a 2-μs run. The mismatched base pair has unpaired and flipped out of the helix. (b) DNA with two 20 bp stems flanking a ten-base G−G mismatch region. The frame shown is about 1.8 μs into a 2 μs run. The G−G region has taken on an unpaired, melted arrangement.

Figure 15 shows two DNAs containing G-G mismatches, one of the most unfavorable mispairings. Figure 15a is a frame from a 100 ns run with a DNA that has 49 correctly paired bases and a single G-G mismatch, which has flipped open to face the "solvent" rather than remain paired. Figure 15b shows a similar system with two 20 base pair complementary stems flanking a ten-base G-G region. The two correctly paired regions are stable and well ordered, but the mismatched region has become completely disordered. In a series of 1 μs runs, all complementary sequences remained paired at all times, but in eight of the twelve cases the mismatched pairs became disordered within 100 ns. Four cases—5'CT3' or 5'TC3' and 5'GA3' or 5'AG3'—remain paired, though the mispaired regions show less order than the complementary stems. These quasi-stable sequences are cases that are still able to form two hydrogen bonds each, despite the mismatch.

3.3.3 Melting

Determining the melting curve of DNA presents a computational challenge due to the high degrees of freedom built into the model. There are many half-melted globular conformations that form metastable energy traps when transitioning from a nonmelted (majority of bases paired) to a clearly melted state (two strands fully separated). Therefore, REMD was implemented in order to help find the melting curve for the DNA. The implementation of is technique is still undergoing parameter refinement, but initial runs have yielded an early melting curve for the DNA (see Figure 16). A 10 μs, 7 thread REMD melting simulation of an $A_{10}T_{10}$ (with temperatures of 380 K, 405 K, 430 K, 440 K, 450 K, 475 K, and 500 K) was run and analyzed using WHAM. Assuming base pairs

are unpaired when the hydrogen bonding beads are greater than 0.35 nm apart (3.5 times the ideal bonding distance), results indicate that the DNA only fully melts at relatively high temperatures, with 50% melted at ~440 K for the model vs ~330K for real DNA. This indicates the model potentials are too strong and/or are too long-ranged to accurately replicate DNA melting. But while this result does not agree with experimental values, it should be noted that the DNA was constructed to work with polymerase at biological temperatures. The system was not initially built with the intent to accurately reproduce DNA melting, and many of the current potential parameters (such as the Screened Coulomb or Q4 potentials) contain set values that do not scale with increased temperature. With modifications to these potentials and refinement of the parameter values the melting temperature could be lowered to realistic values.

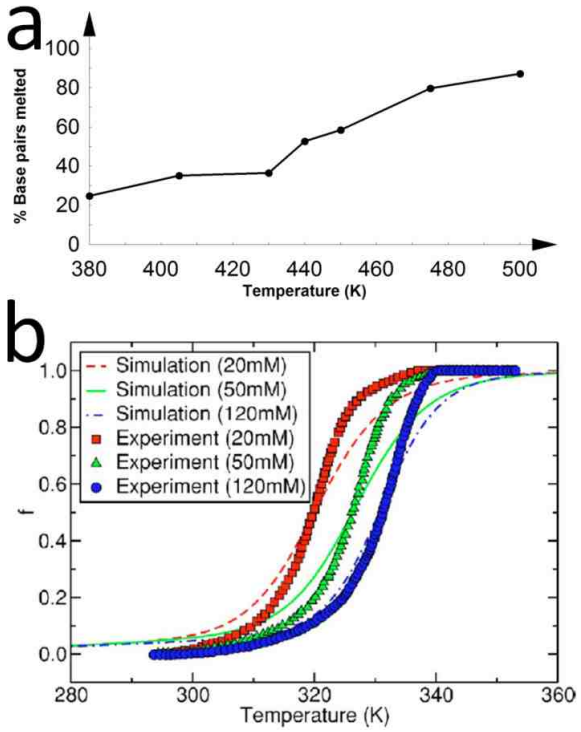

Figure 16: (a) Melting curve for the TM2 DNA model. The y-axis shows the percentage of bases in a $A_{10}T_{10}$ strand that are melted (here defined as separated by more than 0.35 nm). Early results indicate the melting point is approximately 440 K. (b) Experimental and simulated melting curves for short (~100bp) DNA from the results of Knotts et al.[21] comparing their DNA model to real DNA.

3.3.4 Single-stranded DNA

Single-stranded model DNA (with no self-complementary regions) show high flexibility (persistence length 0.67 nm, with loss of all backbone correlation after a few residues), with transitory local base stacking and non-Watson-Crick hydrogen bonding. If the solvent model is turned off, such single-stranded chains collapse into a compact but unstructured ball. With the solvent model active, ssDNA adopts extended conformations that show a variety of local and transient structures (Figure 17a-d). To help understand these structures, Figure 17e shows a "Ramachandran plot" of the local backbone bending angles (called phi and psi here). The plot represents the local (phi, psi) configuration of all residues in 10,000 snapshots taken from a 3 μs run, starting from a molecule that had been pre-equilibrated for 8 μs. Plots made from longer and shorter runs are similar (though they differ in some details), so Figure 17e is roughly representative of the equilibrium configurational populations. Three broad regions, labeled RH, LH, and K, show high population density. By comparison with a phi-psi plot from a double stranded molecule, (Figure 17e insert), region RH can be identified as the residual right-handed double helical conformation, similar to the structure shown by the central and top regions in Figure 17a. A similar statistical helix formation has long been known in real ssDNA, mainly from circular dichroism measurements[99], and is also seen in all-atom simulations of short ssDNA molecules[100], and in coarse-grained models[52]. Region LH corresponds to a left-handed helix with a large radius, as seen in Figure 17b; and region K represents pairs of adjacent bases with a sharp backbone kink that allows the bases to quasi-stack on each other. The K configurations are less common than RH and LH, and appear mainly

at the ends of the chain. Figure 17c,d show representative conformations containing small regions of RH, LH, and K.

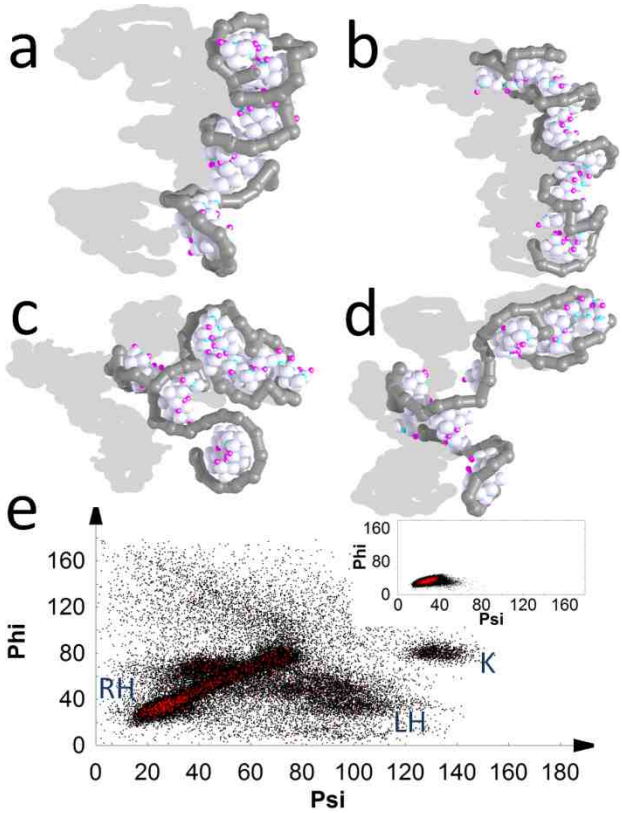

Figure 17: Single-stranded DNA. (a−d) Still frames from a 3 μs run for a single-stranded DNA sequence A_{50}, starting from a molecule that was pre-equilibrated for 8 μs. (a) ssDNA showing a largely right-handed helical conformation. (b) ssDNA showing a left-handed helical structure. (c,d) representative ssDNA conformations. (e) "Ramachandran plot" of the local backbone bending angles. Phi and psi are the polar angle and azimuthal angle, respectively, of the z axis of base pair n + 1 in the frame of base pair n. High-population-density regions are labeled RH, LH, and K, for right-handed, left-handed, and backbone kinks, respectively. The inset is a phi−psi plot of the A strand from a doublestranded $A_{50}T_{50}$ DNA.

3.3.5 Closed dsDNA Loops and Writhe Calculation

The circular DNA in Figure 18 are covalently closed molecules of 109 AT base pairs each. Linear, unclosed molecules of this sequence have an average twist of about 11 bases per turn, so a loop of 109 bases with 10 helical turns (linking number 10) approximates an unstrained circle. The molecules in Figure 18a,c-f have linking numbers

of 10, 9, 8, 11, and 12, corresponding to net under-or-over winding, Δlk, of 0, -1, -2, +1, and +2 turns, respectively. The molecules were initially created in ideal B-conformation, then relaxed for 10 ns at zero temperature, followed by equilibration at 100 K for 1 μs, and then runs of 2 μs at 300 K. The images in Figure 18 are snapshots from late in the runs at 300 K.

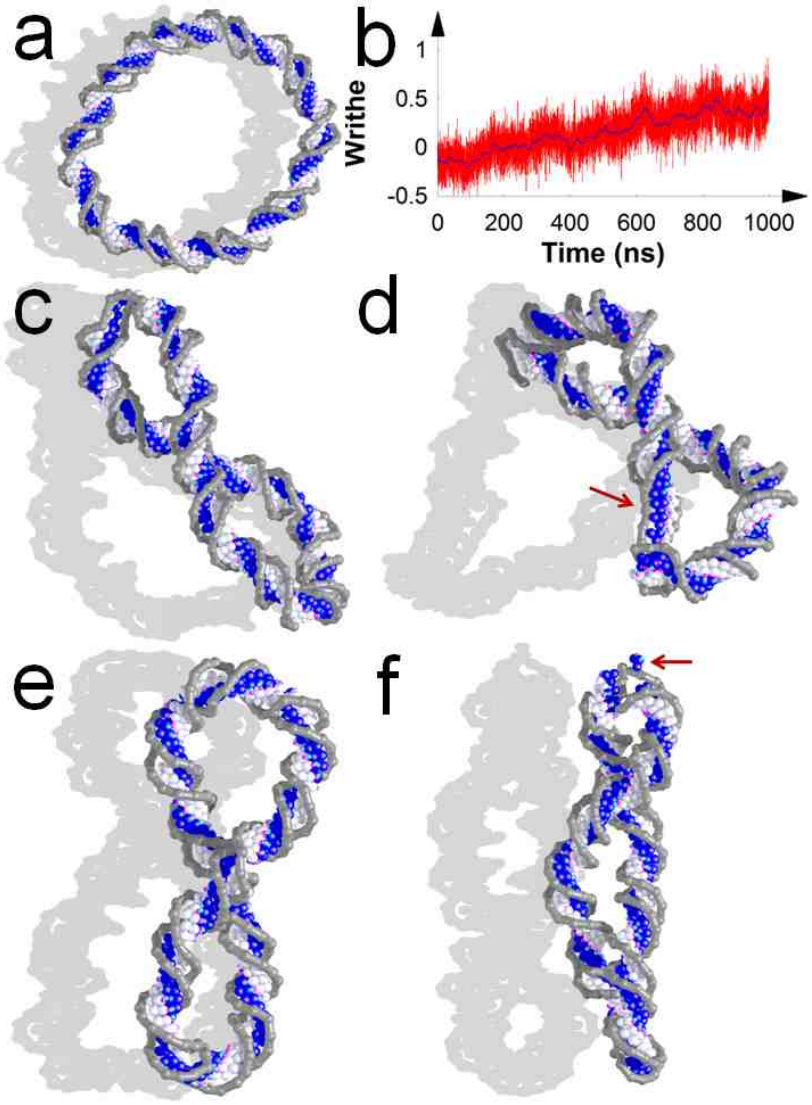

Figure 18: Supercoiling of closed 109-bp DNA loops. (a) Linking number 0, which results in an unstressed loop. (b) Writhe as a function of time for the molecule in panel e. (c) Linking number −1. (d) Linking number −2. The undertwisting stress is relieved in part by a ribbonlike conformation (arrow). (e) Linking number +1 (f) Linking number +2. Overtwisting stress is relieved by a flipped-out base at the top of the loop (arrow).

The writhe of fluctuating closed DNA loops was calculated at each time point according to method 1a of Klenin & Langowski[101], using a discrete version of the Gauss integral:

$$wr = 2\sum_{i=2}^{N}\sum_{j<i}\frac{\Omega_{ij}}{4\pi}$$

Equation 20

where each sum is over base pairs, and

$$\Omega_{ij} = [\arcsin(\boldsymbol{n}_1 \cdot \boldsymbol{n}_2) + \arcsin(\boldsymbol{n}_2 \cdot \boldsymbol{n}_3) + \arcsin(\boldsymbol{n}_3 \cdot \boldsymbol{n}_4) + \arcsin(\boldsymbol{n}_4 \cdot \boldsymbol{n}_1)]sign\{(\boldsymbol{r}_{34} \times \boldsymbol{r}_{34}) \cdot \boldsymbol{r}_{13}\}$$

Equation 21

with

$$\boldsymbol{n}_1 = \frac{(\boldsymbol{r}_{13}\times\boldsymbol{r}_{14})}{|\boldsymbol{r}_{13}\times\boldsymbol{r}_{14}|}; \boldsymbol{n}_2 = \frac{(\boldsymbol{r}_{14}\times\boldsymbol{r}_{24})}{|\boldsymbol{r}_{14}\times\boldsymbol{r}_{24}|}; \boldsymbol{n}_3 = \frac{(\boldsymbol{r}_{24}\times\boldsymbol{r}_{23})}{|\boldsymbol{r}_{24}\times\boldsymbol{r}_{23}|}; \boldsymbol{n}_4 = \frac{(\boldsymbol{r}_{23}\times\boldsymbol{r}_{13})}{|\boldsymbol{r}_{24}\times\boldsymbol{r}_{13}|};$$

and $\boldsymbol{r}_{13} = \boldsymbol{x}_j - \boldsymbol{x}_i; \boldsymbol{r}_{14} = \boldsymbol{x}_{j+1} - \boldsymbol{x}_i; \boldsymbol{r}_{24} = \boldsymbol{x}_{j+1} - \boldsymbol{x}_{i+1}; \boldsymbol{r}_{23} = \boldsymbol{x}_j - \boldsymbol{x}_{i+1}$

where x_i is the origin of the base pair coordinate frame for base pair i (see Chapter 3.2.3). This algorithm is less efficient than others but gives reliable and stable results on noisy curves. Closed loops must satisfy the topological constraint $\Delta lk = \Delta tw + wr$, where Δlk is the difference, $lk - lk_0$, between the equilibrium linking number and the actual linking number, Δtw, is $tw - tw_0$, the difference in helical turns from the equilibrium number, and wr is writhe, a measure of the number of supercoils. For a given molecule, Δlk is fixed but Δtw and wr may change in concert, that is, the molecule may compensate for overtwist or undertwist by forming supercoils.

In the untwisted molecule $\Delta lk = 0$, Figure 18a, the DNA is unstrained and remains in a roughly circular shape during the simulation. Figure 18c, e show loops with

Δlk of -1 and +1, respectively. Both are supercoiled and both display about half a turn of writhe, one positive and the other negative. Figure 18b shows wr as a function of time for the molecule in Figure 18e, with Δlk of +1[101]. Starting from a nearly unsupercoiled, flat loop ($\Delta tw = 1,\ wr = 0$), the molecule steadily unwinds its local twist strain by supercoiling. The molecule does not reach full equilibrium, but by the end of the run (1 μs) about half of the initial +1 overtwist has relaxed, with compensating increase in writhe.

A molecule with two turns of undertwist is shown in Figure 18d. It shows only one partial turn of writhe, but part of the loop has adopted a ribbon-like conformation, which helps relieve much of the torsional strain, and raises the contribution of Δtw versus the writhe contribution to the net linking number. Likewise, the loop with Δlk of +2 (Figure 18) shows a flipped-out base near the top of the loop. As with the ribbon conformation, the open base pair helps relieve the torsional stress on the DNA. Loops with higher values of Δlk (not shown) become tightly knotted with very sharp kinks at the ends of the supercoils, where base pairs frequently open.

3.3.6 DNA Hairpin

Figure 19 shows a hairpin-forming DNA as the molecule is first melted and then reannealed. The sequence of the molecule, 5'GGAAATTTTTTTCC3', allows the formation of a stable double-stranded stem of 5 base pairs (GGAAA complementary to TTTCC) with a five-base single-stranded loop of T residues. The molecule was originally built and equilibrated in the stem-loop structure (Figure 19a), but was melted by raising the temperature to 450 K for 100 ns. Figure 19b shows a frame from the end

of this run, with the molecule in a random extended conformation. The temperature was then lowered in steps as shown in Figure 19f. Representative structures are shown in Figure 19c-e.

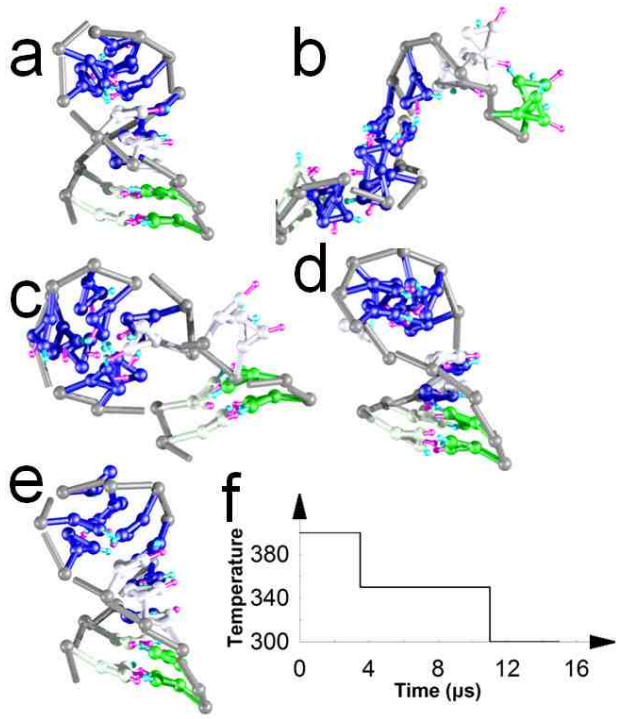

Figure 19: Hairpin-forming DNA (5′GGAAATTTTTTTTCC3′) is first melted and then reannealed. (a) Equilibrated DNA in a stem-loop structure. (b) Melted conformation taken from a run at 450 K. (c−e) Frames from the reannealing simulation: (c) at the first temperature drop (see f), (d) at the second drop, (e) at the end of the run. (f) Temperature program for reannealing.

At 400 K the two GC pairs at the end of the stem are able to form, though they also open transiently. At this point the temperature was dropped to 350 K, which allowed the three AT base pairs to form, though, as with the GC pairs, the AT pairs open and close rapidly. The temperature was then lowered to 300 K, and the original hairpin structure fully reannealed.

The molecule can form mispairs and other long-lived kinetic traps as it cools: the Ts in the loop can pair with the As in the stem; the stem As and Ts can cross-pair in the

wrong order, as can the Gs and Cs; the Ts and Cs can form rather stable non-complementary pairs; single non-Watson-Crick H bonds can form between any pair of bases. Thus, in many "blind" runs with a pre-chosen cooling program the molecule becomes trapped in such states and never forms the hairpin (at least on the ~10 μs time scale). To allow reannealing in a practical length of time, the drop from 400 K to 350 K was chosen to occur at a moment when the two GC pairs were correctly formed. After this the remaining three AT pairs formed on their own, and the molecule stabilized in the original hairpin structure at 300 K. Though the cooling process was biased in this way, the overall result shows that the final hairpin can be reached with minimal cherry picking, and the hairpin is likely to be the true global equilibrium state at 300K.

3.3.7 Long DNA runs

Finally, Figure 20 shows a snapshot from a 10 μs run with a large model DNA molecule of 250 bp with uniform repetitive sequence, $A_{250}T_{250}$. The simulation shows that the model yields stable double-stranded structure even for such large molecules on at least microsecond time scales, with no unrealistic melting, fraying, bubble formation, kinking, or other structural misbehavior. Large-scale, long-wavelength bending fluctuations are apparent, but such fluctuations did not reach equilibrium in the time course of this run.

Figure 20: Large model of DNA. Frame from approximately 3.3 μs into a 10-μs simulation of $A_{250}T_{250}$.

3.4 Conclusion

A coarse-grained DNA model that is capable of interacting with other (coarse-grained) molecular machines (either protein or nucleic acid) must look like DNA on the base pair level, and have DNA-like basic structural properties (base recognition, helical parameters, backbone interactions) and mechanical properties (bending and twisting stiffness, kinking, bubble opening, etc). These properties require residues that are capable of hydrogen bonding and base stacking, and this, in turn, requires flat base planes and specific H-bond donors and acceptors. Seven or eight beads per residue seem to be about the minimum necessary to meet this level of detail.

The results above show that such a "minimal" model can form helices with essentially canonical B-conformation that are stable over long times and under highly stressed conditions. Even when the DNA is bent sharply enough to cause local kinks, the basic helical structure reasserts itself within one or two base pairs of the defect, and base pair opening is limited to the most severe cases. In long runs (microsecond time scales and longer) helical structure remains stable despite strong bending and twisting thermal fluctuations, though base pairs occasionally open, especially at the ends. The main driving forces for helix formation in real DNA—stacking, solvent forces, H-bonding—are also the main helix-stabilizing forces in the model. The long wavelength elastic properties, as measured by bending and twisting persistence lengths, can be made to agree quite closely with experimental values. Topologically closed loops show supercoiling; large double-stranded DNA remain stable, and demonstrate the flexibility and long-wavelength fluctuations expected of long, worm-like polymers.

A fully realistic model would also be capable of reproducing complex secondary structures as well as double-stranded stems. There is little or no distinction between DNA and RNA at the present level of detail, so such a model could be used for a wide variety of RNA systems: tRNAs, ribozymes, nucleoprotein complexes, mRNAs, rRNAs, etc. The current model can address limited cases, where Watson-Crick pairing is sufficient, such as the simple stem-loop structure. But the three-dimensional folding of general RNA sequences requires a greater variety of residue-residue interactions (non-Watson-Crick base pairing, non-standard bases, residues in conformations very different from dsDNA) than the present coarse-grained residue can easily accommodate. Also, the solvent model may not be adequate to represent the wide range of solvent exposure that occurs in a folded RNA.

The ability of DNA to act as an information storage molecule results from its base pairing thermodynamics. An ideal DNA model would reproduce these thermodynamics and thus have the same base recognition, melting, and annealing behavior as DNA. The current model falls short of this ideal, but the H-bonding donors and acceptors have been arranged so that AT and GC base pairs are strongly favored at room temperature. Mismatches vary in behavior; the most unstable (GG, AA, and GA pairs) immediately disorder and would presumably come apart into separate strands if the molecule had no other base pairs. The most stable mispairs (GT and AC) show increased disorder, but may never melt completely. At high temperature all sequences disorder on long time scales, and at very high temperature the strands separate completely and rapidly. This occurs naturally at much higher temperatures than true DNA, but those temperatures could be lowered with a focused adjustment of the potential parameters. In all, these

results are a step toward showing that, with further refinement, TM2 coarse-grained DNA is capable of fully reproducing DNA base pairing and base-recognition thermodynamics. With such mechanics in place, the DNA is ready to be combined with a CG model of DNA polymerase.

4. THE POLYMERASE MODEL

4.1 Background

DNA polymerases are multidomain enzymes responsible for DNA replication, repair and legion bypass via the incorporation of free deoxynucleoside triphosphates (dNTPs). Nucleotide incorporation occurs along the single-stranded DNA primer strand as determined by the complimentary single-stranded template. All known organisms utilize enzymes of similar structure and mechanism for DNA replication and maintenance.

DNA polymerases have over 10^7-fold variance in fidelity of correct nucleotide insertion, depending upon their function[102]. As the preservation and propagation of genetic information is essential for life, replication and repair polymerases have the highest fidelity, with an average fidelity range of 10^{-4} to 10^{-6}, that is, 1 error per 10,000 to 100,000 nucleotides incorporated.[103-108] This is increased to 10^{-8} with the addition of proofreading domains and other error-checking proteins[103, 109]. On the lower fidelity end, polymerases designed to handle damaged DNA can have a range of 10 to 100.[103, 107] How polymerases achieve such fidelities is an active area of research, as it involves complicated interactions between the active site residues and the substrates.[102-105, 107-125]

Depending upon their primary sequence alignment, DNA polymerases are often classified into five to seven families; A, B, C, X, and Y, with D and RT sometimes specified.[103, 107, 121, 125-127] Membership in a given family is based on sequence rather than organism, function, or location in the cell. For example, Pol γ, a polymerase responsible for mitochondrial DNA replication[102, 103], is grouped in family A along with Pol θ, a

genomic DNA replication and repair polymerase[103, 120, 128], and Pol T7, a replication polymerase found in the bacteriophage T7[112, 113, 122, 129, 130]. However, some generalities across the different families can be made. Most of the DNA replication polymerases are found in families A, B, C, and D, with B, C and D containing the majority of polymerases found in eukaryotic, bacterial, and archaeal organisms respectively. Members of the X family are usually involved in DNA repair, such as the smallest cellular polymerase Pol β.[13, 108, 110, 119, 121, 125, 126, 131-134] Almost all of the Y family, along with B family member pol ζ, have relatively low fidelity as they are responsible for replicating damaged DNA, bypassing legions that would trap higher fidelity polymerases.[103, 107, 125]

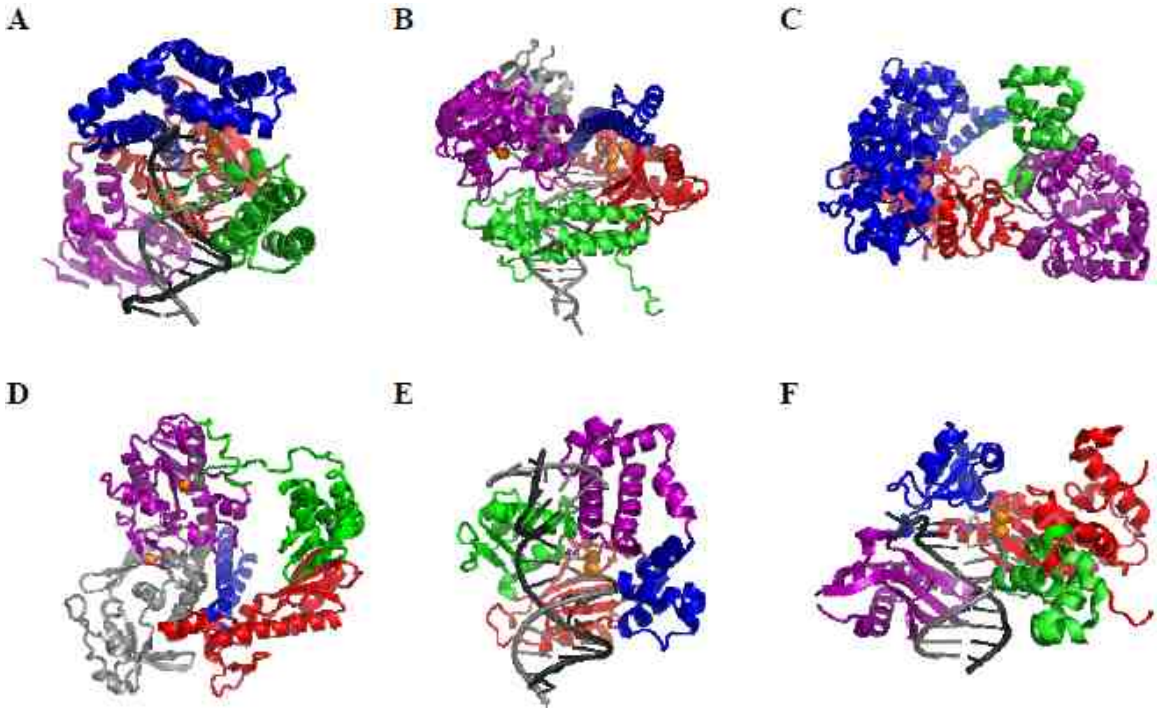

Figure 21: Crystal structures of several representative DNA polymerases. A representative member is shown for each family: (A) Klenow fragment of *Thermus aquaticus DNA polymerase I* (PDB 3KTQ) from family A, (B) RB69 DNA polymerase (PDB 1IG9) from family B, (C) *E. coli DNA Pol III (PDB 2HNH)* from family *C, (D) Pfu* polymerase *(PDB 2JGU)* from family *D, (E)* human Pol β (PDB 1BPY) from family X, and (F) human Pol η (PDB 3MR2) for family Y.Three main domains are colored blue for the fingers domain, red for the palm domain, and purple for the thumb domain. The DNA primer and template strands are light and dark gray, respectively. Image taken from Brown et al. 2010.[103]

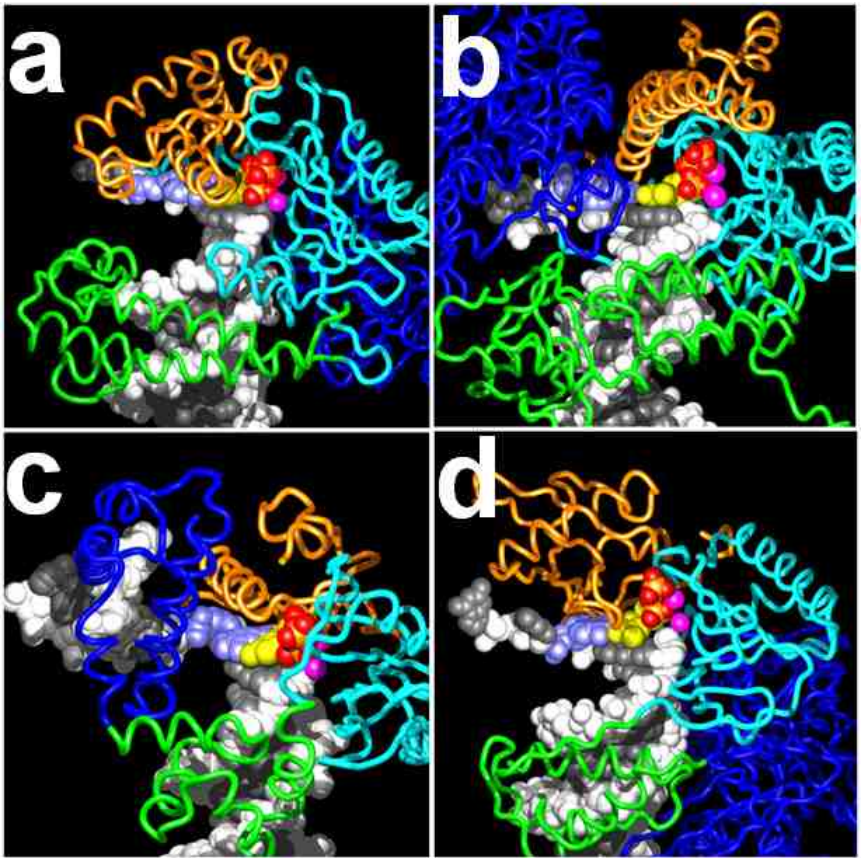

Figure 22: Crystal structures of four DNA polymerases each with the similar orientations. (a) Taq polymerase from family A. (b) RB69 polymerase from the B family. (c)Pol β polymerase from family X. (d)Reverse Transcriptase from the HIV family. Three main domains are colored blue for the fingers domain, orange for the palm domain, and green for the thumb domain. The incoming nucleotide is yellow and the DNA primer and template strands are light and dark gray, respectively.

Across all the families and regardless of function, all DNA polymerases contain three highly conserved domains called the "thumb," "fingers," and "palm" after their topological analogy to a right hand. (Sometimes these regions are classified as "subdomains.") Figure 21 from Brown 2010[103] shows example crystal structures from six of the polymerase families where the conserved domains are colored blue for the fingers, red for palm, and purple for the thumb. Figure 22 shows four example crystal structures of DNA polymerases each with the similar orientations.

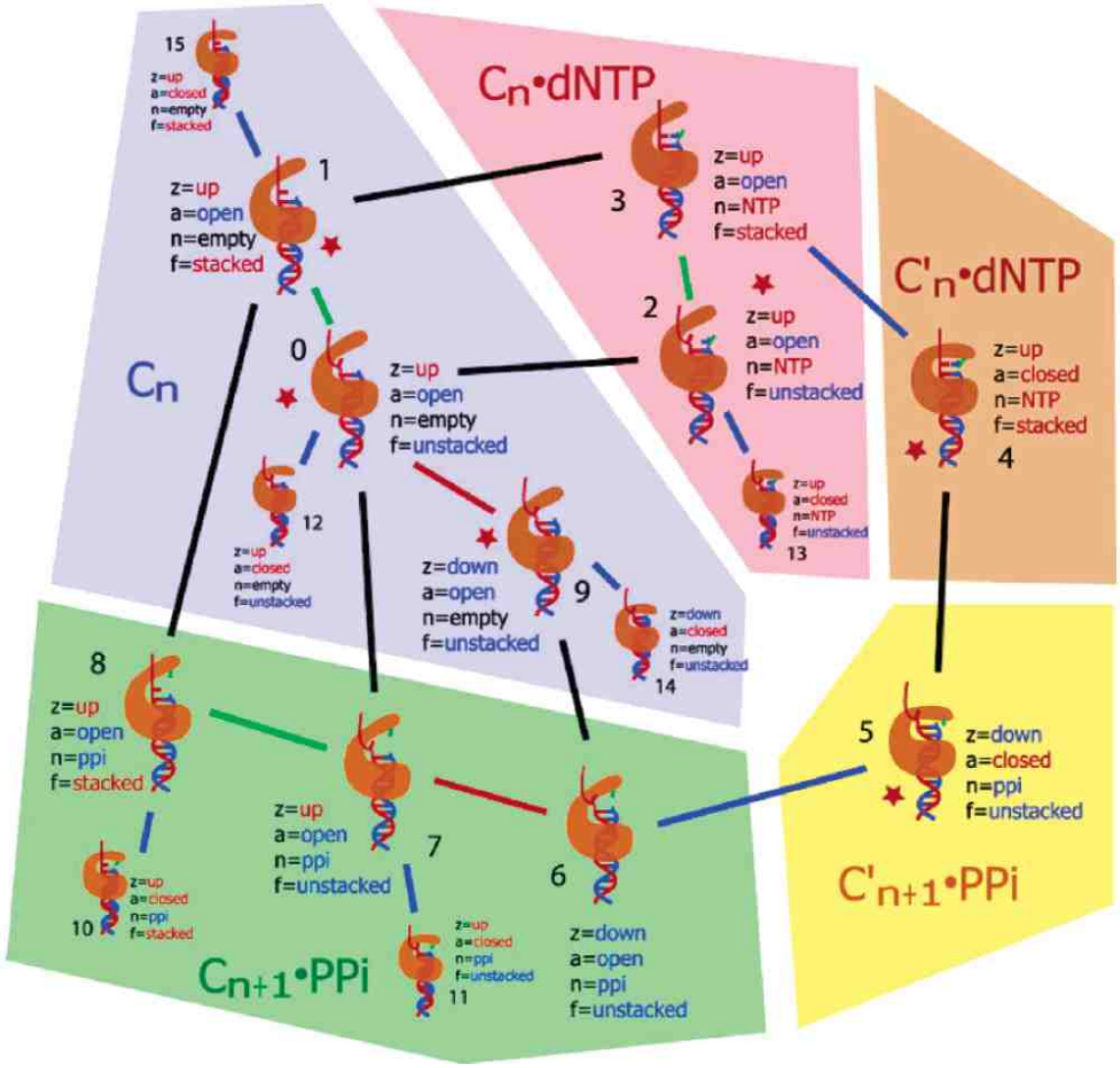

Figure 23: Sixteen reasonable conformational states of DNA polymerase. Each state is labeled by the parameters z (position of the polymerase on the DNA), α (state of the fingers domain), f (state of the template strand), and n (the presence of a bound nucleotide). Lines are colored blue for fingers closing, red for translocation, green for template base stacking, and black for a chemical change. Discrete colored domains correspond to known kinetic mechanisms where the labels Cn, dNTP, and PPi represent the protein-DNA complex, a nucleotide, and a pyrophosphate respectively. Conformations 0-9 represent a standard polymerization cycle. Image taken from Keller and Brozik 2005[106].

Polymerases add nucleotides to the 3'OH end of an existing DNA primer strand, forming the double-strand DNA along the 3' to 5' direction of the template strand (since the primer and template strands are antiparallel). The thumb binds along the minor groove of the double-stranded DNA substrate and is involved in positioning, processivity,

and translocation of the polymerase. The fingers domain undergoes a conformational change between an "open" state, where it allows incoming dNTPs to bind to polymerase and releases the pyrophosphate (PPi), and a "closed" state where it forms a tight catalytic pocket with the palm domain. This domain plays a major role in the selection of the correct nucleotide and synchronization of the overall catalytic cycle. The palm is positioned near the 3' OH group at the end of the primer stand and coordinates with the phosphates of the incoming dNTP. The palm contains the active site with amino acid residues that coordinate the two divalent metals (usually Mg^{2+}) necessary for the catalysis of the phosphoryl transfer reaction that will link the nucleotide to the growing primer chain. These three domains are functionally equivalent across most polymerases, despite the variability of sequences across families. Beyond these conserved domains, the remainder of the protein varies dramatically depending upon the function of the polymerase.[103, 106, 121, 125, 135]

A large library of DNA polymerase crystal structures has been catalogued[102, 103, 105, 106, 108-110, 114-116, 131-133, 136-140], along with a wealth of kinetic and thermodynamic data for a wide range of polymerases[13, 62, 103, 104, 106, 108, 110-112, 115, 116, 118, 119, 122, 126, 133, 135, 139, 141-150]. Following Keller and Brozik 2005[106], sixteen states are shown in Figure 23 where four degrees of freedom are necessary to describe each state; z, α, f, and n. The degree of freedom z describes the position of the polymerase on the DNA where "down" is the initial state of the protein and "up" is the final state of the protein after nucleotide addition and translocation. α is used to represent the "open" and "closed" state of the fingers domain. f describes the template strand where the basepairs can be in a "stacked" or "unstacked" conformation. n tracks the presence of a bound nucleotide, "NTP", or a

bound pyrophosphate, “PPi”, or an “empty” state where neither compounds are present. For the sake of convenience and simplicity, the first three variables are each restricted to two values and n to three values. Within a single polymerization cycle, there are six different enzyme conformations known from the crystal structures. However, there are sixteen possible and physically reasonable conformational states that polymerase could adopt. Figure 23 also displays the likely transitions between the sixteen conformation sates. Lines are colored blue for fingers closing, red for translocation, green for template base stacking, and black for a chemical change (NTP binding, PPi release, or catalysis). The colored areas indicate the standard kinetic biochemical states of the enzyme, such as the C_n blue region for the state where only the enzyme is present and at its initial position. This coloring scheme is meant to highlight the difference between what has been inferred via kinetic experiments (the biochemical states) and the total conformational states available to the polymerase. The figure makes three initial assumptions: (1) It assumes that phosphodiester bond formation only occurs when a complete catalytic complex is created with the fingers domain closed and the bases stacked and paired to a nucleotide. (2) All degrees of freedom are assumed to be frozen during the bond formation reaction, meaning the enzyme does not change its conformation. (3) Transition pathways between states are assumed to involve only a single change to one of the four variables, ignoring possible simultaneous changes in favor of the fastest transition along the four degrees of freedom.[106]

The conformational transitions between states 0-9 represent a pathway that catalyzes a polymerization cycle. A free dNTP in solution diffuses to the active site when that site has been made accessible by the opening of the fingers domain. The dNTP

binding facilitates a conformational change to the fingers domain. Once a base on the template strand is stacked, and if the dNTP is complementary to the base, the fingers domain can close completely and create a catalytic pocket with the palm domain. The two catalytic metal ions (designated A and B) in the palm region play a key role in the nucleotidyl transfer reaction. Metal A lowers the pKa value of the′3 -OH on the primer strand while metal B stabilizes and orients the triphosphates and subsequent PP_i leaving group, as shown in Figure 24 taken from Castro et al. 2007[151]. Deprotonation of the stabilized 3'-OH results in an attack by the nucleophilic oxygen anion on the α-phosphate. Kinetic studies of polymerase T7 and pol β suggest that the reaction proceeds through a trigonal-bipyramidal transition state formed by a pentacovalent phosphorus intermediate that is stabilized by both metals[103, 108, 126, 151]. With the newly added NTP, the negatively-charged PP_i is free to disassociate from metal B and the polymerase undergoes another conformational change to open the fingers domain. This process also causes the polymerase to translocate to the next position along the DNA, resetting the cycle.

The conformational states 10-15 in Figure 23 represent possible off-pathway "traps" that do not contribute to the polymerization cycle. These conformational states could be inaccessible due to high energy barriers and therefore not contribute to the turnover kinetics. Alternatively, they could exist in equilibrium with the known catalytic conformations and stall the polymerase in an inactive state for a period of time. Ideally, the energy barriers and rates of transitions between all the conformations should be found through various experimental studies. However, accessing that information for every step has not been feasible so far.

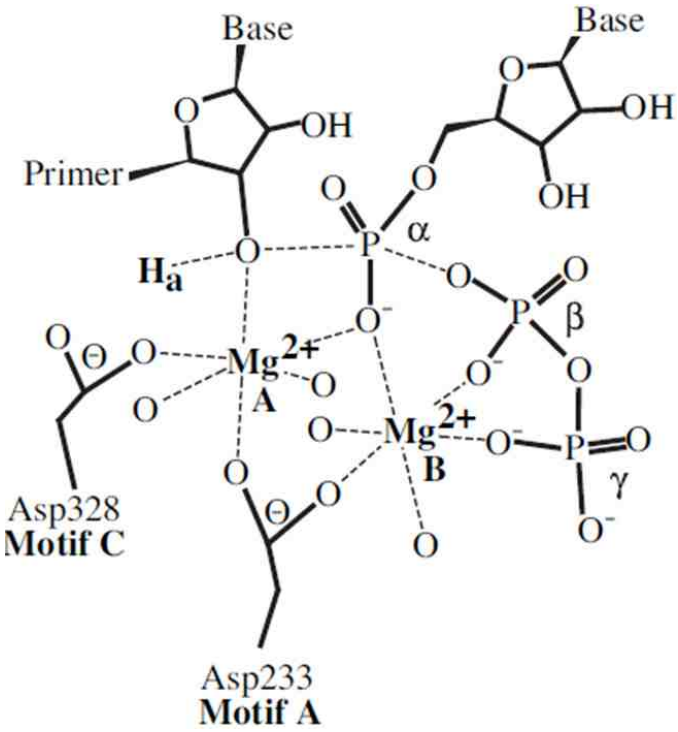

Figure 24: Polymerase active site catalyzing nucleotide addition. Magnesium A coordinates with the primer strand (dotted lines), lowering the pKa of the 3-OH (labaled Ha). Image taken from Castro et al.[151]

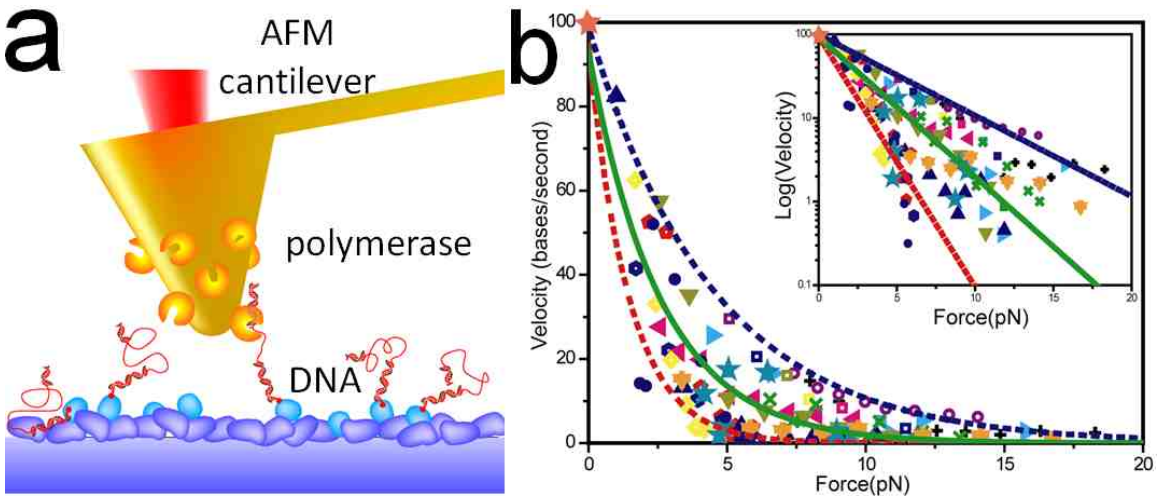

Figure 25: Measurements of the stalling force of polymerase (a) The experimental setup showing HIV RTs attached to AFM measuring tips as it is brought into contact with primer-template DNA strands attached to a surface (b) The force-velocity results for HIV RT. The different icons represent 15 different runs where full polymerization was measured. Most of the data fall within the dashed lines while the green line is an average corresponding to an overall movement of 16 Å for the polymerase. (Inset) a log plot of the graph. Images taken from Lu et al. 2004.[139]

The kinetics of polymerization have been measured using a variety of techniques including pre-steady-state stop-flow kinetics, mechanical force-velocity curves, and single-molecule studies.[76, 97, 103, 106, 115, 116, 126, 130, 139, 143, 145, 147, 150, 152-157] In the polymerization cycle, the main driving forces are PPi release, the stacking of an incoming nucleotide, and the fingers subdomain opening or closing. The rate-limiting step is the closing of the fingers subdomain, as determined by dissociation measurements[109] and pre-steady-state experiments[157]. This is further supported by measurements made to the stalling force of polymerase. In one experiment, Lu et al. 2004[139] created a force-velocity curve for the Human Immunodeficiency Virus Reverse Transcriptase (HIV RT). An Atomic Force Microscope (AFM, See Chapter 7 for more information) was used to measure the stalling force for HIV RT in solution (see Figure 25a). Several HIV-RTs were attached to the ~35 nm radius end of a cantilever tip and measurements were conducted in a buffer containing excess nucleotides. A sample surface was coated in DNA containing a 10-base primer with a 56-base DNA template attached via its 5'-end to a biotinylated bovine serum albumin coated surface. The polymerase coated tip was brought within a few nanometers of the surface and allowed to "fish" for a chance contact with DNA primer-template strands. If the polymerase and DNA primer-template contacted with the correct orientation, polymerization began. As nucleotide incorporation progressed, the tip was pulled toward the surface, gradually putting more strain on the polymerase and the DNA system as the cantilever was bent. When the force of the bent cantilever became too high, the polymerase stalled and eventually the system dissociated (either by the loss of the DNA or through a break elsewhere within the tip-sample system). As AFMs record both the speed and the amount of deflection of the cantilever,

each polymerization event allowed the construction of a force-velocity curve. The freely jointed chain model was then used to estimate the number of bases polymerized at each time to yield the curve shown in Figure 25b. This curve demonstrates a stall force of about 15 pN for HIV RT. The fast velocity decay at low force implies that the rate-limiting step of the polymerase is strongly affected by load forces, as is consistent if the load force is acting on the finger-closing motion.

Another experiment that looked at polymerization kinetics focused on the overall reaction rates of the enzyme. Ortiz et al. 2005[147] used single molecule microscopy to measure polymerization rates via fluorescently labeled nucleotides (see Figure 26). In this case, HIV RT was attached to a glass surface while free primer-template strand DNA was present in the buffer solution. The DNA contained a short primer-template segment followed by sequenced single stranded template bases (usually 10 to 40) which had an adenine base just after the double stranded region. The buffer contained all the components necessary for uninhibited polymerization (excess dNTP) to occur whenever the primer-template DNA bound to HIV RT. Also present was a low concentration of fluorescently labeled deoxyuridine triphosphate (dUTP), a nucleotide complimentary to adenine. The excitation laser was setup to only excite fluorophores near the surface. Because the HIV RT was fixed, whenever the labeled nucleotide was incorporated into the DNA it was held near the surface (and therefore in a fluorescing state) until the polymerization finished and the DNA dissociated. By observing the length of time of fluorescence, the replication time for individual short primer-templates could be determined. Through repeat measurements, a histogram was generated and fit to a model which provided estimates for the rate of single base polymerization. Repeating the

experiment at several temperatures also yielded an estimate for the Arrhenius activation energy for nucleotide incorporation.

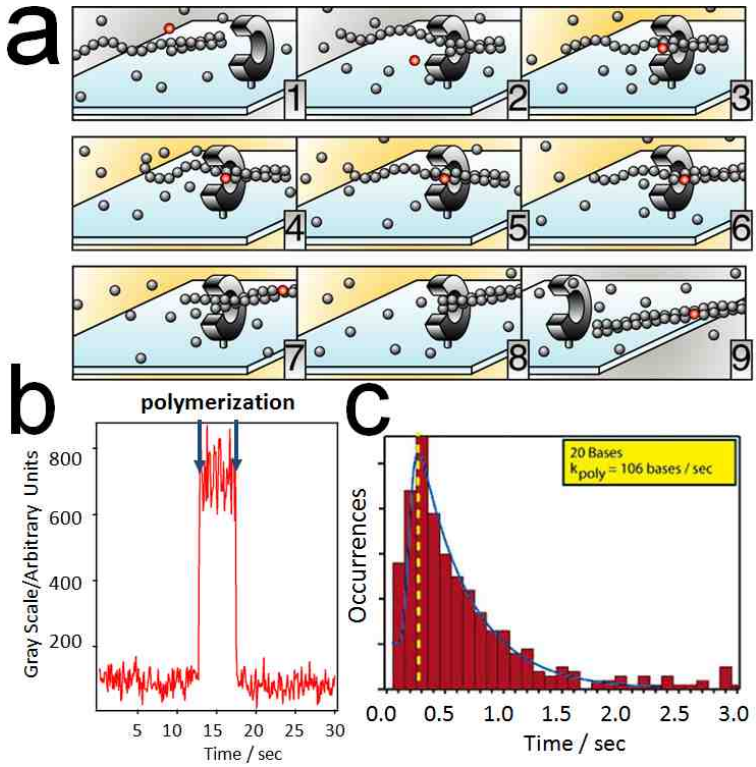

Figure 26: Measurements of polymerization rates. (a) The experimental setup showing HIV RTs bound to a glass surface (gray c-shapes) (1) Primer-template DNA strands exist in a buffer solution with dNTPs and fluorescently tagged nucleotides (dUTPs). The dUTPs fluoresce when near the surface. (2) A Primer-template strand binds to the polymerase. (3) A dUTP is incorporated into the growing DNA strand. Fluorescence begins (light background). (4-8) Polymerization progresses until a fully replicated DNA is created. (9) The DNA disasociates from the polymerase and the surface. Fluorescence ends. (b) An example fluorescent event showing increased signal during the time of polymerization. (c) Fitted histogram of many replication times for a 20 base pair DNA. Images taken from Ortiz et al. 2005.[147]

The combination of structural and kinetic information on polymerase establishes limits to the behavior of a C.G. model. One way to represent those limits is with a free energy surface.[106, 133] Each of the reasonable conformational states and transitions mentioned above has an associated statistical free energy. This can be viewed as a Helmholtz free energy that is a function of the state parameters, A(z,a,f,n;T,F). Therefore, a multi-dimensional free energy surface can be constructed from these values. To

simplify the dimensionality of this representation, it is useful to define the parameters for the nucleotide occupation state (n) and the template basepair stacking (f) as discrete variables. This creates a set of six surfaces $A_{nf}(z,\alpha)$, shown in Figure 27[106]. Each surface in the set follows the position of the polymerase on the DNA (z) along one axis and the position of the fingers subdomain (α) along the other axis. The energy values are represented by the surface contour, where wells are minimum energy stable states and higher regions are energy barriers. Transitions between states cross saddle points where the increased heights from the well bottoms correspond to activation energies. The well and barrier heights (also shown as numerical energy values in Figure 27) are derived partly from the kinetic experiments mentioned above. These surfaces therefore predict all transitions of polymerase (including times and velocity for polymerization) as a function of temperature, load force, and template length. A model polymerase seeking to be consistent with all known structural and kinetic data must correspond to a random walk across these surfaces.

As the key enzyme in the viral incorporation of HIV, RT has been a favored target for anti-AIDS drug therapy with medications such as nucleoside analog reverse transcriptase inhibitors (azidothymidine, zalcitabine, etc.), and nonnucleoside analog reverse transcriptase inhibitors, (nevirapine, efavirenz, etc.)[139, 147, 149, 158, 159] . However, the high genetic variability of HIV RT often results in the emergence of drug resistant strains. In order to further new generations of drug development, a more complete understanding of the RT cycle is required. As stated above, computational simulations provide insight into mechanisms not accessible by experimental methods. The size of the RT protein (117 kDa[137]) coupled with the DNA, free dNTP, and long polymerization

cycle times (~ 6 ms[147]) necessitates a coarse-grained (C.G.) approach if the entire system is to be simulated. The DNA model described above was developed as the first step in creating a complete C.G. model of an RT cycle.

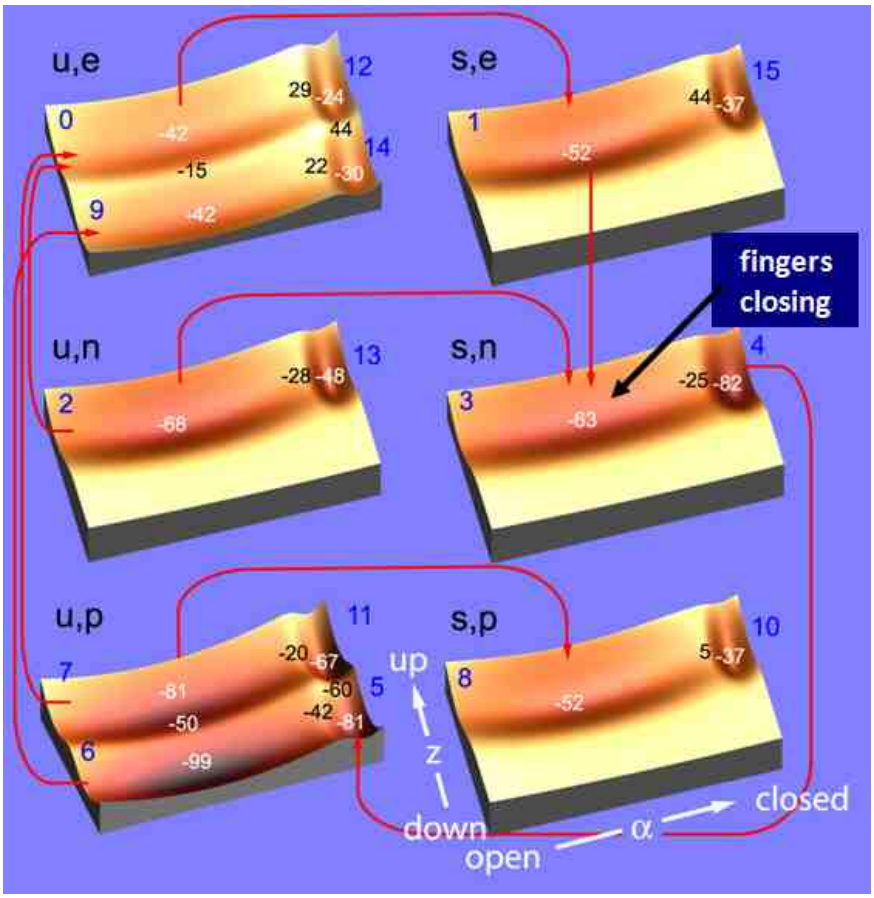

Figure 27: The potential energy surface for a model DNA polymerase. The two-dimensional surfaces are slices of a higher dimensional free energy function. Each of the six images represents four of the polymerase states in Figure 23 above where the template strand basepairs are either unstacked (u) or stacked (s) and the polymerase has a bound nucleotide (n), or a bound pyrophosphate (p) or is empty (e). On a single surface, movement along the vertical axis represents polymerase translocation (z) and movement along the horizontal axis represents movement of the fingers subdomain. The surface contour and color represent values of the potential energy function, where low, dark regions are low energy and high, bright yellow regions are high energy. The red arrows show transitions between surfaces. The blue numbers near energy minima correspond to numbered states shown in Figure 23. The numbers near the wells and saddle points are free energy values (relative to a flat-level state of 0 with units of kJ/mol) for the example model for HIV reverse transcriptase. These surfaces provide approximate activation barrier heights and free energy changes for conformational transitions of a model polymerase. This image was taken from Keller and Brozik 2005.[106]

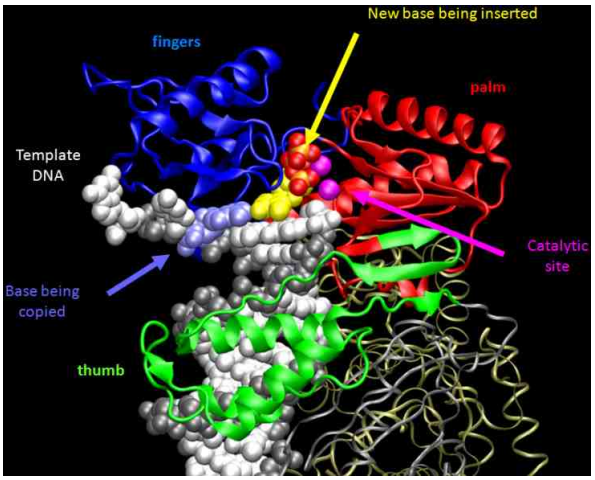

Figure 28: Crystal structure of Reverse Transcriptase. The polymerase is represented as a ribbon diagram where the fingers are colored blue, the palm is colored red, and the thumb is colored green. The DNA is represented as a spacefill diagram and is colored gray, with the exception of the blue template base being copied and the incoming base colored yellow and red.

4.2 Modeling Procedure for Proteins

Utilizing the program described above, we are currently developing a C.G. model for the HIV RT protein. To this end, we have developed a procedural approach to coarse graining proteins. Using the concept of medial axis transforms, we reduce the atoms within a protein to a small subset of shell points while still adhering as closely as possible to the original protein's shape.

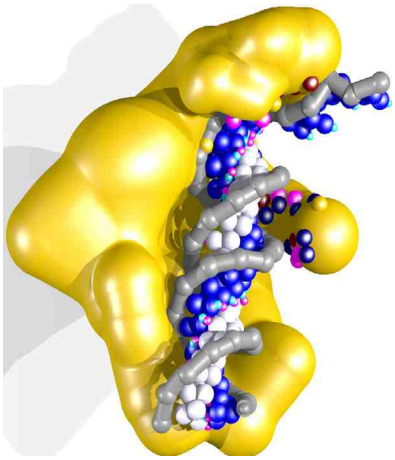

Figure 29: An example GC model of Human Immunodeficiency Virus Reverse Transcriptase complete with both shell (yellow) and bead points (pink and purple). The CG DNA has also been included.

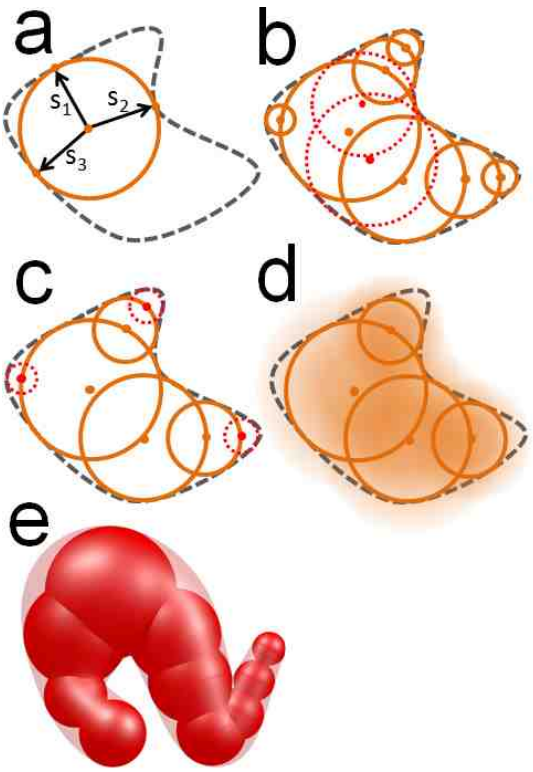

Figure 30: Medial Axis Spheres and Basis Set for a simple shape. (a) First the raw medial axis spheres are determined. A medial sphere contacts the surface in at least three locations. (b) The interior space is filled with medial spheres. Overlapping spheres (dotted red lines) are eliminated (favoring larger spheres). (c) Smaller medial axis spheres near the edges of the shape boundary are also eliminated to set the desired resolution. (d) The remaining medial sphere locations and radii provide parameters for the basis set. (e) A simple 3D example of the process in (a-d).

The medial axis transform (MAT) generates a reduced, skeleton representation of an object.[160-162] The surface of the object is reduced to a discrete line or surface called the medial axis where each point along the axis is the center of a circle (or a sphere in three dimensions). The radii of the circles are set so a union of all the circles produces a smooth surface approximation of the original object (see Figure 30). In essence, an array of many 3D surface points can be reduced to a much smaller 2D array of medial axis points and radii.

As detailed above in Chapter 2, the TM2 program utilizes a density isosurface to define the excluded volume of a shape (see Equations 14 and 15). The density is defined

as a sum of density source functions, sometimes called "blob" functions. If these blobs functions carry different weights, then Equation 15 can be rewritten as Equation 22. The linear combination of the blobs functions (ρ) is

$$\rho = \sum_{all\ blobs} A_i \left[1 - \left(\frac{|x - x_i|}{R_i}\right)^2\right]^2$$

Equation 22

where A_i is a weight per blob, R_i is the size of the blob, and $x\text{-}x_i$ is the distance from the blob center to a probe point. MAT is used to create a well-defined, reproducible basis set of blob spheres for a given protein. This converts the atoms in a pdb file (numbering in the thousands in the case of HIV RT) into a lower number of blob spheres (few hundred at most in the HIV RT case).

To convert a protein to a CG version, the full atom pdb file[163] is used by the commercially available program Chimera to generate a large number of surface points that define the protein shape. Chimera finds the solvent excluded surface (SES) by rolling a size-adjustable spherical probe over all the atoms in the protein.[164-167] With the protein surface defined, the original atom locations serve as initial blob locations for MAT. MAT then runs a search on each test point to determine the distance between the test points and the nearest surface points. If there are three or more surface points whose distance to the test point are nearly identical (with a tolerance value, usually 5%), then the test point is counted as a medial axis point (see Figure 30a).

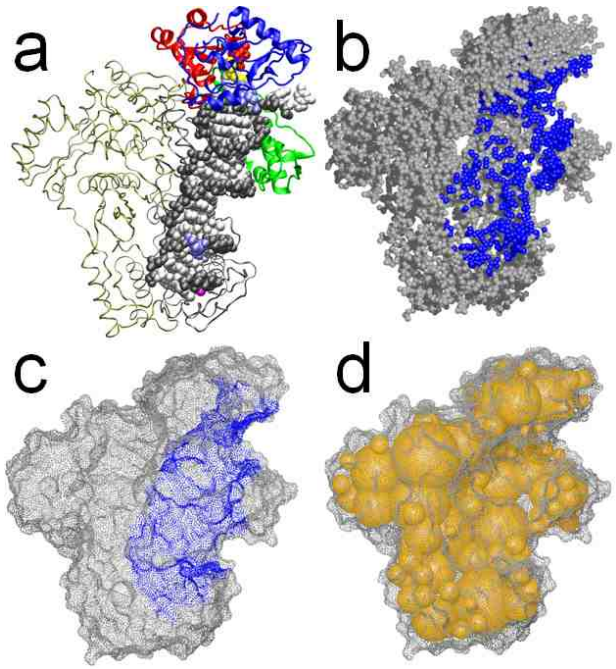

Figure 31: Medial Axis Transform for Reverse Transcriptase (HIV RT). (a) Ribbon crystal structure of RT and DNA. (b) An atom representation of HIV RT, where atoms within 8 Å of the DNA are colored blue. (c) Surface points following the solvent exclusive surface (SES) of HIV RT. These were calculated by Chimera using a 3 Å radius probe. (d) A union of some initial medial spheres of the SES of RT.

The recorded test points (along with their radii) form a set of proto-blob points. The proto-blob points are reduced by eliminating heavy overlap. Starting with any overlapping radius, proto-blobs are eliminated. After this reduction, any remaining proto-blobs smaller than a set minimum are eliminated, which sets the resolution of the final representation. At this stage, the MAT spheres form a one-to-one representation of a basis set of the blob functions that will be used to create the surface. The actual density function is determined by finding the weights A_i for each blob basis function using a linear least squares fit to the SES. This approach allows the strength of the blobs to be adjusted. It is possible to set different minimum blob sizes for different regions, allowing for a higher or lower resolution for different parts of the protein. For example, in the case of HIV RT, high resolution (smaller blobs) are preferred for the parts of the protein that

bind DNA, while lower resolution (larger blobs) can describe the non-interacting regions of the protein. Figure 31 shows an early example of a conversion of RT to a coarse grain model.

4.2 Future Work

While this technique is still in being developed, MAT replaces alternate (and problematic) "by eye" adjustment methods. Figure 32 demonstrates examples of different resolution options available within the MAT. Even at relatively low resolution (Figure 32a), the rough shape of RT is preserved while replacing roughly 8,000 atoms with 26 shell points. Of course, MAT only finds the space-filling shell component of a protein. The addition of bead points and normal mode oscillations will ultimately determine the behavior of these models.

In addition, normal model analysis of Reverse Transcriptase has been done by Adam Goler and James Brozik at the Chemistry department of Washington State University.[168] In this analysis, the normal modes of HIV RT was calculated by 1) using the simple elastic network model[22, 74, 169, 170] and by 2) using Essential Dynamics Analysis[170-181] on the atomic fluxuations of a pdb reverse transcriptase in a molecular dynamics simulation (NAMD).[31]

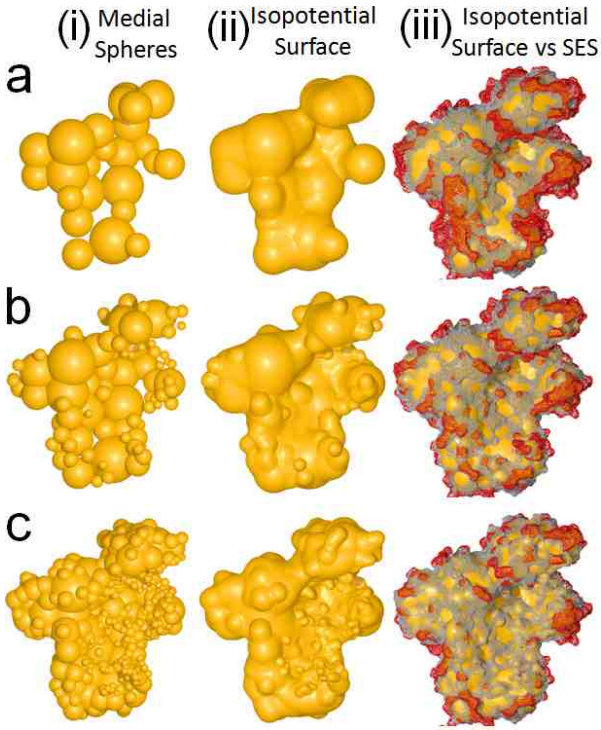

Figure 32: Variable resolution medial axis transforms of HIV RT. The first column (i) shows only the medial axis spheres. The second column (ii) shows the isopotential surface generated from the spheres in (i). The last column (iii) compares the isopotential with the SES surface points. Grey points are $\rho(x) > 0.2$ at the SES and red points are $\rho(x) < 0.2$ at the SES. (a) A representation using 26 basis functions where the minimum medial sphere radius is 6.0 Å, the maximum overlap is 1.3 times the medial sphere radius, and the minimum sphere radius near the DNA is also 6.0 Å. The RMS difference from the SES points is 0.61. (b) A representation using 95 basis functions where the minimum medial sphere radius is 3.0 Å, the maximum overlap is 1.3 times the medial sphere radius, the minimum sphere radius near the DNA is 2.0 Å. The RMS difference from the SES points is 0.61. (c) A representation using 362 basis functions where the minimum medial sphere radius is 3.0 Å, the maximum overlap is 1.0 times the medial sphere radius, the minimum sphere radius near the DNA is 1.5 Å. The RMS difference from the SES points is 0.54.

5. BACKGROUND TO MULTIFUNCTIONAL SURFACES AND THE BACTERIAL ADHESION MODEL

5.1 Introduction

In addition to coarse graining the DNA and polymerase system, a related coarse grain program is being developed to model bacterial surface attachment to patterned surfaces. Using PairWise Additive (PWA) forces, this adhesion model utilizes a combination of experimental and theoretical studies performed on nanostructured multi-component surfaces to create a theoretical model for bacterial attachment. The development of this PWA model is part of a project to determine the bioadhesion properties of multifunctional "smart" materials. These patterned, patchy, or nanostructured surfaces are composed of combinations of biocidal films, switchable polymers, and self-assembled monolayers. Containing both a light-activatable biocide and a stimli response polymer (SRP), such materials have the ability to capture and kill bacteria, and then self-clean. These surfaces are intended to serve as a prototype device to explore the combination of active materials to create multifunctional surfaces for use in detecting and destroying pathogenic bacteria. This project is part of a large, multi-university effort involving seven faculty members across three universities, including professors David Whitten, Hua Guo, John Grey, Linnea Ista, and David Keller at the University of New Mexico, Gabriel Lopez at Duke University, and Kirk Schanze at the University of Florida.

PWA Simulator has been developed from experimental results to provide a means to test theoretical models. The model focuses on results from bacterial adhesion and

surface characterization, with specific attention given to Atomic Force Microscopy imaging.

5.2 Motivation

The development of novel biocidal materials is crucial to countering the increasing prevalence of antibiotic-resistant bacteria. There is a need to develop new methods for limiting bacterial growth and transmission that do not rely on traditional antibiotics and antimicrobials. As antibiotic-resistant bacteria become more prevalent, classical mechanisms for controlling these organisms are becoming less effective. For example, according to the World Health Organization (WHO), a recently emerging threat is carbapenem and fluoroquinolone resistance in *Escherichia coli*. Fluoroquinolones are one of the most widely prescribed antibiotics and carbapenems are one of the only available treatment options for severe and resistant infections. Meanwhile, *E. coli* is one of the most frequent causes of community and hospital-acquired urinary tract, kidney, and bloodstream infections; and one of the leading causes of foodborne infections worldwide. When following treatment guidelines, antibiotic resistance of *E. coli*, *Klebsiell pneumoniae* and *Staphylococcus aureus* each exceeded 50% in many settings.[182] In 2013, resistant *E. coli* had a global mortality rate of 23.6% in infected patients, similar to the 26.3% infected patient mortality of methicillin-resistant *S. aureus* (MRSA). In the United States alone, the MRSA incidence rate reached 3.77 per 1000 patient-visits in 2010, with a mortality rate of 14.7% for those with invasive MRSA.[183] Figure 33 summarizes the main findings for selected bacteria in the WHO 2014 Antimicrobial Resistance Global Report on Surveillance. Figure 33a shows the

prevalence of resistant bacteria in hospitals and Figure 33b details how the risk of death is higher in those with resistant strains. [182]

a

Name of bacterium/ resistance	Examples of typical diseases	No. out of 194 Member States providing data	No. of WHO regions with national reports of 50% resistance or more
Escherichia coli/	Urinary tract infections, blood stream infections		
- vs 3rd gen. cephalosporins		86	5/6
- vs fluoroquinolones		92	5/6
Klebsiella pneumoniae/	Pneumonia, blood stream infections, urinary tract infections		
- vs 3rd gen. cephalosporins		87	6/6
- vs 3rd carbapenems		71	2/6
Staphylococcus aureus/	Wound infections, blood stream infections		
- vs methicillin "MRSA"		85	5/6

b

		Deaths (%)		
	Outcome (number of studies included)	**Resistant**	**Not resistant**	**RR (95% CI)**
***Escherichia coli* resistant to:**				
3rd gen. cephalosporins	Bacterium attributable mortality (n=4)	23.6	12.6	2.02 (1.41 to 2.90)
Fluoroquinolones	Bacterium attributable mortality (n=1)	0	0	
***Klebsiella pneumoniae* resistant to:**				
3rd gen. cephalosporins	Bacterium attributable mortality (n=4)	20	10.1	1.93 (1.13 to 3.31)
Carbapenems	Bacterium attributable mortality (n=1)	27	13.6	1.98 (0.61 to 6.43)
***Staphylococcus aureus* resistant to:**				

Figure 33: (a) Common bacterial strains responsible for nosocomial infections. States refer to WHO member countries grouped according to regional distribution. (b) Table of the death percentages from both resistant and non-resistant select strains where n is the number of reports and RR stands for relative risk). Images taken from The World Health Organization 2014 Global report.[182]

5.3 Phenylene ethynylenes

Phenylene ethynylene (PE)-based materials exhibit biocidal activity in aqueous solution against Gram-negative bacteria, Gram-positive bacteria, and Gram-positive bacterial spores (Bacillus anthracis, Sterne)[184, 185], viruses (T4 and MS2 Bacteriophages)[186], and vegetative yeast cells and ascospores (Saccharomyces

cerevisiae)[187]. PPE materials utilize a completely different inactivation mechanism than inhibitory drugs like quinolones. Since the first report by Lu et al.[184] in 2005, an entire library of PE materials has been developed consisting of poly(p-phenylene ethynylene) (PPE) based-polymers and controlled-length oligo-(p-phenylene ethynylene)s (OPEs). This work has been done in collaboration between the Schanze Group at the University of Florida and the Whitten Group at the University of New Mexico. Phenylene ethynylenes are a class of π–conjugated (alternating single and triple bonds with aromatic rings) polyelectrolyte (CPE) molecules with charged functionalized side chains (see Figure 34). The backbones of these polymers and oligomers confer the optical and electronic properties characteristic of π–conjugation while the presence of ionic side groups confers solubility and hydrophilicity. The polymers tend to form nano-scale aggregates in aqueous environments via intra- or interchain stacking of the hydrophobic backbone and will spontaneously coat oppositely-charged surfaces with near monolayer coverage.[184] The oligomers are generally chemically similar to the polymers, but have a small controlled number of repeat units (usually with $n < 10$)[188]. Figure 34 shows the structures of PPEs and OPEs relevant to the topics covered in this dissertation.

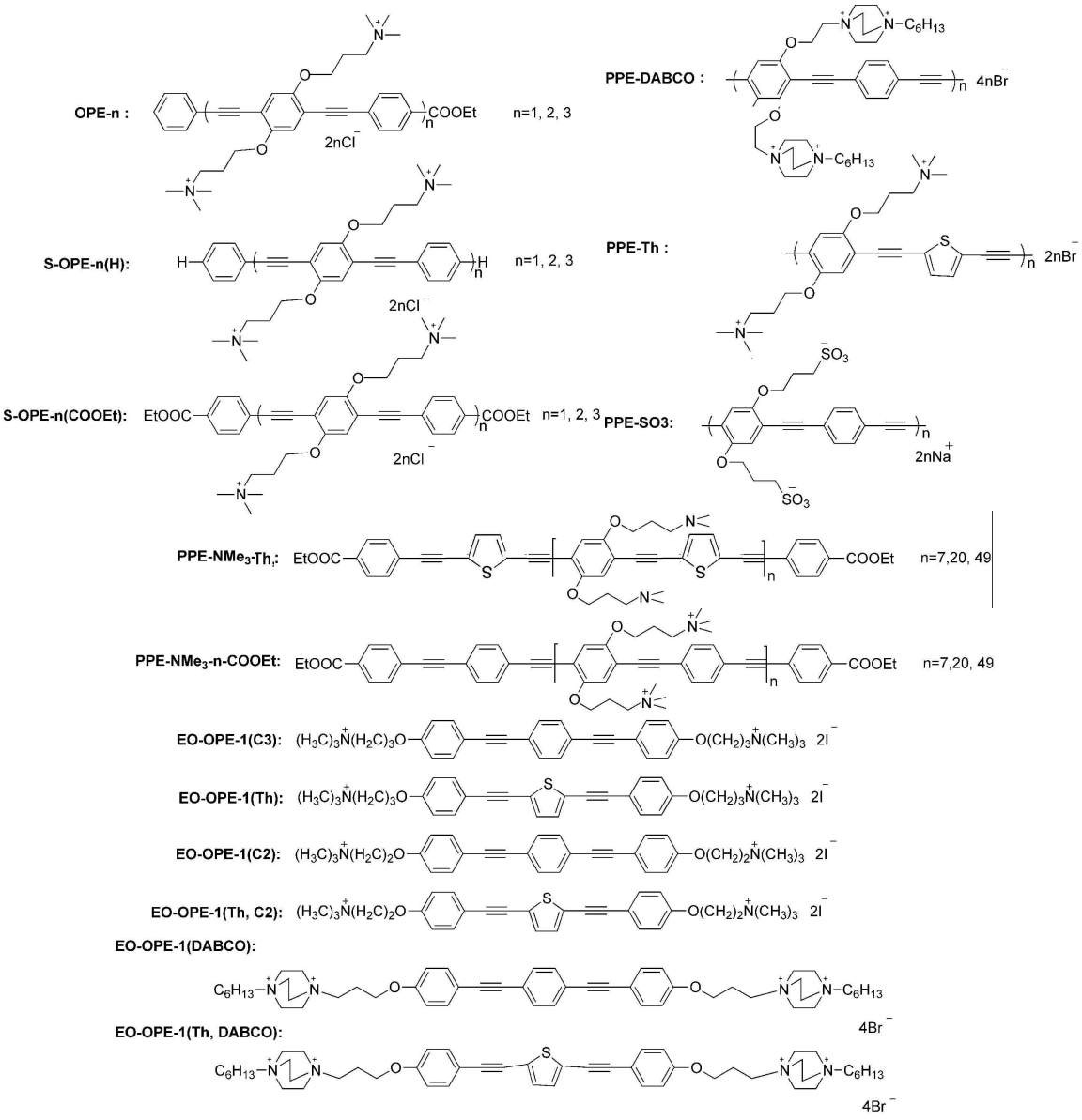

Figure 34: Structures of relevant PPEs and OPEs[189]

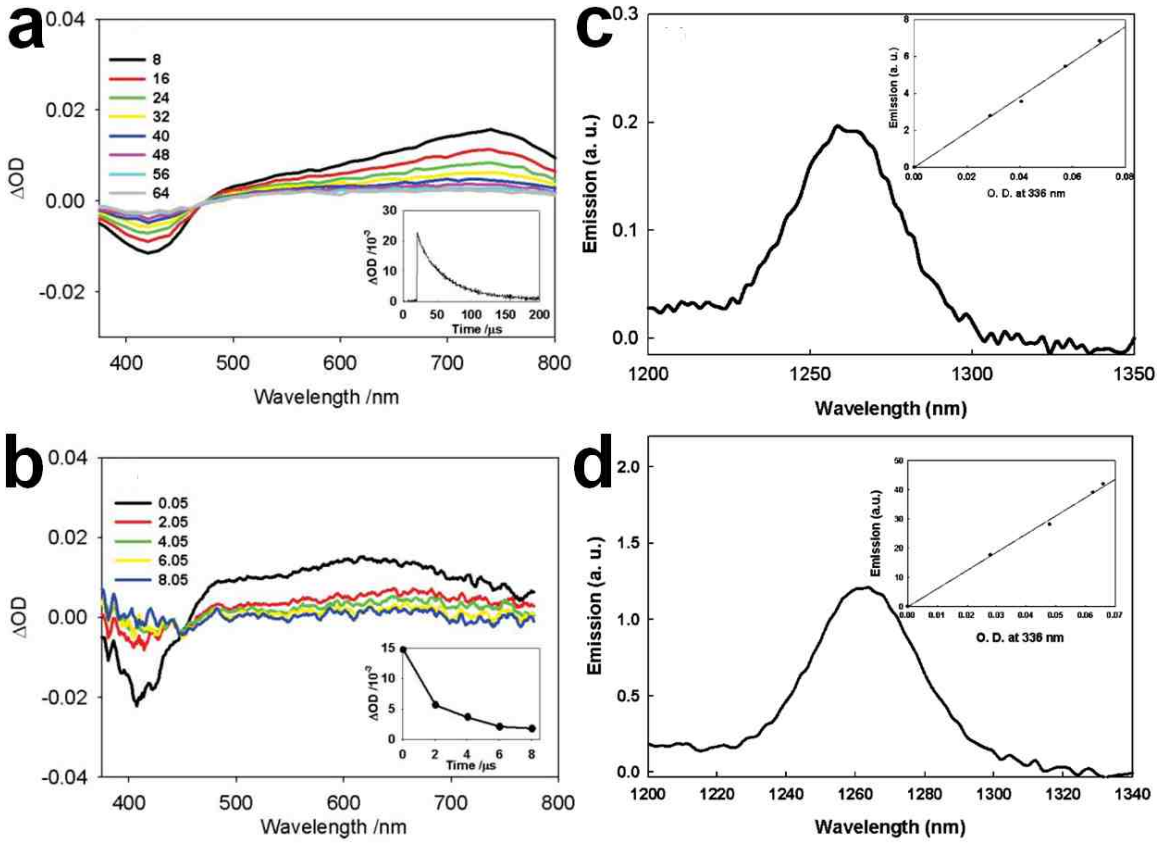

Figure 35: Transient absorption difference spectra of (a) PPE-Th in water and (b) PPE-DABCO in water (Insets: Transient absorption difference decay curves) and singlet oxygen emission sensitized by (c) PPE-Th and (d) PPE-DABCO in water in CD3OD (Inset: Integrated $^1O_2$ emission intensity versus optical density of the polymer solution). Images taken from Corbitt et al. 2009.[190]

As efficient light harvesters, CPEs and OPEs are excited by visible or UV light into a singlet excited state. Some of these excited states then undergo intersystem crossing (φisc = 0.05-0.20) to populate a relatively long-lived triplet state. Evidence of the triplet state can be found via transient absorption in the red visible region. For example, Figure 35 shows laser excitation of PPE-Th (Figure 35a) and PPE-DABCO (Figure 35b) in aqueous solution[190], where both biocides show transient absorption with a peak of around 760 nm (and ground-state bleaching at ~425 nm). The insert shows the lifetime of the absorption peaks, suggesting that the excited state has lifetimes of 40-60 μs for the polymers and 2-4 μs for the oligomers in aqueous solution.[191] The long

lifetimes provide evidence that the excited state observed is due to the triplet excited state.[192, 193]

This triplet state has enough energy (ET ≈ 2.0 -2.2 eV) to undergo transfer to surrounding solution-dissolved triplet oxygen ($^3O_2$), producing singlet oxygen ($^1O_2$).[194] Both near-infrared photoluminescence spectroscopy and Uv-vis spectroscopy of 1,3-cyclohexadiene-1,4-diethanoate (CHDDE) (a water-soluble singlet oxygen trap) in deuterated methanol confirms the presence of singlet oxygen (Figure 35c,d). For the above example polymers, PPE-DABCO has a singlet oxygen quantum yield of 0.32 and PPE-Th has a quantum yield of 0.037.[190] Singlet oxygen in turn is very reactive and can either attack cells directly or generate reactive oxygen species (ROS, usually peroxides) with biocidal properties.[191, 195-197]

5.4 Biocidal Activity

As mentioned above, PPEs and OPEs display both dark and light active biocidal activity in varying degrees against a wide variety of microorganisms. Primarily, these materials have been tested against both Gram-positive and Gram-negative bacteria. Gram-negative bacteria are more sensitive to these biocides, but most cases PPEs and OPEs exhibit more than 4 log killing in the light. These materials are also efficient at killing germinated yeast cells and display promising results against viruses and biofilms.

5.4.1 Activity against Bacteria

The differences between Gram-positive and Gram-negative bacteria are well documented.[198-208] Most Gram-positive bacteria contain a lipid membrane covered with a relatively thick (15–50 nm) heavily cross-linked peptidoglycan (PG) matrix interspersed

with teichoic acid (TA) chains and proteins (see Figure 36b). TA are polymers of glycerol phosphates or ribitol-phosphates linked via phosphodiester bonds, and are covalently anchored to the peptidoglycan (wall teichoic acids) or attached to the glycolipids in the membrane of the cell wall (lipoteichoic acids). The TA chains form a network of negative charges, which are efficient at binding cationic groups, including mono- and divalent metal cations (such as Mg2+). PG is a linear polymer of alternating β-(1,4) linked N-acetylglucosamine and N-acetylmuramic acid disaccharides, with short peptides of four or five L and D amino acids attached to N-acetylmuramic acid residues. These peptides crosslink to one another to create a net-like surface. The distribution of teichoic acid within the peptidoglycan is not well understood, but by weight there is roughly 50-70% peptidoglycan and 30-50% TA (with proteins making up very little of the weight).[200-202, 204, 205, 208-217] In contrast, Gram-negative bacteria contain an inner lipid membrane and an outer membrane with a thin (1-3 nm) intermittently cross-linked peptidoglycan layer between the membranes (see Figure 36a). The outer membrane contains phospholipids, membrane proteins, and high concentrations of negatively charged lipopolysaccharides (LPS). Most of the LPS are located on the outer face of the outer membrane, leading to a highly anionic surface. The surface is also fairly porous, especially to hydrophilic compounds, as the membrane is populated by large membrane proteins such as channel forming porins. Interior to the outer membrane is the periplasmic space, filled with a gel-like periplasm containing materials vital to the cell's health, such as binding proteins for amino acids, sugars, vitamins, and ions, as well as degrading and detoxifying enzymes. The periplasmic space is in turn supported by a thin peptidoglycan layer and an inner membrane.[198, 201, 203, 218] In general, the more structured

cell envelope of Gram-negative bacteria exhibits a stronger resistance to antimicrobial material than the cell wall of Gram-positive bacteria.[189, 195, 198]

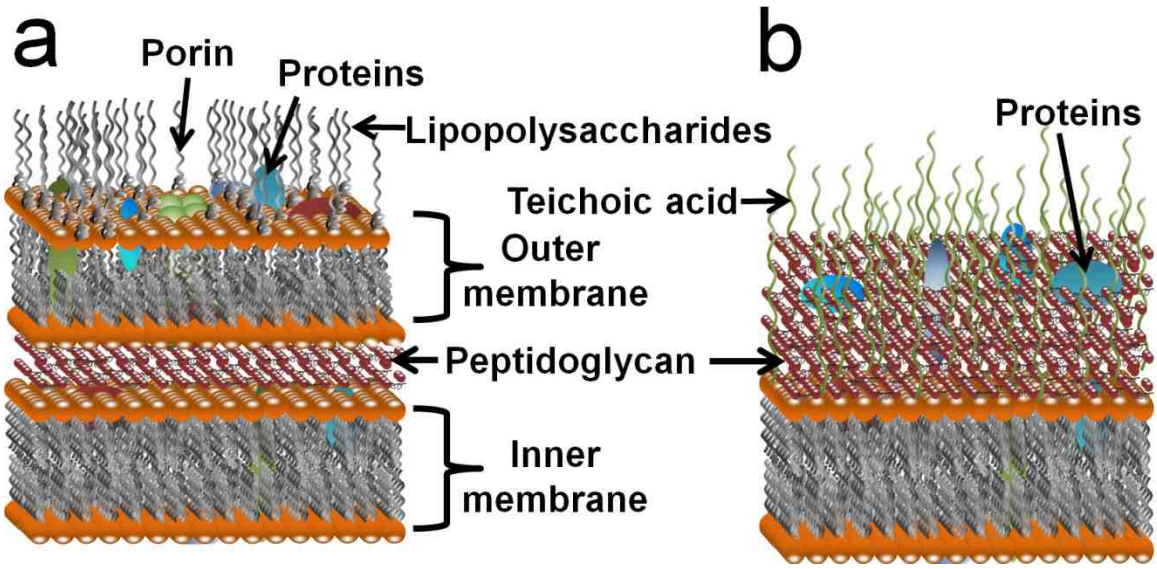

Figure 36: Diagrams of the cell wall for (a) Gram-negative and (b) Gram-positive bacteria with lipid bilayers (orange lipid heads with gray tails), lipopolysaccharides (gray), peptidoglycan (dark red), membrane proteins (blue, dark green, and dark red), and teichoic acid chains (light green).

Both Gram-positive and Gram-negative bacteria can also contain additional outer structures, with the most common being capsules and S-layers. Bacterial capsules are polymers (typically polysaccharides and/or proteins) that enclose the cell and extend radially outward from the bacterial surface (often out to a few hundred nanometers[219]). Capsules are very hydrophilic and serve primarily to bind bacteria to surfaces.[198, 199] S-layers are planar paracrystalline arrays of often weakly acidic glycoproteins that enclose and protect the cell and can make up more than 15% of the cell wall's weight. In Gram-positive bacteria, the S-layer attaches to the peptidoglycan matrix while in Gram-negative bacteria it is anchored to the LPS of the outer membrane.[220] Most of the bacteria tested against PPEs and OPEs do not contain additional outer structures.

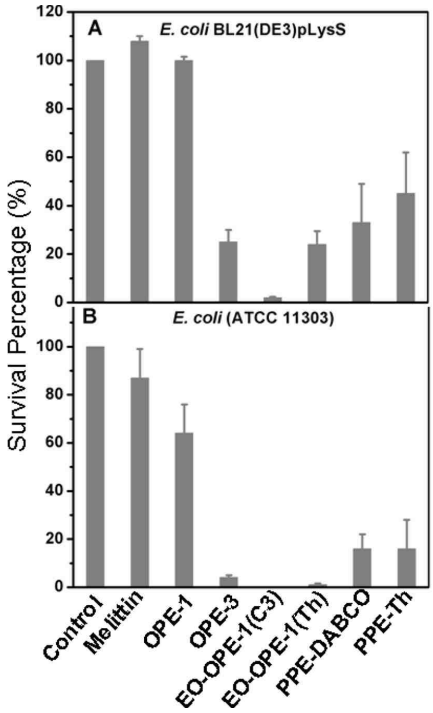

Figure 37: (a) The survival percentages of *E. coli* cells (at 10^8 cells/mL) in the dark at 37°C after 1 hr exposure to OPE-1, OPE-3, EO-OPE-1(C3), EO-OPE-1(Th), PPE-DABCO, PPE-Th, and Melittin (a well-known antimicrobial peptide). Images taken from Wang et al. 2011.[221]

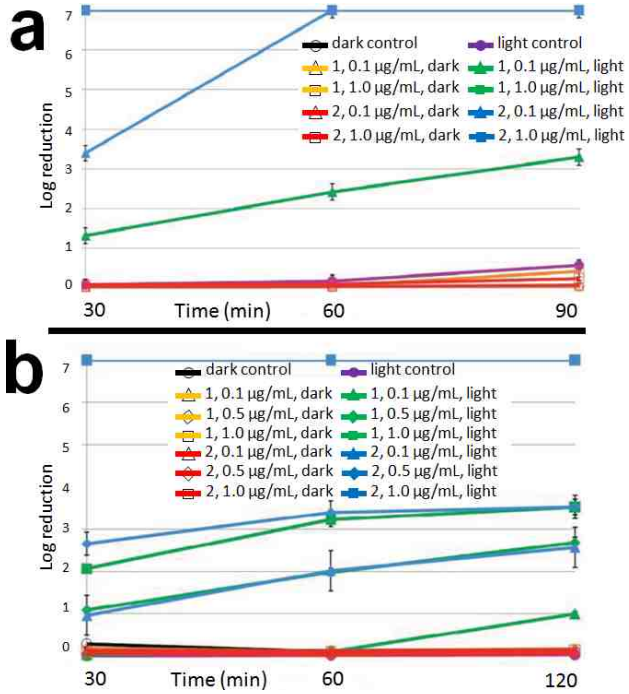

Figure 38: For comparisons between dark and light inactivation, plots of the log reduction effect of EO-OPE1-(C3) (1) and EO-OPE1-(C3,Th) (2) on (a) *S. aureus* and (b) *E. coli* at three different concentrations (0.1, 0.5, and 1.0 µg/mL) and at three times (30, 60, and 120 min). Images taken from Corbitt et al. 2011.[222]

A large library of PPE and OPE materials have been tested against Gram-negative and Gram-positive bacteria. Most polymers and oligomers show bactericidal activity in both the dark and the light, but light activation results in superior inactivation. Figure 37 shows the survival percentage for two strains of *E. coli* (Azurin and ampicillin resistance BL21(DE3)pLysS and wild-type ATCC 11303) exposed to several polymers and oligomers. 10 μg/mL of the PPEs or OPEs were added to a 37°C solution of 10^8 cells/mL of *E. coli* for one hour in the dark. Under these conditions, the OPEs (especially EO-OPE-1) exhibited a higher biocidal activity in the dark than the polymeric PPEs with a virtually complete killing of the ATCC 11303 *E. coli*. In another example, (Figure 38a), when a 10^7 cells/mL solution of *S. aureus* (ATCC 25923) was exposed to only 0.01 μg/mL of EO-OPE-1(C3), flow cytometry revealed 46% biocidal activity in the dark and nearly 4 log inactivation in the light. A similar solution of *E. coli* (ATCC 29425) was exposed for 1 hr to 1.0 μg/mL of the oligomer EO-OPE-1(C3), resulting in 50% biocidal activity in the dark and over 3 log inactivation after light exposure. (Figure 38b).[222] In most cases, both biocidal materials exhibit >99.99% biocidal efficiency toward both Gram-positive and Gram-negative bacteria.[187] In addition, Gram-positive bacteria tend to be more susceptible than their Gram-negative counterparts to light-activated biocidal killing, which is likely due to the Gram-positive's higher susceptibility to single oxygen species.

5.4.2 Activity against Endospores

Bacillus anthracis is an aerobic rod-shaped Gram-positive spore-producing soil organism, and the causative agent of anthrax. Anthrax is an acute life-threatening

infection of virulent *B. anthracis* strains (such as the Ames strain) in humans and domestic animals and is spread via inhalation or ingestion of the bacterial spores.[223] Virulent *B. anthracis* infection results in a 45% mortality rate if treated in the early phase of disease. The mortality rate increases to 92% if the illness is allowed to progress.[224]

B. anthracis is a Gram-positive bacterium with a protective outer polypeptide (poly-γ-D-glutamate) capsule, non-glycosylated S-layer proteins, and a cell wall that does not contain teichoic acid.[225] The capsule and a three-component toxin produced in the log phase of growth, both encoded on plasmids, comprise the two virulence factors of *Bacillus* cells.[226]

The *Bacillus anthracis Sterne* used below is a non-virulent strain commonly employed as a model for anthrax. It contains the toxin but lacks the polyglutamate capsule, thereby rendering it lab-appropriate.[227] *B. anthracis* produces one endospore per cell. The endospores are dormant cells and are highly resistant to temperature and moisture changes, and also to disinfectants.[226] The core of an endospore contains a compact chromosome surrounded by a thin germ cell wall. The core is then protected by an inner peptidoglycan cortex and other spore-specific layers including a final 60-100-nm thick protein layer spore coat.[228]

a

concn of PPE−NR_3^+	spore colonies	% killing
0 (control)	72 ± 8	0
1.1×10^{-3} M	75 ± 3	0
2.8×10^{-4} M	55 ± 2	23
1.1×10^{-4} M	59 ± 3	18
2.8×10^{-5} M	64 ± 4	11
1.1×10^{-5} M	48 ± 3	33
2.8×10^{-6} M	52 ± 2	28
1.1×10^{-6} M	45 ± 1	38
2.8×10^{-7} M	46 ± 4	37

b

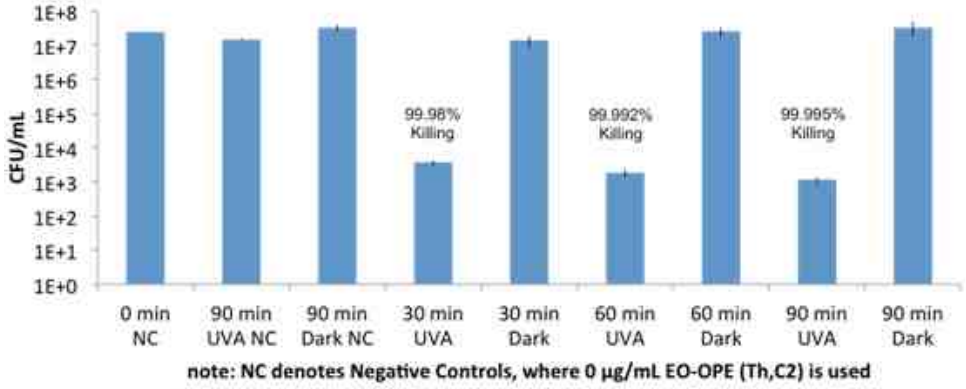

c

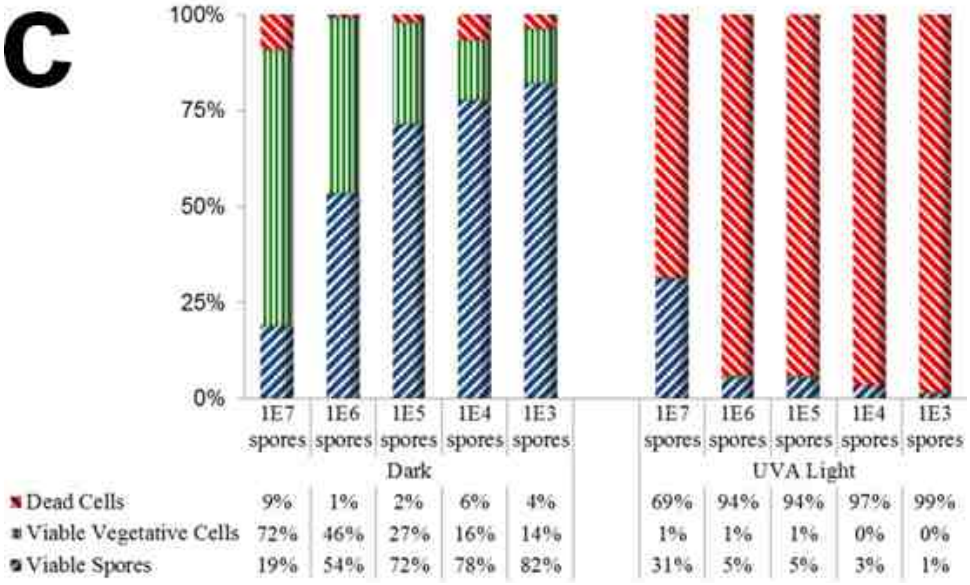

Figure 39: (a) *B. Anthracis* Spore killing percentages (as estimated by colony counting) after 2 hr exposure to PPE-$NR3^+$ (at a range of concentrations) in the light. Images taken from Lu et al. 2005.[184] (b) Number of CFU of *B. anthracis* Sterne vegetative cells following exposure to10 µg/mL EO-OPE (Th,C2). (c) Viabilities of *B. anthracis* Sterne spores at varying concentrations exposed to 10 µg/mL EO-OPE (Th,C2) for 90 minutes in the absence (left) and presence (right) of UV light. Images (b) and (c) taken from Pappas et al. 2015.[185]

When initially exposed to the PPE polymer PPE-NR_3^+ at 1 x 10-5 M, up to 40% of the viable spore count was reduced following 1.5 h of incubation in the light (see Figure 39a). Further experiments revealed that the inactivation ability of PPE-NR_3^+ was nearly independent of exposure time, but relied heavily on the concentration of the PPE. This suggests that the spore surface coating by the polymer plays a vital role in the bacterial's survival.[184] The oligomer EO-OPE (Th,C2) also inhibited *B. anthracis* Sterne spores at 10 μg/mL, causing 2 log killing in vegetative cells as measured by flow cytometry (see Figure 39b). Interestingly, in both the PPE and OPE cases, the biocidal materials may have also induced germination of the *B. anthracis* spores. This possibility was explored with EO-OPE (Th,C2), where the oligomer was found to cause rapid germination of the endospores in both the light and dark. In the dark, these germinated endospores matured into viable vegetative cells, but in the presence of near-visible light, the germinated vegetative cells were killed by the light-activated OPE. Light active EO-OPE (Th,C2) germination and killing was able to reduce the viable spore count by 99% (though this was dependent on spore concentration, with 10^3 yielding the best results, see Figure 39c).[185]

5.4.3 Activity against Yeast

S. cerevisiae is a pathogenic yeast species that serves as a common model for fungal species. *S. cerevisiae* is closely related to the pathogenic *Candida* species, which are the most commonly found clinical pathogenic fungi.[229] *S. cerevisiae* has a cell wall up to 200 nm thick, and is composed of an inner layer of mostly β1,3-glucan and chitin and an anionic outer layer of heavily glycosylated mannoproteins.[230, 231] When exposed to

environmental stress, some *S. cerevisiae* yeast cells produce ascospores, a dormant state that increases their resistance to environmental factors (including antibiotics). The ascospores are further enclosed by an ascus coat, which is derived from the cytoplasmic membrane and cell wall. Ying et al. 2013[232] exposed vegetative cells (ATCC 9763) and ascospores and the asci (ATCC 204722) of *S. cerevisiae* to a selection of PPEs and OPEs at 30 μg/ml with and without germination in the dark and under UV-irradiation for 60 min. The broad-spectrum antifungal agent Amphotericin B (AmB) was also tested to provide comparison (see Figure 40). In the dark, several of the CPEs and OPEs (specifically PPE-DABCO, EO-OPE-1(DABCO) and OPE-3) exhibited inactivation of vegetative *S. cerevisiae* cells comparable or higher than dark exposure of AmB (such as EO-OPE-1(DABCO)'s 10-fold increase). With light exposure both CPEs and OPEs showed dramatically increased cell inactivation (compared to dark exposure) with more than 6-log reductions in yeast viability. Likely, the cationic side chains of these materials favors close association with the anionic cell surfaces, providing cellular disruption. However, the tested CPEs and OPEs exhibited limited sporicidal activities. Only EO-OPE-1(Th, C2) with UV irradiation was able to exhibit significant inactivation towards ascospores. It is possible this was the only material able to penetrate the protective ascal coat.[232]

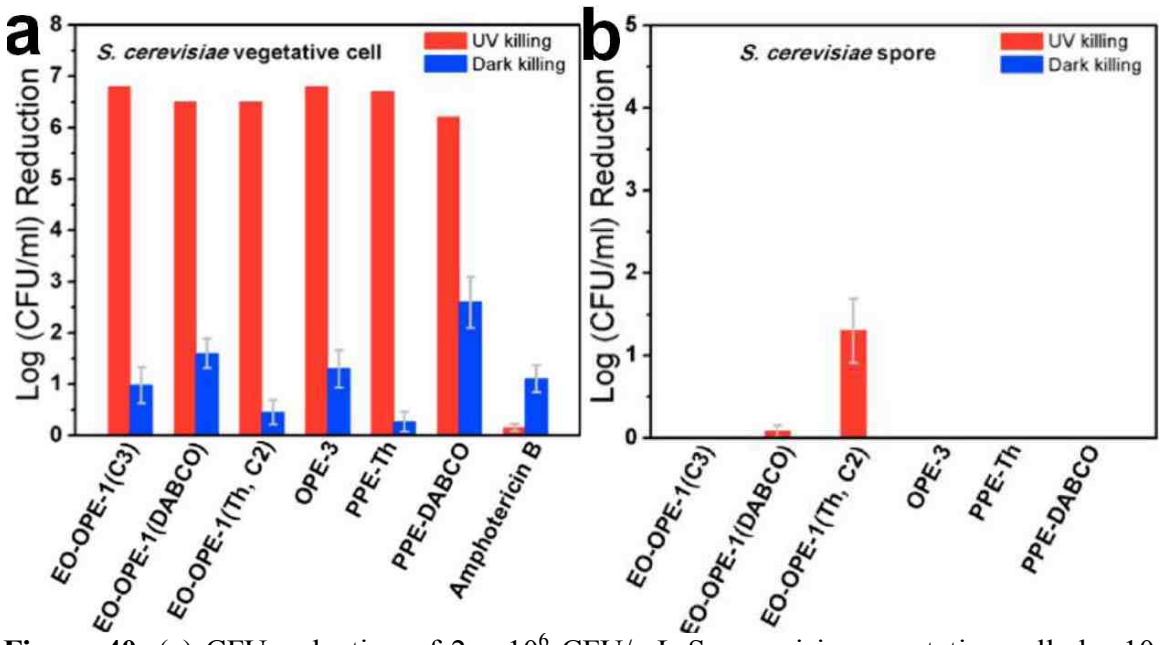

Figure 40: (a) CFU reduction of 2 x 10^6 CFU/mL S. cerevisiae vegetative cells by 10 µg/mL CPEs or OPEs in the dark (blue bars, 60 min incubation) and in the light (UV-vis, red bars, 30 min incubation). (b) CFU reduction of 2 x 10^6 CFU/mL S. cerevisiae ascospores vegetative cells by 10 µg/mL CPEs or OPEs in the dark and in the light. Images taken from Wang et al. 2013.[232]

5.4.4 Activity against other biological systems

In addition to the bacterial and fungal studies above, PPEs and OPEs have undergone initial studies with viruses, bacterial biofilms, and human endothelial and skin cells. For viruses, both materials demonstrated several orders of magnitude reduction in the number of plaque forming units (PFU) for the two model viruses, (the T4 and MS2 bacteriophages). These viruses are composed of a protein shell that encloses a nucleic acid core (a 3600 nucleotide single-stranded RNA genome for MS2 and a 170 kbp double-stranded DNA sequence for the larger T4). Neither of these commonly used model viruses contain envelopes and both are slightly anionic in neutral buffers. This negative charge facilitates association between the viruses and the CPEs and OPEs. Most of the tested CPEs and OPEs were very effective at inactivating both model viruses in

both the dark and under UV/vis activation, and showed visible damage in TEM images (Figure 41a).[186, 187]

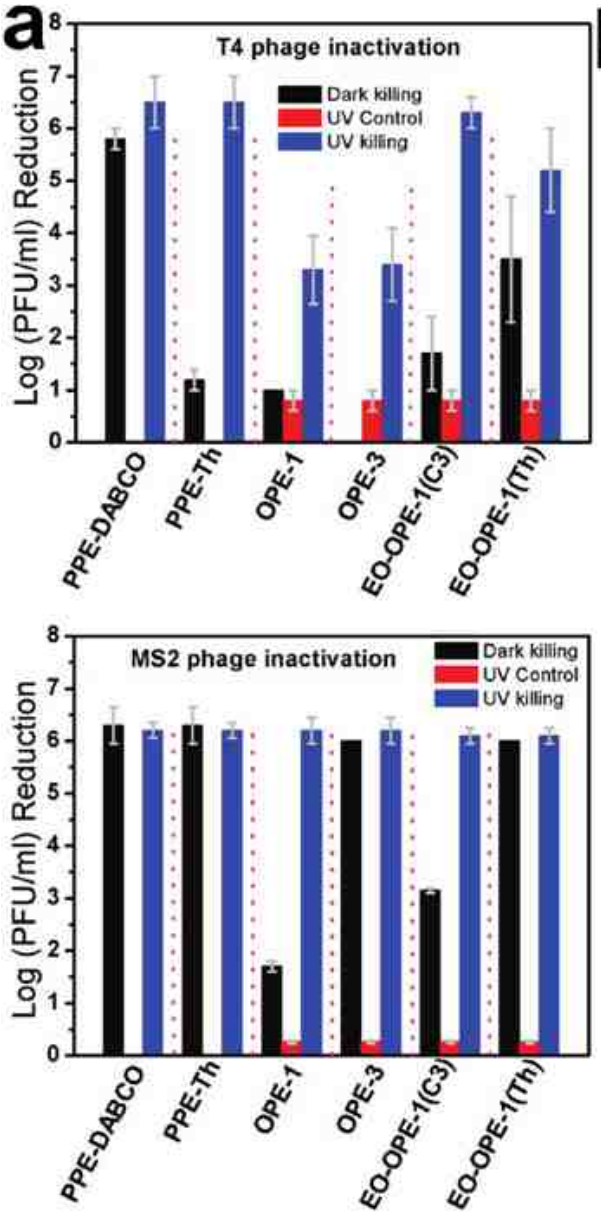

b

Endothelial Cells		LC_{70}
PPE-DABCO	dark	7
	light	27
PPE-Th	dark	13
	light	5
S-OPE-1(H)	dark	31
	light	3
S-OPE-2(H)	dark	30
	light	7
S-OPE-3(H)	dark	66
	light	19
EO-OPE-1-DABCO	dark	11
	light	8
EO-OPE-1-Th	dark	27
	light	<1
EO-OPE-1-C2	dark	29
	light	3

Epithelial Cells		LC_{70}
PPE-DABCO	dark	63
	light	68
PPE-Th	dark	<1
	light	<1
S-OPE-1(H)	dark	39
	light	2
S-OPE-2(H)	dark	36
	light	4
S-OPE-3(H)	dark	39
	light	4
EO-OPE-1-DABCO	dark	25
	light	4
EO-OPE-1-Th	dark	28
	light	<1
EO-OPE-1-C2	dark	32
	light	4

Figure 41: Biocidal activity against bacterialphages, endothelial and epithelial cells. (a) PFU reduction of 10^7 PFU/mL T4 (top) and MS2 (bottom) bacterialphages by 1hr exposure to 10 μg/mL CPEs or OPEs in the dark (black bars) or in the light (UV-vis, blue bars). Images taken from Wang et al. 2011[186] (b) Calculated LC70 concentrations (μg/mL) for endothelial and epithelial cells after 24-hour individual exposure to eight different PPE and OPE materials in dark and light conditions. Images taken from Wilde 2012.[188]

Bacterial biofilms are highly resistant surface aggregates of bacterial cells and an extracellular polymeric matrix of polysaccharides, proteins, and DNA. Biofilms are a main component of bacterial surface fouling as they protect incorporated microbes from a large range of environmental factors.[233] OPEs exposed to an *E. coli* biofilm showed better eradication than the standard antibiotic kanamycin in both the dark and after 1h of UV exposure (60-70 μg/mL minimum required concentration for the OPEs compared to kanamycin's 1000 μg/mL).[187, 234]

For human cell toxicity, several PPEs and OPS were tested on model human skin and were shown to be non-irritants at all concentrations. These materials did exhibit toxicity against mammalian epithelial and endothelial cells, especially under light exposure. Figure 41b shows an overall calculated cell toxicity (defined as LC70, the point of 30% cell viability in the tested samples).[188, 235]

5.5 PNIPAAm

In the creation of multifunctional surfaces for use in detecting and destroying pathogenic bacteria, a key material is a Stimuli Responsive Polymer (SRP) that can control organism capture and release. SRPs can dramatically change their properties (such as surface adhesion) in response to an external trigger. These polymers can be attached to surfaces either by chemical coupling or by surface polymerization. One such SRP is poly(N-isopropylacrylamide) (PNIPAAm), which switches between an extended hydrophilic state and a collapsed hydrophobic state under temperature changes. Below its lower critical solution temperature (LCST) of approximately 32°C PNIPAAm has an

expanded, hydrophilic conformation; while above its LCST, PNIPAAm collapses into a condensed hydrophobic state (see Figure 42a).

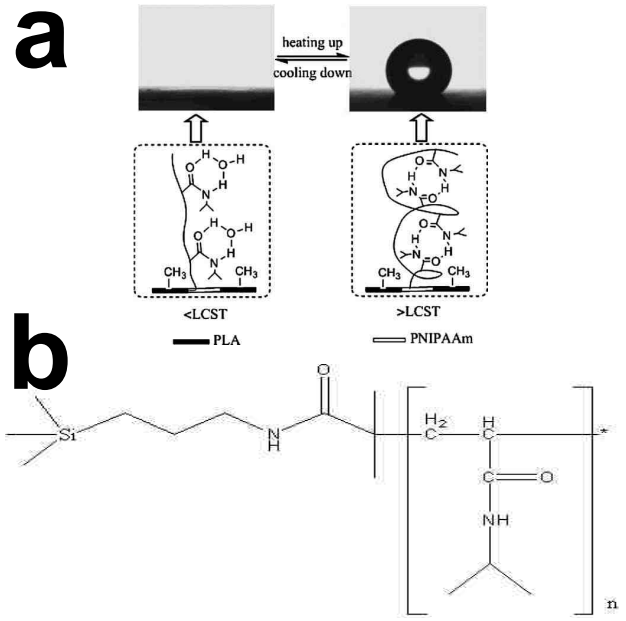

Figure 42: (a) Switchable properties of poly N-isopropylacrylamide (PNIPAAm). Below the LCST the polymer is expanded and hydrophilic, so water spreads across a PNIPAAm surface. Above the LCST the polymer collapses and water beads on the surface. (b) Chemical structure of the PNIPAAm polymer and polymerization initiator.

PNIPAAm is commonly made via a surface polymerization technique that utilizes atom transfer radical polymerization (ATRP). A glass surface is prepared by using overnight chemisorption to bind a monolayer of a polymer initiator with a silane linker to the glass ((3-trimethoxysilyl)propyl 2-bromo-2-methylpropionate). The linked surface is then placed in a solution containing 0.75 M of NIPAAm monomer along with 0.4 mM of Cu(II)Br and 0.7 mM of pentamethyldiethylenetriamine (PMDETA). The polymerization is initiated with ascorbic acid and quenched with acetone. A water and methanol rinse then removes the excess monomer from the surface. The chemical structure of the initiator and PNIPAAm polymer is shown in Figure 42b.[236, 237]

5.6 Multifunctional Surfaces

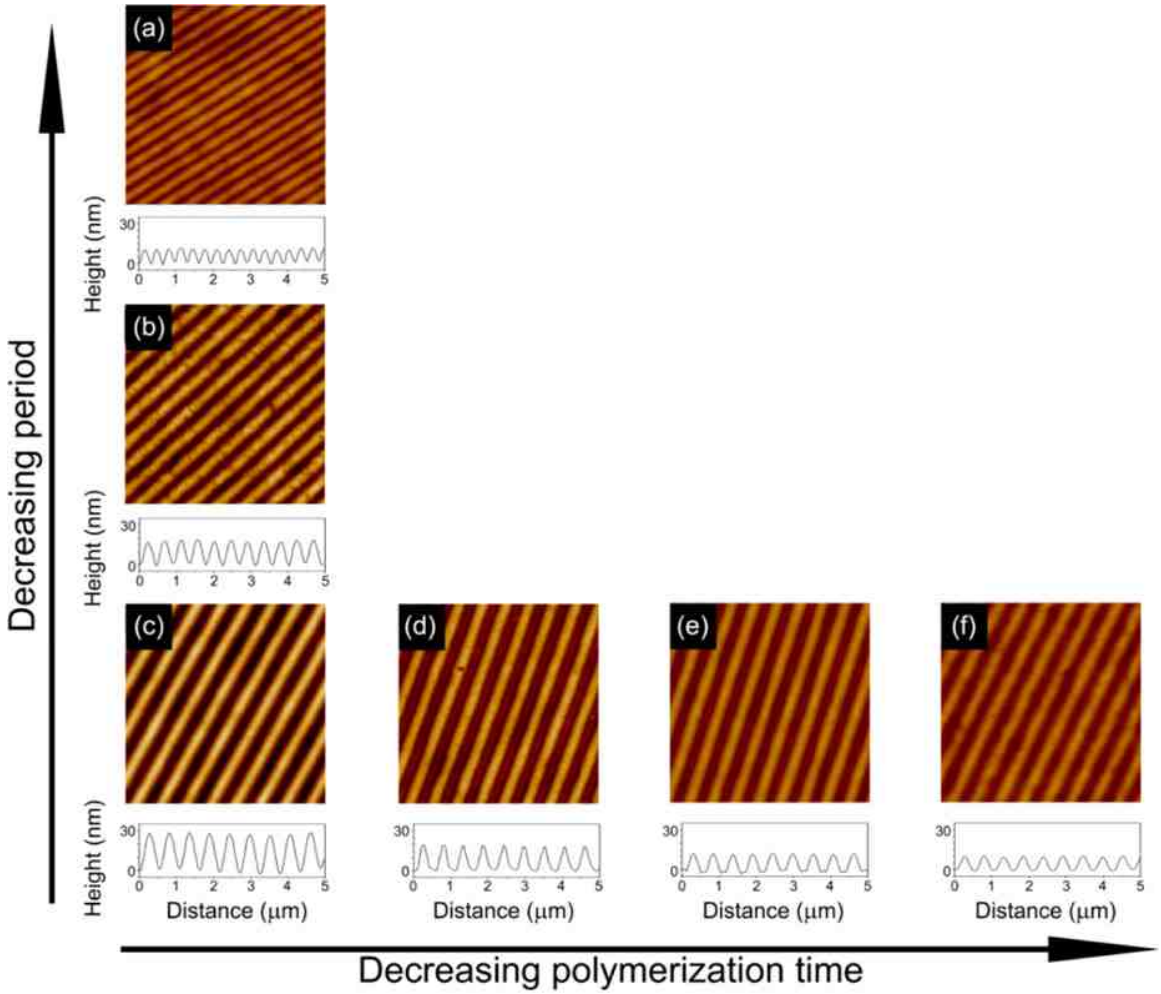

Figure 43: AFM images of nanopatterned PNIPAAm surfaces, altered (inset removed) from Yu et al. [238] 5 × 5 μm2 images were made in contact mode in air and cross sections are included below each image. Images (a), (b), and (c) have the same polymerization time of 6 minutes but vary in pattern period (330 ± 16 nm, 464 ± 17 nm, and 561 ± 19 nm respectively). Images (d), (e), and (f) have the same pattern period of 561 ± 19 nm but vary in polymerization time (4.5 min, 3 min, and 1.5 min respectively).

To create a multifunctional "smart" surface, the temperature responsive PNIPAAm polymer (controlling surface attachment) can be combined with the above PPEs (acting as a biocide). These materials can be depositied in a patterned arrangement or in a random, mixed arrangement. The López research group at Duke University has explored nanopatterned PNIPAAm and biocidal surfaces.[236, 238-241] This technique has the

benefit of being well-defined and adjustable, allowing for a study of bacterial attachment to systematically varied surfaces.

To make these nanopatterned materials, the Self-Assembled Monolayers (SAMs) terminated with atom transfer radical polymerization (ATRP) initiators were photodegraded using UV Interferometric Lithography (UV-IL). UV-IL is an adjustable, maskless technique that uses laser interference to produce regular patterns of exposure on a sample.[242] This technique allows for an adjustable and repeatable nanopatterned SAM with different pattern periods. The non-degraded regions of the SAM surfaces then initiated PNIPAAm polymerization (via ATRP) where the polymerization length could be controlled. A range of surfaces with varying pattern periods and polymer lengths were then created and characterized by X-ray photoelectron spectroscopy (XPS) and AFM images (see Figure 43). Bacterial release studies done with 1×10^8 cells/mL *E. coli* exposed the nanopatterned surfaces to bacteria at 37°C for 2 h (in buffer) before being rinsed. Since 37°C is above the LCST for PNIPAAm, the polymer collapsed and created a hydrophobic surface that promoted *E. coli* attachment. Four times more bacteria bound to the nanopatterned PNIPAAm surfaces than to the unpatterned PNIPAAm surfaces. The cells were then rinsed with 4°C water, which dropped the PNIPAAm below the LCST, causing the polymer chains to hydrate, expand and promote release. Yu et al.[238] found that approximately 80% release was achieved with the nanopatterned surfaces. This release appeared to coincide with the length of the graphed PNIPAAm polymers but was unaffected by the period of the pattern. When biocidal quaternary ammonium salt (QAS) was attached to the polymer-free regions of the nanopatterned surfaces, 73 ± 5% of the *E. coli* cells were inactivated (compared to 90 ± 2% for QAS-only surfaces).[238]

5.7 Conclusion

Phenylene ethynylene (PE)-based materials are novel biocidal materials, which have been shown to be effective against a variety of microbial organisms. The PEs exhibit increased effectiveness under light activation, likely due to increased singlet oxygen production. When exposed to Gram-positive and Gram-negative bacteria, PPEs and OPEs often cause up to 99.99% inactivation. Viruses, biofilms, and germinated spores are also susceptible to these materials. Attaching these biocides to a surface in conjunction with PNIPAAm creates a surface that can capture, kill, and release pathogens in response to the environmental factors of light and temperature. López research group has explored the creation of nanopatterned PE/PNIPAAm surfaces which can provide the experimental data needed to model bacterial attachment.

6. THEORY AND SIMULATION FOR BACTERIAL ADHESION

6.1 Introduction

In a related project to the course-grained DNA polymerase simulation, the PairWise Adhesion (PWA) model is being developed to model bacterial surface attachment. As part of a large collaboration, the PWA model is intended to help understand the attachment of bacterial cells to complex, possibly nanostructured, multi-component surfaces. We aim to create a predictive model for bacterial attachment to surfaces relevant to the overall biocidal materials project discussed in Chapter 5. In addition we look to answer questions like: "Is it possible to reduce the complexity of a bacterial-to-substrate interaction enough to create a model that reproduces observed attachment rates?" and "Can that model then be used to predict bacterial attachment to various surfaces?"

The initial attachment of a bacterium to a surface, before the cell begins to express attachment structures (such as pili and adhesin proteins), is driven by the thermodynamics of the cell-to-surface interaction region. Physical adhesion is mostly caused by short-ranged (relative to the size of a bacterium) interactions in this region, which depend on the complex composition and spatial structure of both the cell and the surface. The PWA model approaches bacterial attachment as a thermodynamic state driven by the combination of the free energy of interaction between the various materials present on both the cell and the target surface. The model reduces the free energy of bacterial attachment to a (large) sum of simple contributions between sites on the bacterial and target surfaces.

What is required of the model is: (a) knowledge of the types of materials on both surfaces that contribute to attachment, (b) the spatial distribution of those materials on relevant surfaces, and (c) an estimate of the free energies of interaction between pairs of sites on the surfaces. To determine attachment, all contributions to the total surface free energy (or surface tension) are calculated. The surface tension from each pure chemical component interacting with another pure chemical component on the opposite surface are added in a pairwise manner over all sites. These surface tension values ideally would be found experimentally, but in most cases only reasonable estimates are available. This is also true for the surface organization. However in the cases reported below the target surface is generally well-characterized while the bacterial surface structure can be estimated via imaging or statistical distributions.

6.2 PWA Simulator and PWA Integrator

The PWA Simulator program is a variant of the TM2 program discussed in Chapter 2 and allows the dynamic process of initial attachment of bacteria to surfaces. It utilizes the same Brownian motion mechanics covered in Section 2.3. In this system, an entire bacterium is a single unit, as is a planar target surface. However, the PWA Simulator program requires some customization to deal with the complex interactions between the model bacteria and the surfaces. This is handled by special units called a "cell" and a "surface" which are unique to PWA Simulator and far more complex than the basic units of TM2.

While PWA Simulator can be used to explore the dynamics of adhesion, a second program called PWA Integrator uses explicit integration of a partition function to determine the equilibrium potential of mean force (pmf) between a bacterium and a target

surface as a function of distance from the cell to target surfaces. From the pmf, bulk properties like equilibrium constants and surface coverage can be determined. PWA Integrator therefore facilities direct comparison between the basic theory and measureable experimental quantities.

6.3 Cell-to-Surface Free Energy Functional

As a cell and a planar target move toward each other, different materials on their surfaces come into contact. Both PWA Simulator and PWA Integrator use a surface free energy functional to estimate the total free energy between two objects. The free energies associated with these contacts dictates whether or not adhesion takes place. The total cell-to-surface adhesion free energy (ΔG) is taken to be a sum of the cell-to-surface contact energy ($\Delta G_{cell\text{-}target}$) plus cellular deformation energy (ΔG_{deform}).

$$\Delta G = \Delta G_{cell-target} + \Delta G_{deform}$$

Equation 23

To determine $\Delta G_{cell\text{-}target}$, let the target's exposed surface be an (infinite) xy plane, and let the cell have an ideal lozenge shape. Let each of these surfaces have a statistical arrangement of different materials defined by a set of fractional area functions, $\boldsymbol{\alpha}(x,y)$. Consider a small area patch dA on one of the surfaces. We can think of the patch as containing a mosaic of different pure materials arranged together (such as Teichoic acids or PNIPAAm). Instead of keeping track of the location of each material, the PWA model assigns only the fraction of the total area occupied by each material (see Figure 44 and Figure 45). Doing this for every material within a given patch at position (x,y) yields an array of area fractions $\boldsymbol{a}(x,y) = (\alpha_1(x,y),\ \alpha_2(x,y), \ldots, \alpha_i(x,y))$ that must sum

to unity. The size of the area patch defines the resolution at which the surface is treated. This essentially coarse-grains the surface, so that it is not necessary to keep track of very small, high-resolution features (like individual proteins). $\Delta G_{cell\text{-}target}$ is then approximated as the sum of interactions between the pure materials weighted by their prevalence on the surface (their area fractions).

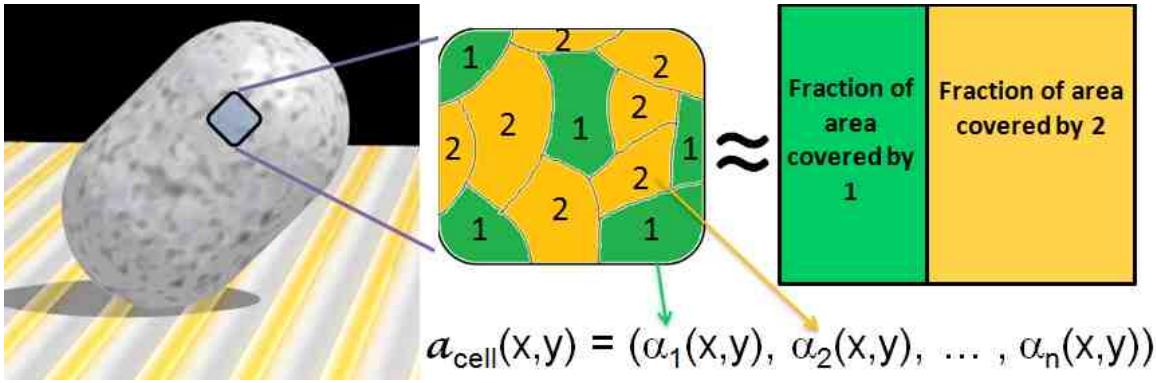

Figure 44: An example of an area patch on the cell containing two "pure" materials, 1 and 2. Within the patch, the coverage of each material is summed into an area fraction

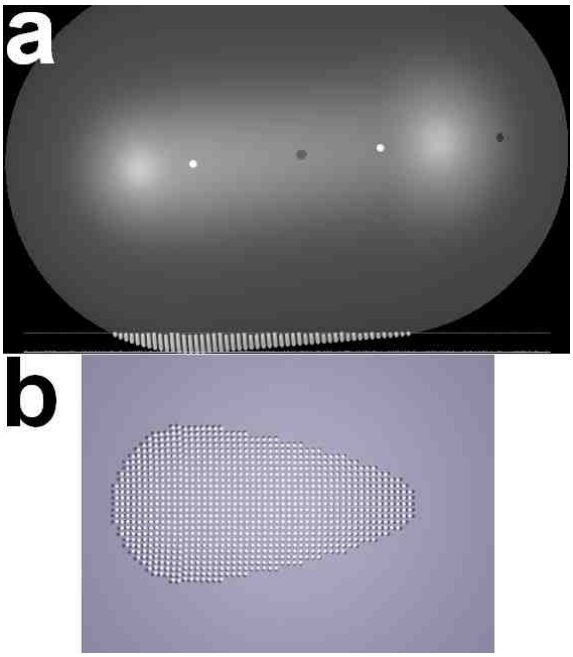

Figure 45: Example of an interacting footprint composed of many area patches. (a) A side-view of a model cell (large gray lozenge) as one side touches a model pane near the bottom of the image. Area patches that are close enough to contribute to the cell-target interaction energy are highlighted on the cell. (b) A top view of the interacting footprint on the target plane. Each dot in this image represents an area patch.

To find $\Delta G_{\text{cell-target}}$, first consider a cell at a fixed orientation (Ω) with respect to the target surface and let Δz be the distance between the target and the closest point on the cell (see Figure 46). A reasonable approximation for $\Delta G(\Omega, \mathbf{x}, \Delta z)_{\text{cell-target}}$ is then:

$$\Delta G(\Omega, \mathbf{x}, \Delta z)_{cell-target} = \iint dA_{target} \iint dA'_{cell} \sum_k \sum_l \sum_i \boldsymbol{a}^k_{cell}(\boldsymbol{x}_{cell}) \boldsymbol{a}^l_{target}(\boldsymbol{x}_{target} + \boldsymbol{x}) \Delta\boldsymbol{\gamma}_{k,l} f_i^{k,l} e^{-\kappa_i^{k,l} z(\Omega, \boldsymbol{x}_{target})} \delta^2(\boldsymbol{x}_{cell} - \boldsymbol{x}_{target})$$

Equation 24

$\boldsymbol{a}^k_{cell}(\boldsymbol{x}_{cell})$ and $\boldsymbol{a}^l_{target}(\boldsymbol{x}_{target} + \boldsymbol{x})$ are the area fractions mentioned above; in this case these arrays are indexed by the type of materials (k and l). $\Delta\boldsymbol{\gamma}_{k,l}$ is the surface tension between the "pure" materials of the area fractions. Here $\Delta\boldsymbol{\gamma}_{k,l} = \gamma_{kl} - \gamma_{k,solv} - \gamma_{l,solv}$, where $\Delta\boldsymbol{\gamma}_{k,l}$ is the surface tension between a pair of pure materials, k and l, minus the surface tensions of each material, $\Delta\gamma_{k,solv}$ and $\Delta\gamma_{l,solv}$, with respect to the solvent. The difference accounts for the exclusion of solvent upon contact between the two surfaces. The z-dependent exponential series $\sum_i f_i^{k,l} e^{-\kappa_i^{k,l} z(\Omega, \boldsymbol{x}_{target})}$ is a representation of the pmf between two surface patches separated along the z-direction by $z(\Omega, \mathbf{x}_{\text{target}})$. It allows for the fact that not all points need to be in contact with each other. This includes effects such as counterion-shielded charge-charge interaction, and the effects of polymeric cushions. The exponential ensures that the effective $\Delta\boldsymbol{\gamma}_{k,l}$ goes to zero when the two surfaces are sufficiently far apart. The delta function represents a further approximation that limits interaction between a given patch on the target plane and the corresponding patch vertically above it on the cell. This greatly reduces the number of required calculations and amounts to assuming that long-distance interactions do not greatly contribute to the total free energy. Also, to account approximately for the fact that the cell surface is not

always parallel to the target, the cell area element that appears in the above equation, $dA'_{cell,}$ is the projected area of the curved cell patch onto the target surface. Converting to the proper cell area, dA_{cell}, requires a foreshortening adjustment term. This factor is cos(θ), where θ is the angle between the normal of the cell area patch and the z-axis of the cell-target frame (see Figure 46)

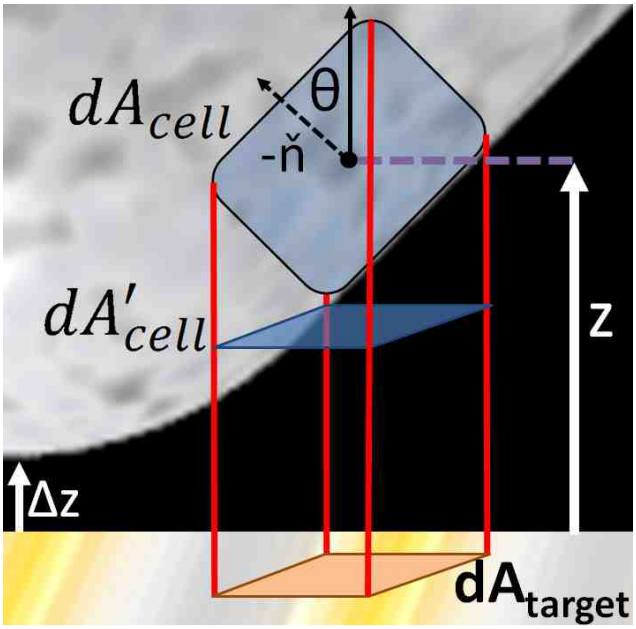

Figure 46: Converting an area fraction on a cell to a projected area fraction.
$dA'_{cell} = \cos\theta * dA_{cell}$, where θ is the angle between the area patch normal and the z-axis. (Here the negative normal is shown for image clarity.)

With the addition of the foreshortening factor, simplifying the above equation yields:

$$\Delta G(\Omega, \mathbf{x}, \Delta z)_{cell-target} = \sum_k \sum_l \sum_i \Delta G_{0_i}^{k,l}(\Omega, \mathbf{x})\, e^{-\kappa_i^{k,l} \Delta z}$$

Equation 25

where

$$\Delta G_{0_i}^{k,l}(\Omega, \mathbf{x}) =$$

$$\iint dA_{target} \left[cos\theta\ \boldsymbol{a}_{cell}^{k}(\boldsymbol{x}_{cell})\, \boldsymbol{a}_{target}^{l}(\boldsymbol{x}_{target} + \boldsymbol{x})\, \Delta\boldsymbol{\gamma}_{k,l}\, f_i^{k,l} e^{-\kappa_i^{k,l} h_0(\Omega, \boldsymbol{x}_{target})} \right]$$

Equation 26

Here $h_0(\Omega, \mathbf{x}_{target})$ is the height of a particular cell area patch above the cell's lowest point (Δz). At a fixed Ω and Δz, $h_0(\Omega, \mathbf{x}_{target})$ varies for every patch on the cell. The quantity $\Delta G_{0_i}^{k,l}(\Omega, \mathbf{x})$ is independent of the cell-to-target distance and therefore all of the dependence of $\Delta G(\Omega, \mathbf{x}, \Delta z)$ on Δz is contained in the exponential factors $e^{-\kappa_i^{k,l}\Delta z}$. Once $\Delta G_{0_i}^{k,l}(\Omega, \mathbf{x})$ is found for the cell-to-target interaction at the cell's closest approach ($\Delta z = 0$), it is possible to calculate $\Delta G(\Omega, \mathbf{x}, \Delta z)_{cell\text{-}target}$ at any Δz value quickly.

6.4 Initial simulations

Initial test simulations were carried out in PWA Simulator using simple models of the bacterial and target surfaces. The simulations were carried out as in TM2, using Brownian dynamics with interaction forces between the cell and target calculated from the gradients of the free energy functional with respect to orientation and the center of mass. The goals of these early trials was to investigate the behavior of cells and (1) their initial contact with the surface, (2) full attachment to a strongly adhesive target and (2) reversible attachment to a weakly adhesive target. A bacterium was taken to be an ideal lozenge shape with a length of 800 nm and a diameter of 500 nm and both the cell and target surfaces were composed of two randomly distributed materials. As the units involved are much larger than the DNA residues from Chapter 3, the timestep was increased to 1 μs per step. Figure 47 shows the multistep process for a single bacterium binding to a strongly adhesive target surface in PWA Simulator. In this case, one of the materials on the target surface was neutral (does not contribute to the interactions) while the other was either attractive or repulsive toward the bacterium. In the very first stage of

cell attachment, the bacterium attached via a single pole. This was followed by an irreversible attachment of the cell as it contacted the surface along the bacterium's major axis. This surface binding pattern is consistent with the observed behavior of rod-shaped bacteria,[243, 244] demonstrating that PWA Simulator can reproduce at least some observed behavior with relatively simple models for the bacterium and target. Cell attachment is a diffusion-driven multistage process where the geometry of the bacterium (with a relatively large surface area of contact) can create irreversible binding from even a small surface free energy difference between the solvent exposed surface and the directly contacting cell and target.

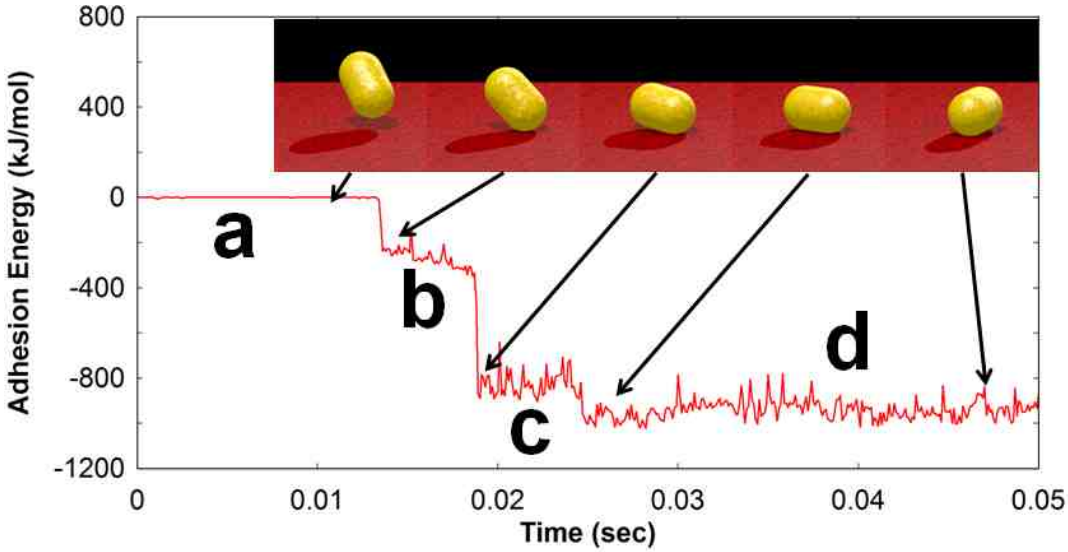

Figure 47: A graph of the adhesion free energy for a single bacterium binding to a strongly adhesive target surface in PWA Simulator. The surface tension difference between the cell and the attractive surface material is -0.01 dyne/cm. (a) Initial stages of bulk diffusion with no interaction between the bacterium and the target surface. (b) The tip of the bacterium contacts the target. (c) The bacterium lays down on the target, increasing contact. (d) The bacterium settles on the surface and starts diffusion across the surface. (Inset) A series of images from PWA Simulator highlighting the different stages of binding (arrows) for the bacterium (yellow) to the target (red).

PWA Simulator also allows for dynamic switching of the target surface's properties, mimicking behaviors of environmentally responsive materials like

PNIPAAm.[236, 238, 239, 241, 245-248] Figure 48 shows the response of a model bacterium to a binding switchable target surface. Initial attachment to an adhesive surface again follows the multistep binding process; however, when the target is switched to a non-adhesive surface the cell quickly disassociates.

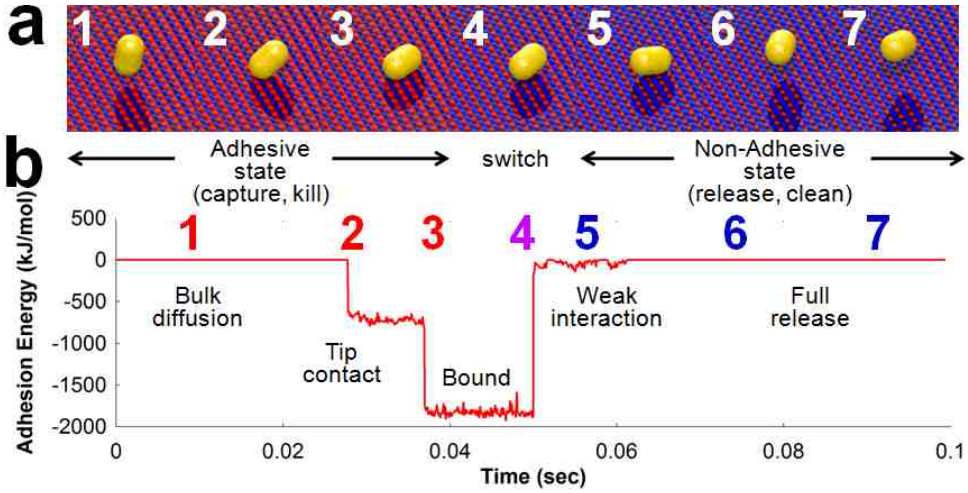

Figure 48: A graph of the adhesion free energy for a single bacterium binding to a binding to a switchable surface in PWA Simulator. The surface tension between the cell and the attractive surface material is -0.01 dyne/cm until it is switched to zero. (a) Images of the bacterium (yellow) binding and releasing from the target surface as it switches from adhesive (red) to non-adhesive (blue). (b) A graph of the total adhesion free energy for a single bacterium binding to a switchable target surface in PWA Simulator. (1) Initial stages of bulk diffusion with an adhesive surface. (2-3) The bacterium contacting the surface in a similar process as shown in Figure 47 above. (4-5) The target switches to a non-adhesive surface that only interacts weakly with the bacterium. (6-7) The bacterium diffuses away.

Simulations have also been done with multiple bacteria interacting with a target surface (Figure 49). With a weakly adhesive target (Figure 49a,b), transient binding occurs where several bacteria associate with the target, but then dissociate relatively quickly as a result of Brownian diffusion.[243, 244] With a strongly adhesive target (Figure 49c,d), successive bacteria bind irreversibly, lowering the overall adhesion energy.

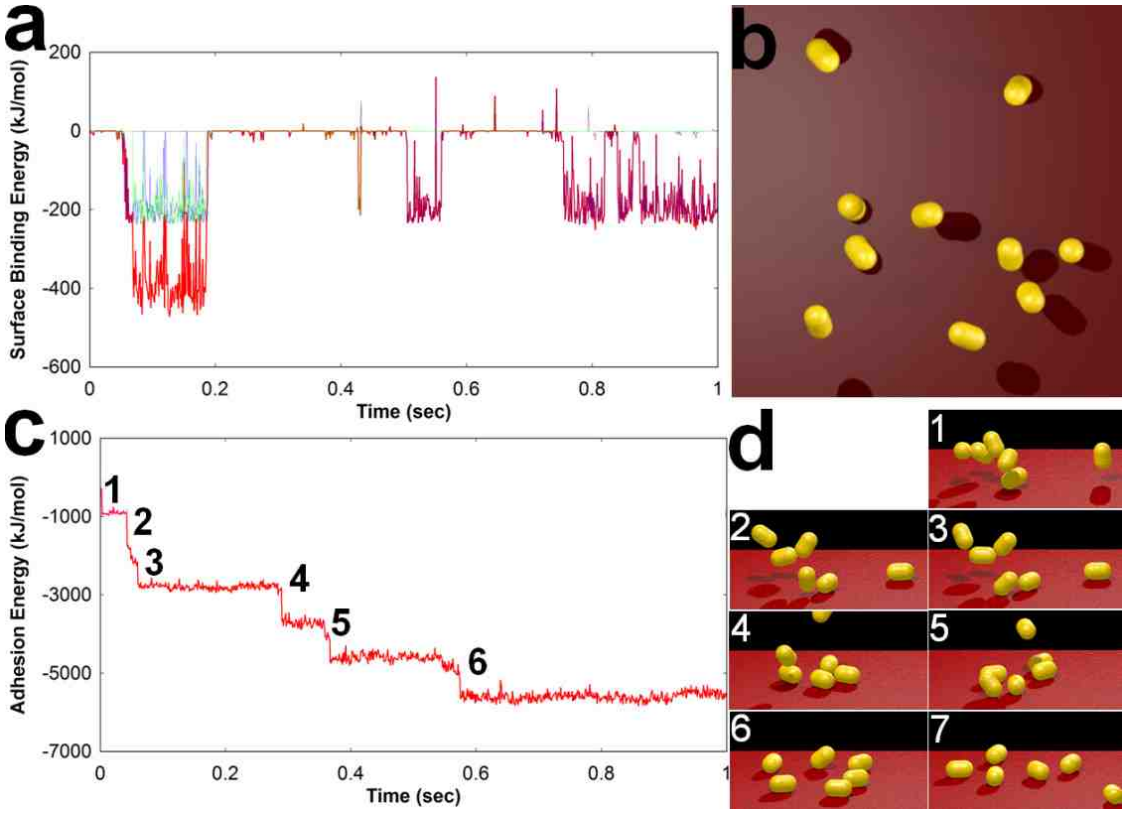

Figure 49: Multiple bacteria binding to a target surface in PWA Simulator. (a) A graph of the adhesion free energy for ten bacteria interacting with a weakly adhesive target surface (surface tension is -0.001 dyne/cm). The free energy for each bacterium is represented by various colors while the total is shown in red. (b) An image showing a top-down view of the bacteria (yellow) near the target surface (red). (c) A graph of the total adhesion free energy for six bacteria interacting with a strongly adhesive target surface (surface tension is -0.03 dyne/cm). Each number corresponds to the irreversible binding of an additional bacterium. (d) Images showing successive binding events, numbered to match the events in (c)

6.5 Potential of Mean Force for Cell-to-Target Height

PWA Integrator calculates the full potential of mean force as a function of cell-to-target distance. This is done by integrating the free energy of adhesion for all cell-patch-to-target-patch pairs over all possible orientations of the cell at a fixed height z_{cell}, the height of the cell centroid above the target surface (see Figure 50). The resulting pmf can then be used to find experimentally measurable properties like the equilibrium constant and the cell surface coverage.

The pmf for a given cell-target distance z_{cell}, $W(z_{cell})$, is defined as:

$$W(z_{cell}) = -k_B T \ln\left[\frac{1}{8\pi^2}\int_0^{2\pi}\int_0^{2\pi}\int_0^{\pi} \sin\theta \, d\theta d\phi d\chi \, e^{-\beta\left(\Delta G(\Omega)_{\text{cell}\,-\text{target}} + \Delta G_{\text{deform}}\right)}\right]$$

Equation 27

where θ,ϕ, χ are the three cell orientation angles, defined in Figure 50 below, and constitute the actual coordinates implied by Ω. The deformation energy, ΔG_{deform}, is characterized by elasticity theory[249-255] and is approximated as the energy required to deform a spherical shell as it contacts a hard surface.

$$\Delta G_{\text{deform}} = \left(c_0\sqrt{\Delta z} + c_1 \Delta z^2\right)\frac{\Delta z}{R}$$

Equation 28

where Δz is the cell-to-target distance defined above, R is the radius of sphere (500 nm), and of c0 and c1 are elastic constants (9.5 x 10^{-15} J/$m^{1/2}$ and 0.1 J/m^2 respectively).

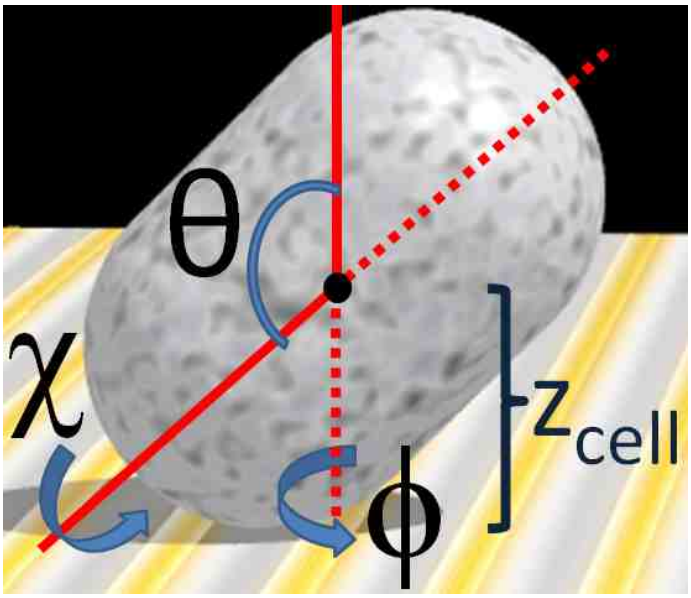

Figure 50: The three orientation angles for a lozenge shaped cell and Z_{cell}, the distance the between the target surface and the bacterium center.

6.6 Cell-to-Surface Binding Equilibrium Constant

In order to calculate the equilibrium constant for the binding of cells to a target surface (K), the relationship between K and $W(z_{cell})$ must be derived. The equilibrium constant for binding between a given bulk concentration of cells, c, and an equilibrium concentration of surface cells, σ, is given by

$$K = \frac{\sigma/\sigma^{\theta}}{c/c^{\theta}}$$

Equation 29

where c^{θ} and σ^{θ} are standard state concentrations for the surface and the bulk respectively. The equilibrium constant can be measured experimentally by counting the number of cells on the target surface as a function of the bulk concentration. Using the pmf defined above, K can be predicted for surfaces with known patterns of materials. This allows the theory to be tested and should be useful for designing surfaces with new engineered properties.

To relate $W(z_{cell})$ to K, consider a grand canonical ensemble where a fixed volume (V) containing free bacteria in solution are in equilibrium with the target surface. The volume of the system allows both cells and the medium to exchange freely with the surrounding solution. The bacterial solution acts as temperature (T) and pressure (P) baths and as a bath for the chemical potential (μ) of the bacterial cells. The cells are assumed to be at a low enough concentration so cell-to-cell interactions can be ignored. We consider two cases: (1) The cell-to-target pmf, $W(z_{cell})$, includes all interactions between the cell and target as outlined in the sections above. (2) We consider a fictitious

potential, $W_0(z_{cell})$, for a purely repulsive, hard surface which includes only the deform energy of the cell.

$$W_0(z_{cell}) = -k_B T \ln\left[\frac{1}{8\pi^2}\int_0^{2\pi}\int_0^{2\pi}\int_0^{\pi} \sin\theta \, d\theta d\phi d\chi e^{-\beta(\Delta G_{\text{deform}})}\right]$$

Equation 30

$W_0(z_{cell})$ accounts for cells that would be present in any situation simply due to random motion and not as a result of active binding. Binding to the surface is then equivalent to switching from $W_0(z_{cell})$ to $W(z_{cell})$. The difference in the number of cells inside V at equilibrium between these two potentials can be used to find the equilibrium constant.

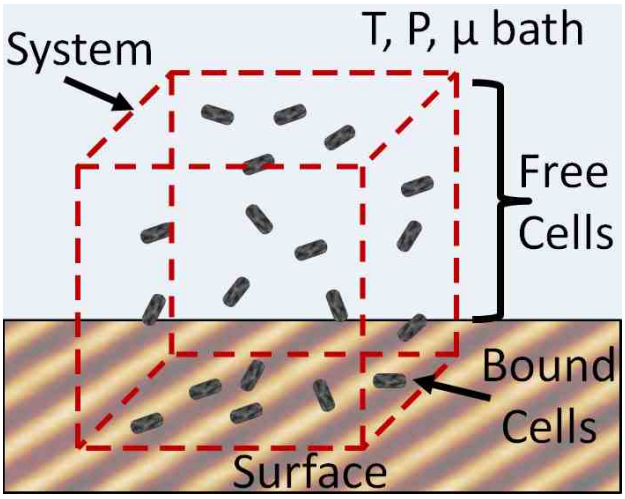

Figure 51: The setup for the grand canonical ensemble where a system of bacteria exist both in solution and on a surface surrounded by infinite T,P, and μ baths.

The characteristic free energy for a grand canonical ensemble is

$$\Phi[W(z_{cell})] = E - TS - \mu N$$

Equation 31

where E is energy, T is temperature, S is entropy, μ is the cell chemical potential, and N is the total number of cells in volume V. The grand free energy $\Phi[W(z_{cell})]$ can be considered a nonlinear functional the pmf $W(z_{cell})$. Our purpose is to derive this functional. For both the $W(z_{cell})$ and $W_0(z_{cell})$ cases, change in the grand potential is given by

$$\mathrm{d}\Phi[W(z_{cell})] = -PdV - SdT - Nd\mu$$

Equation 32

The corresponding grand canonical partition function is

$$\mathrm{e}^{-\beta\Phi[W(z_{cell})]} = \sum_{N} Q(N,V,T)e^{\beta\mu N}$$

Equation 33

where Q(N,V,T) is the canonical partition function for the system. For independent cells, $Q = q^N/N!$ where q is the canonical partition function for one particle. Replacing Q and solving for $\Phi[W(z_{cell})]$ in Equation 33 then gives

$$\Phi[W(z_{cell})] = -k_B T q e^{\beta\mu}$$

Equation 34

As can be seen in Equation 32, the number of cells in V is the partial derivative of the grand potential with respect to the bath chemical potential with the temperature and volume held constant.

$$N = -\left.\frac{\partial\Phi[W(z_{cell})]}{\partial\mu}\right|_{T,V} = qe^{\beta\mu}$$

Equation 35

The difference in the number cells, ΔN, between $W_0(z_{cell})$ and $W(z_{cell})$ potentials is then

$$\Delta N = e^{\beta\mu}(q[W(z_{cell})] - q[W_0(z_{cell})])$$

Equation 36

where the canonical partition function for one cell is shown as a functional of the pmf. For a single cell interacting with a target surface, the canonical partition function is:

$$\mathrm{q} = \frac{\mathrm{q_{int}}}{\Lambda_{\mathrm{D}}^3}\iiint \mathrm{dV}\,\mathrm{e}^{-\beta W(z_{cell})}$$

Equation 37

here Λ_D is the thermal de Broglie wavelength,

$$\Lambda_D = \sqrt{\frac{h^2}{2\pi m k_B T}}$$

Equation 38

where m is the mass of a cell. The quantity q_{int} accounts for all the internal variables of the cell, including the interactions of the cell with the surrounding solvent. The integral is over the volume of the system box.

Therefore the change in the number of cells is

$$\Delta N = e^{\beta\mu} \frac{q_{int}}{\Lambda_D^3} \iiint dV \left(e^{-\beta W(z_{cell})} - e^{-\beta W_0(z_{cell})}\right)$$

Equation 39

The factors in front of the integral can be rewritten in a much simpler form. The chemical potential for cells in the bath is

$$\mu = \frac{\partial A_H}{\partial N}$$

Equation 40

where A_H is the Helmholtz free energy for free cells.

$$A_H = -k_B T \ln\left(\frac{q^N}{N!}\right)$$

Equation 41

Where for this case

$$q = \frac{q_{int}}{\Lambda_D^3} V$$

Equation 42

Rearranging the above chemical potential equation yields

$$e^{\beta\mu} = \frac{N}{V}\frac{\Lambda_D^3}{q_{int}} = c\frac{\Lambda_D^3}{q_{int}}$$

Equation 43

Where c is the cell number density, or bulk concentration, as in Equation 29 above. This simplifies Equation 43 to

$$\Delta N = c \iiint \mathrm{dV} \left(\mathrm{e}^{-\beta W(z_{cell})} - \mathrm{e}^{-\beta W_0(z_{cell})} \right)$$

Equation 44

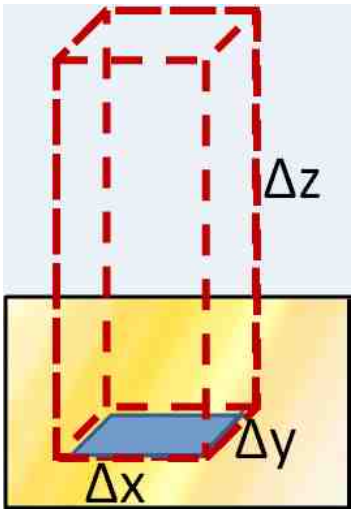

Figure 52: An example narrow box on the surface that is smaller than the area fractions.

Further simplification can be achieved by considering the case of a narrow box extending from the surface (see Figure 52). The lateral dimensions of the box are smaller than the area patches on the target surface and has an area of $\Delta x \cdot \Delta y$. Since the $W(z_{cell})$ and $W_0(z_{cell})$ potentials only depend on z_{cell}, the above integral reduces to

$$\sigma = c \int_0^{\infty} \mathrm{dz} \left(\mathrm{e}^{-\beta W(z_{cell})} - \mathrm{e}^{-\beta W_0(z_{cell})} \right)$$

Equation 45

Comparing to Equation 29 we see that

$$K = \frac{\mathrm{c^o}}{\sigma^o} \int_0^{\infty} \mathrm{dz} \left(\mathrm{e}^{-\beta W(z_{cell})} - \mathrm{e}^{-\beta W_0(z_{cell})} \right)$$

Equation 46

6.7 PWA Integrator Results

Initial calculations were performed by PWA Integrator on a model bacterium of an ideal lozenge shape with a length of 900 nm and a diameter of 600 nm (see Figure 53a). Several initial test cases were calculated to obtain a better understanding of the cell-target system. Figure 53b shows a graph of $W(z_{cell})$ and $W_0(z_{cell})$, for a cell with a single pure material binding to a single pure material target. The cell and target are weakly attractive for $W(z_{cell})$ while $W_0(z_{cell})$ shows the interaction for two non-adhesive materials. For $W_0(z_{cell})$, the pmf simply decreases in free energy as the cell moves away from the target and gains rotational entropy. For $W(z_{cell})$, the energy curve is more complex. A global minimum is present at the height where the cell is laying down on the target, but is not being compressed. This represents the maximum contact area for the two attractive potentials. There is a second, local energy minimum that corresponds to the cell only contacting the target at one of its poles (with its major axis perpendicular to the surface), creating a spinning top-like orientation. Between this arrangement and the full-contact minimum, there is a slight energy barrier that comes from the loss of entropy as cell rotation becomes hindered by the presence of the target. The cell must be at a relatively low height with respect to the surface before favorable binding conditions overcome the loss of rotational entropy. Therefore, in a population of many cells with this type of surface interaction, a small percentage of tip standing, spinning top-like orientations should be present alongside the much more numerous fully bound cells. As mentioned above, this behavior has been observed in rod shaped bacteria[243, 244] though the material distributions of real cells and surfaces are much more complex.

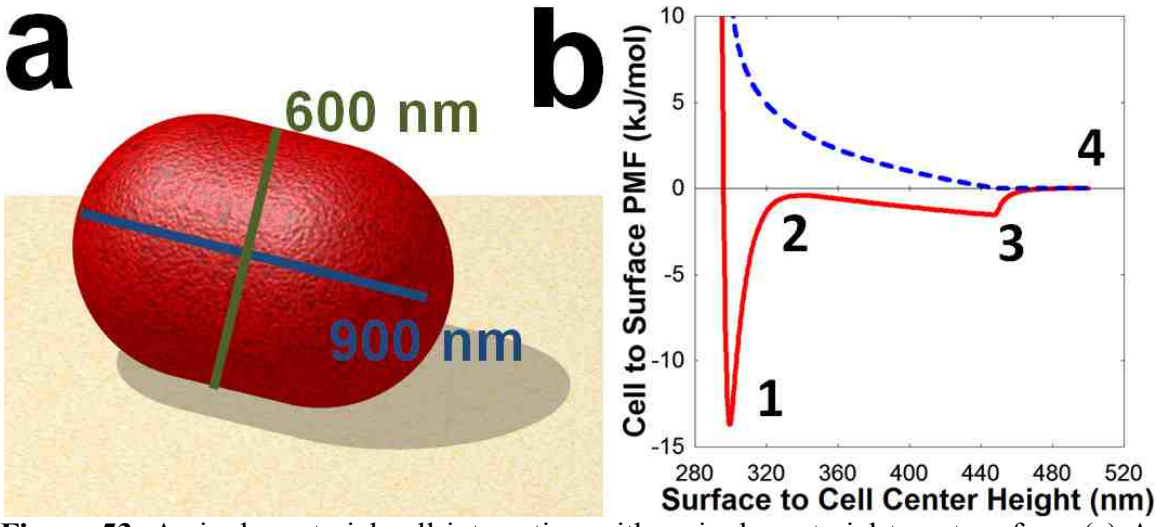

Figure 53: A single-material cell interacting with a single-material target surface. (a) A bacterium is taken to be an ideal lozenge shape with a major axis of 900 nm and a minor axis of 600 nm. (b) A graph of the cell-to-target pmf, $W(z_{cell})$, for a single-material cell interacting with a single-material, adhesive target surface (red, solid line), and the cell-to-target pmf, $W_0(z_{cell})$, for a neutral interaction (blue, dashed line). The surface tension between the cell and the attractive surface is -0.0007 dyne/cm. (1) The cell is flat on the surface, maximizing surface contact. (2) Cell-target interactions are neutral. (3) The cell is far enough away from the surface so that only the tip can contact the surface. (4) The cell is completely off the surface.

Figure 54 shows a case where a single material cell is brought into contact at various points along a two material patterned target. The surface contains two materials, one attractive and the other neutral to the cell, arranged in a cosine wave pattern with a wavelength of 500 nm along the x-axis. The equilibrium constant for a cell binding to a surface will depend on the type of material it encounters, therefore for this surface K will vary across the x-axis of the target. This is shown in Figure 54b, where the equilibrium constant strongly favors binding at the center locations of the attractive target material. This quickly drops in even slightly off-alignment positions, even though there is no repulsive material involved. Thus, on patterned surfaces, cells are expected to preferentially bind along adhesive regions. This hints at an interesting phenomenon explored in more detail in Figure 55.

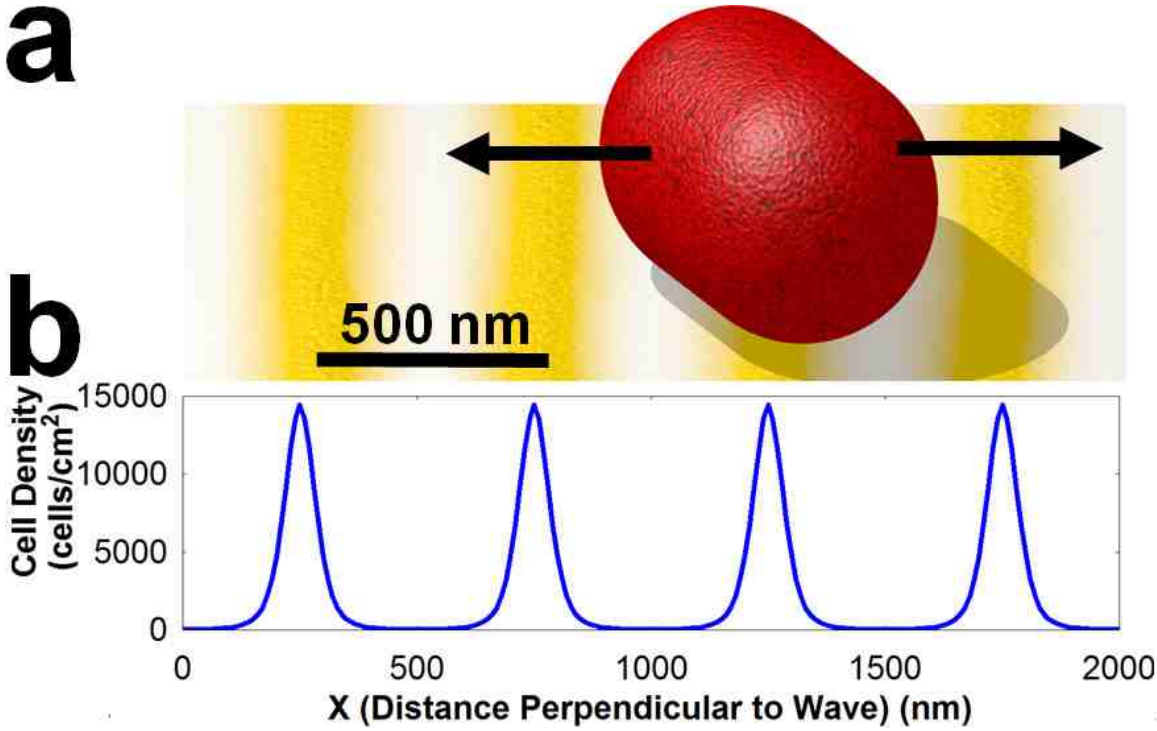

Figure 54: A single material cell interacting with a two material target surface. (a) The materials on the target are patterned as a cosine wave with a wavelength of 500 nm along the x-axis. The equilibrium constant K depends on the location of the cell along the target pattern. One of the target materials is neutral towards the cell, while the other has a surface tension of -0.0015 dyne/cm. (b) A graph of the cell density (for a bulk concentration of 10^6 cells/cm^3) as a function of the cellular center location on the target.

Figure 55 shows the effects of pattern resonance between a two material patterned cell interacting with a two material patterned target. The materials on both the cell and the target are patterned as a cosine wave, but the cell's pattern is kept constant at a wavelength of 100 nm while the wavelength of the target varies for each calculation. If the two pure materials on the cell are labeled (m1) and (m2) and the two pure materials on the target are labeled (m3) and (m4), then (m1) is attractive toward (m3) and repulsive toward (m4). Likewise, (m2) is attractive toward (m4) and repulsive toward (m3). As can be seen in Figure 55b, cell binding is greatly enhanced when the cell and target patterns match. However, even a slight misalignment causes the binding constant to rapidly decrease. Figure 55c shows $W(z_{cell})$ for the on-resonance case (surface

wavelength is 100 nm). Unlike the single material binding seen above, the two patterns cause an oscillatory response in the free energy, meaning the cell is locked into preferred tip-standing angles. This binding enhancement from pattern resonance suggests that attachment could, in principle, be controlled by pattern matching. Theoretically, it could be possible to preferentially bind to a selective bacterial population by creating a surface pattern that matches the distributions of select cellular proteins.

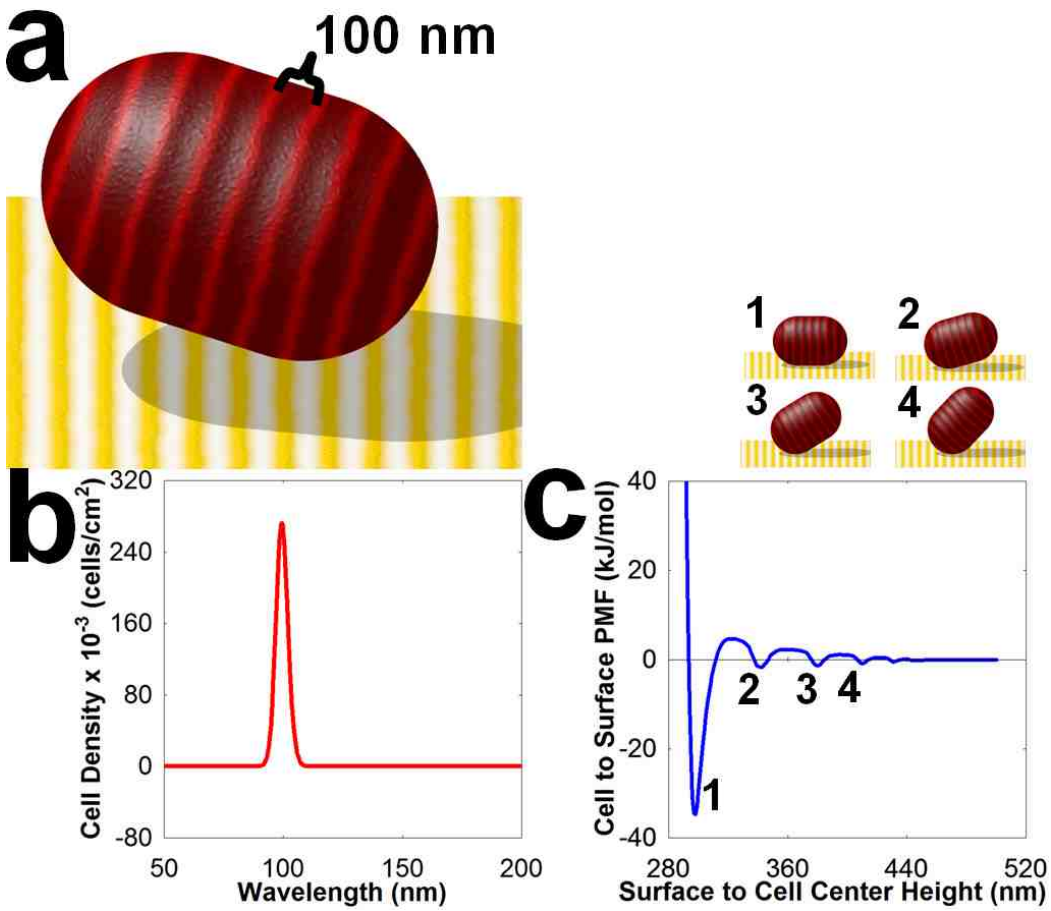

Figure 55: A two material cell interacting with a two material target surface. (a) The materials on the cell are patterned as a cosine wave with a wavelength of 100 nm along the surface. The wavelength of the target was allowed to vary. One material type on both the cell and target are attractive (surface free energy of -0.003 dyne/cm) while the second material type on each are repulsive (surface free energy of 0.003 dyne/cm). (b) A graph of the cell density (for a bulk concentration of 10^6 cells/cm^3) as a function of the target pattern wavelength. The peak corresponds to a target wavelength of 100 nm. (c)A graph of $W(z_{cell})$, as a function of distance, for a target wavelength of 100 nm. Images (1-4) correspond to different cell heights where full (1) or partial (2-4) cell and target pattern alignment occurs.

6.8 Future Work

Due to the inherently complex nature of bacterial surface composition, bacteria attachment to surfaces has received little attention from multiscale computational modeling.[256] PWA Simulator and PWA Integrator attempt to quantify bacterial composition and attachment in order to create a predictive model for both dynamic and equilibrium bacterial attachment. Surfaces are quantized into area fractions of pure materials whose surface attachment energies can be independently obtained through experiment. The potential of mean force is calculated via surface integration and can be used to determine the equilibrium constant for cell-to-target attachment. Direct comparison of area coverage between the model and experimental results can further parameterize and refine the program.

The development of PWA Integrator and PWA Simulator is still ongoing. One possible improvement to the models can come from the Atomic force microscopy (AFM) imaging currently ongoing as part of the DTRA grant project. AFM images of biocidal surface and of bacterial surfaces have the ability to provide experimental models for the surface area distributions utilized by the program (see Figure 56 for an example of an AFM imaged bacterial surface)[257]. The next two chapters provide a more detailed explanation of the AFM results.

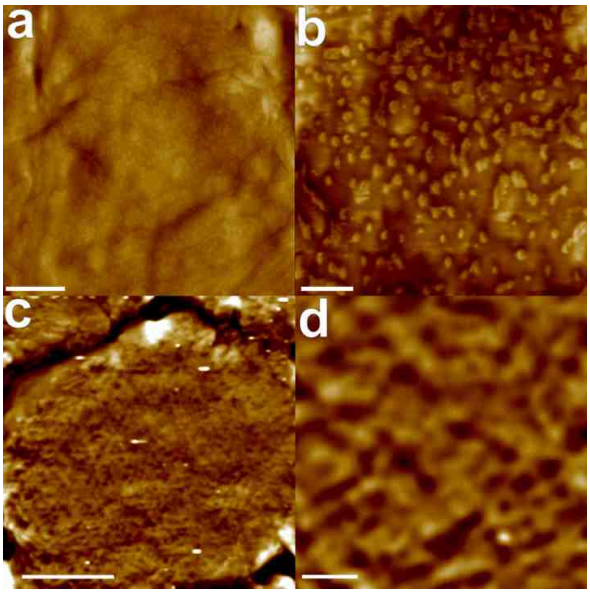

Figure 56: AFM air image of dried bacterial surfaces. Dried *E. coli* showing surface detail. Scale bar is 100 nm. (b) Higher resolution scan of the *E. coli* surface. Scale bar is 50 nm. (c) Dried *Staphylococcus aureus* showing surface detail. Scale bar is 250 nm. (d) Zoomed image of the *S. aureus* surface. Scale bar is 50 nm.

7. ATOMIC FORCE MICROSCOPY

7.1 Introduction

Atomic Force Microscopes (AFMs) provide a means to measure and image nano and piconewton forces on the nanometer scale. The AFM was invented by Gerd Binnig in 1986[258], with a prototype introduced later that year by Binnig, Calvin Quate, and Christoph Gerber[259]. The AFM was developed as a follow-up device to the then 5 year old Scanning Tunneling Microscope (STM), for which Binnig and Heinrich Rohrer were awarded the Nobel Prize in Physics[260]. One of the main limitations of Scanning Tunneling Microscopy is its requirement for the electrical conduction of the sample material. The AFM was designed to work with any surface type with the goal of achieving atomic scale resolution. This was achieved in 1995 when Franz Giessibl imaged the Si(111)-(737) surface with atomic resolution[261,262].

AFMs function via a disposable chip on which is mounted a small, flexible cantilever containing a nanometer-sized tip on one side and a reflective surface on the other. The chip is mounted so a laser reflects off the back of the cantilever into a four quadrant photodiode detector (see Figure 57). As the tip interacts with a sample, the tip-sample forces deflect the end of the cantilever, changing the position of the reflected laser spot on the detector. Changes to the photodiode's voltage output are used in conjunction with a constant setpoint value (maintained by a signal feedback system) to determine the amount of cantilever deflection and create images.[263]

By calibrating the AFM to a known hard sample, the signal from the photodetectors can be related to the cantilever deflection. The tip deflection is kept fixed

at a certain setpoint value via an electronic feedback loop. This feedback loop acts to oppose changes in tip deflection due to surface features. The feedback loop circuit contains a proportional amplifier and an integrating amplifier, whose gains can be individually adjusted so as to optimize feedback stability. Proportional feedback acts as a multiplier that sets how fast the instrument responds to a deviation from the setpoint while Integral feedback looks at time averaged errors around the setpoint to correct the cumulative effects over a longer period of time.[263]

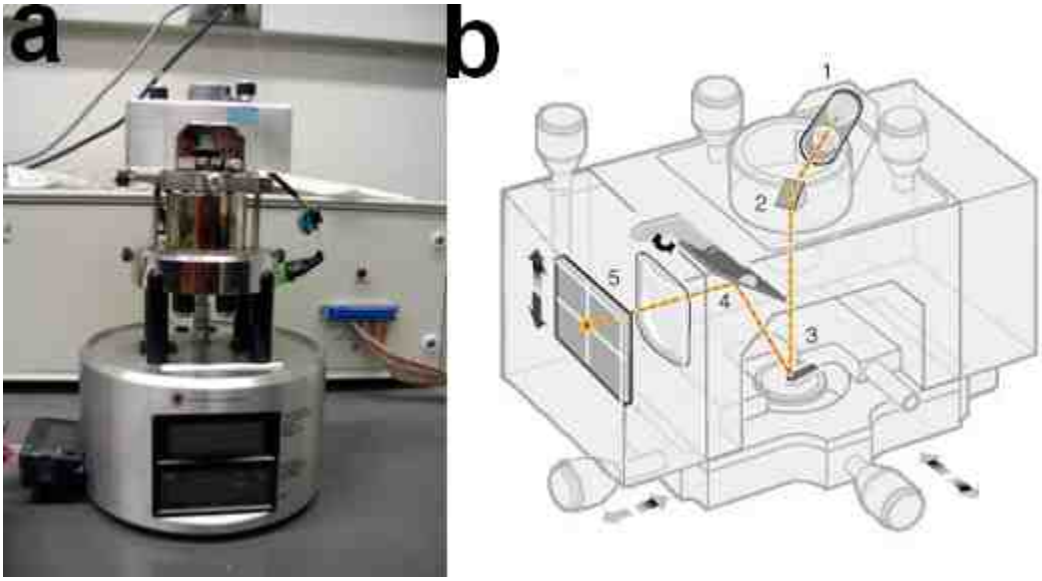

Figure 57: The Atomic Force Microscope. (a) Picture of the Nanoscope IIIa Atomic Force Microscope used to create the images below. (b) Diagram of an Atomic Force Microscope measuring head. The dotted yellow line indicates the path of the laser from its semiconductor diode laser emitting at 670 nm (1) into an initial static mirror (2), off the back of an aligned cantilever (3), into a second, adjustable tilt mirror (4), and finaly into a four quadrant photodetector (5).[263]

7.2 AFM Stage

Sample movement in an AFM is controlled by a piezoelectric stage. The scanner size determines the maximum image scan size and image resolution. Smaller scanners generally offer higher resolutions while larger scanners provide a wider scan size. Piezoelectric stages are composed of special non-conducting crystals (usually lead

zirconate titanates[264]) that utilize the piezoelectric effect where stress on the crystals generates a potential difference across opposite crystal faces proportional to the direction and amount of stress. Alternatively, applying a potential difference to the crystals causes a deformational change. Along the z axis of the scanner, the piezos expand and contract to move the sample in contact with the tip. In the xy plane, complimentary sections of piezos are arranged across from each other so that as one side expands, the other contracts, allowing for precise scans (see Figure 58). The AFM instrument applies potential differences to the stage to raster the sample under the tip, moving the sample in the x-y plane while adjusting the z height of the sample so as to keep the tip-sample forces (approximately) constant. Temperature changes can also affect crystal size and stress values, so there is always a small amount of stage drift in AFM images. The "image" is the voltage needed to keep the forces constant at each x-y position.[259]

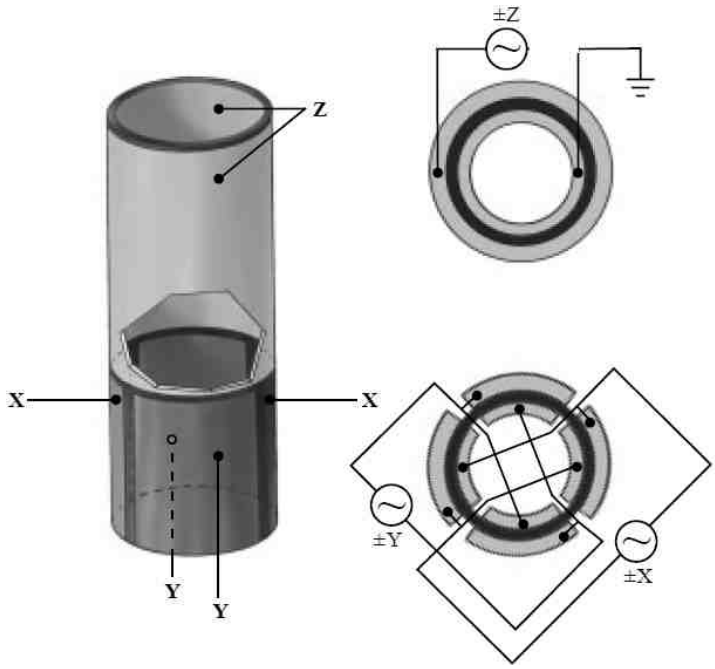

Figure 58: A schematic of a cylindrical AFM piezoelectric stage. Five electrodes (±x, ±y, and z) are arranged to allow for controlled movement in x, y, and z. Image from the AFM Instruction Manual.[263]

7.3 Tip-Sample Forces

Common tip-sample forces often include effects from van der Waals, chemical, electrostatic, and meniscus potentials. Image resolution is determined by the shape of the AFM tip and the atom-to-atom level forces between the very end of the tip and the target surface. The smaller the radius of curvature of the tip, the smaller the feature that can be resolved. During operation, the tip will commonly gather debris, which dulls the end and results in image distortion (and loss of resolution).

7.3.1 van der Waals Potential

Consider an ideal system where the surface is flat near the tip and the tip is assumed to be spherical with radius R near its tip (see Figure 59).

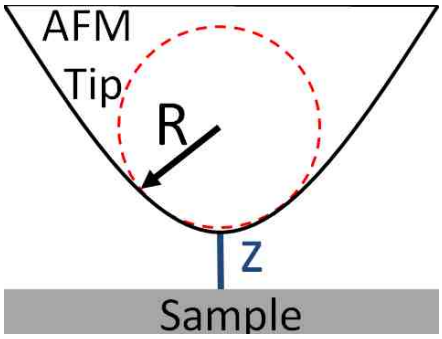

Figure 59: A diagram of an AFM probe tip interacting with a flat surface at a distance z. The end of the tip is assumed to be spherical with a radius of R.

The van der Waals potential (V_{vdW}) between two atoms in a vacuum is:

$$V_{vdW}(r) = -\frac{C_{vdW}}{r^6}$$

Equation 47

where C_{vdW} is the atomic van der Waals constant and r is the distance between the atoms.

Applying Hamaker integration, which replaces a sum over all atoms in a tip with a smooth atomic density, yields the simplified force, $F_{vdW}(z)$, relation between the tip and surface:

$$F_{vdW}(z) = -\frac{A_H R}{6z^2}$$

Equation 48

where A_H is the Hamaker constant (on the order of 0.1 aJ for most condensed materials.[262]) and z is the tip-sample distance. [265] As this approximation is dependent on the tip shape, tip changes (as are expected to occur after sample contact) will change the distance dependence of $F_{vdW}(z)$. In Figure 60 typical calculated van der Waal forces are shown for varying tip geometries as a function of tip-sample distance.[265]

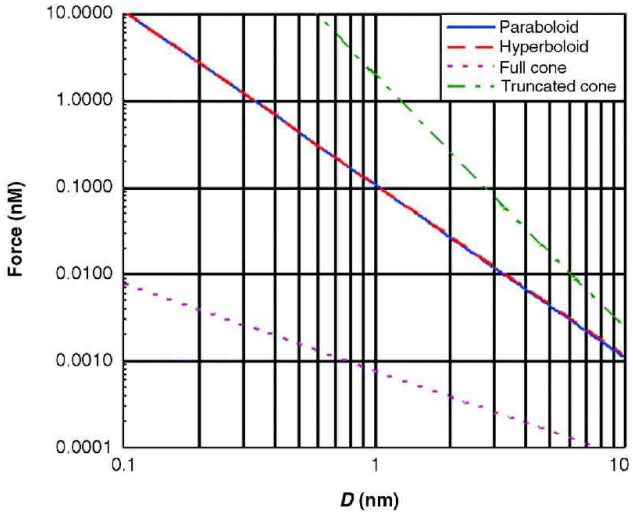

Figure 60: Calculated van der Waal forces for varying tip geometries as a function of tip-sample distance D. Image taken from Haugstad 2012.[265]

7.3.2 Electrostatic Potential

Related electrostatic force contributions can also become a major factor in tip-sample forces, even if no potential has been directly applied. Many samples (such as cleaned glass) carry a charge that can result in charge-charge or charge-dipole

interactions, depending on the tip composition. In a basic approximation, which uses a spherical tip and assumes the tip-sample distance z is small compared to the tip radius R, the electrostatic potential is

$$F_{elec}(z) = -\frac{\pi\epsilon_0 R E^2}{z}$$

Equation 49

where ϵ_0 is the permittivity of free space and E is the electrostatic potential difference. AFM tips also have the potential to form chemical bonds with the sample.

7.3.3 Water Meniscus Forces

When dealing with interfacial regions there are usually unique forces that must be accounted for. In the case of the AFM, when imaging in air, capillary forces from water are present at the tip-surface interface. Even if the ambient air's water vapor is below the gas to liquid transition point, water can condense on hydrophobic surfaces, in addition to spontaneous capillary condensation that can occur between two closely confinement surfaces. Water menisci can form between any two surfaces, but the air humidity and the hydrophilicity of the materials influence its formation. Figure 61a shows a diagram of a spherical tip near a flat surface that is surrounded by a water meniscus.[265]

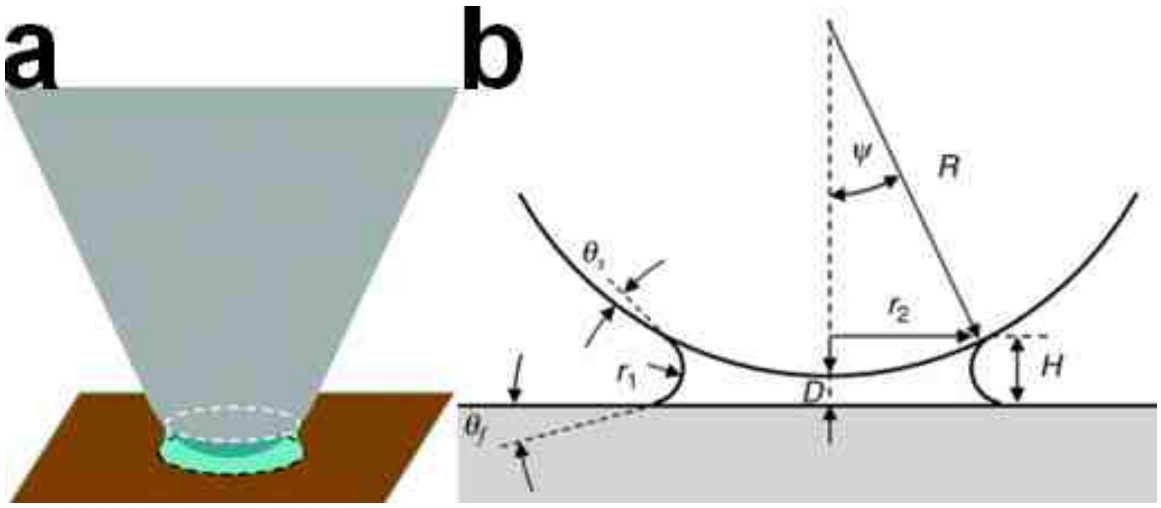

Figure 61: (a) Diagram showing a water meniscus between and AFM tip and a flat surface. (b) A cross-section detailing the geometry of a meniscus between a non-contacting tip and a surface. Image taken from Haugstad 2012.[265]

The forces associated with water menisci are very strong at the AFM scale and can overwhelm all other tip-samples forces. Meniscus forces are always attractive, with surface tension acting to pull the tip down toward the surface. A diagram is shown in Figure 61b. Surface tension at the air-water interface acts in all directions to pull water together; however, the net forces felt by the tip from this tension cancel out in the horizontal directions leaving the remaining vertical attractive component forces. Surface tension and the curvature of the air-water interface also lead to the Laplace force, which is caused by the fact that the negatively curved water surface causes the water pressure under the tip to be lower than the surrounding atmospheric pressure. This pressure differential produces an attractive force between the AFM tip and the surface. Interestingly, within the meniscus other attractive forces such as van der Waals and electrostatic forces are reduced in magnitude by the water environment. However, the meniscus more than compensates as capillary forces are stronger than any other force acting on the tip. Figure 62 shows typical forces for an idealized constant curvature water

meniscus. In reality, the geometry of the meniscus is so dependent on vapor pressure and defects on both the tip and the surface that these forces can vary by 10s of nN even during imaging.[265]

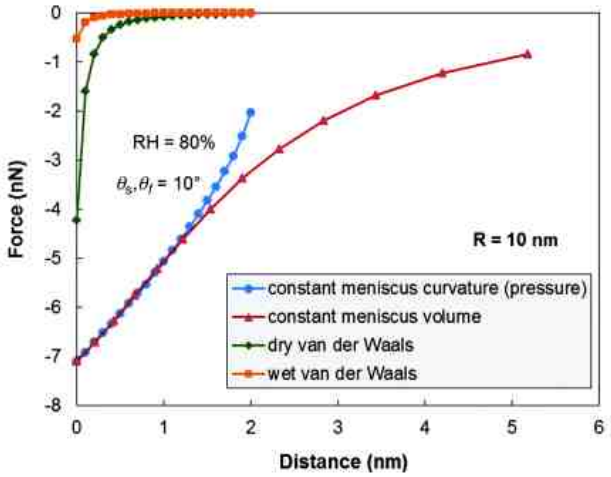

Figure 62: Distance dependences of water capillary forces under different ideal assumptions. Image taken from Haugstad 2012.[265]

7.3.4 AFM Cantilever Spring Constant

The cantilever responds to the above forces as a mechanical spring. This response can be modeled to a first approximation (i.e. assuming linear elasticity) with Hooke's Law

$$F = -\kappa \cdot d$$

Equation 50

where the force (F) felt on the tip is equal to the spring's force constant (κ) times the tip displacement distance (d).[266] Hooke's Law is used to determine AFM forces, especially when using an instrument mode called Force AFM. In this mode the tip is not raster scanned across the surface to create an image but instead brought carefully down to a single contact point and pulled away. In order to relate the deflection of the tip to the deformation forces, a measurement of the spring constant, κ, is required. There are

several ways to measure κ, such as the thermal method from Hutter and Bechhoefer[265, 267]. The thermal method measures the effect of the thermal noise of the instrument and surrounding environment on the tip. The tip fluctuations (characterized across a wide band range of frequencies) are assumed to be vibrations of a one-degree of freedom free oscillator. The equipartition theorem[265] then relates thermal noise (the Boltzman constant k_B times the temperature T) to the spring constant (κ) times the mean squared position of the tip averaged over time ($\langle x^2 \rangle$):

$$\frac{1}{2}\kappa\langle x^2\rangle = \frac{1}{2}\mathrm{k_B T}$$

Equation 51

By measuring the mean-squared thermal fluctuations of the cantilever, it is then possible to estimate the spring constant.

7.4 Types of AFM cantilevers

The thermal method (and force AFM in general) makes use of several assumptions, the primary being cantilever geometry.[265] (Cantilever geometry should not be confused with tip geometry, as the latter deals with the shape of the sample contact point.) For several AFM modes (such as force, friction, and tapping mode), cantilevers with a beam or "diving board" geometry are required (see Figure 63b). Diving board tips are generally more sensitive to the environment, but present a simpler geometry. In contrast, AFM imaging can employ V-shaped or triangular cantilevers (see Figure 63a). These cantilevers contain two supporting arms, forming a triangular shape that is less sensitive to the environment. They are especially good at reducing torsional or twisting motions. Both cantilever geometries follow the general rule that the large cantilevers have smaller spring constants. In addition, as the angular displacement of the reflected

laser beam is inversely proportional to the cantilever length; longer cantilevers offer a larger (and hence easier to measure) laser deflection across the photodetector. This is balanced against the above mentioned attractive forces, as a cantilever must have a high enough spring to prevent it from becoming trapped by the surface.[263]

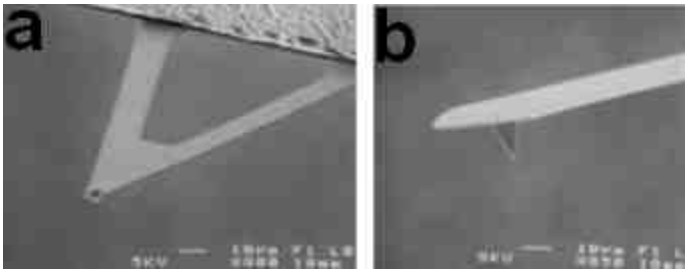

Figure 63: Two types of AFM cantilevers. (a) triangular silicon nitride cantilever (b) diving board silicon cantilever[263]

Cantilever stiffness is also directly related to its primary resonance frequency, the key aspect of tapping (or altering force) mode AFM. Tapping mode AFM is an alternate imaging mode where a small electromagnet induces oscillation of the cantilever. After an initial frequency sweep, the drive frequency is set to match the 1st order harmonic mode of the cantilever. Deflections from the nominal oscillation are measured (instead of absolute deflection) as the tip is brought into contact with a surface. During imaging, the tip only directly contacts the surface at intervals instead of the constant contact required by contact mode. This method reduces tip-sample interactions (preserving the native state of both for a longer period of time) in exchange for a slight resolution loss. For imaging biological samples, tapping mode is usually the preferred method as it helps retard the transfer of material from the surface to the tip, a common problem with soft organic surfaces (see Figure 64).

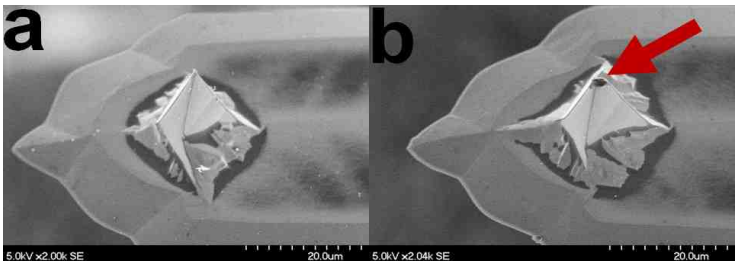

Figure 64: SEM image of a tapping mode cantilever and tip. (a) unused tip (b) tip after it has been damaged (arrow showing missing tip end) and rendered useless

8. BIOCIDAL ACTIVITES AND BACTERIAL ADHESION ON MULTIFUNCTIONAL SURFACES

8.1 Introduction

Atomic force microscopy is a common method for creating high resolution images of cellular surfaces in air and also has the ability to image living cells in solution.[268-272] To explore the effects of the antimicrobial action of the above mentioned PPEs and OPEs (see Chapter 5), we obtained a series of AFM images for several biological systems. For an initial trial, we imaged a selection of supported lipid bilayers on mica before and after exposure to PPE-NMe3-Th and OPE-2. The loss of lipid coverage after the introduction of the biocide prompted further investigating on full bacterial cells.

Using AFM (and TEM via collaboration), we generated high-resolution images of cell surfaces in air and in solution after (or during) exposure to PPE-Th and EO-OPE-1(C3). One goal was to confirm the mechanism of dark killing by cellular disruption proposed by Wang et al.[273] by observing changes in the cell surfaces. The presence of surface aggregates on the bacterial surface after *E. coli* was exposed to PPE-Th supports a mechanism where the biocide causes large enough surface disruptions to kill the cells. The absence of similar aggregates for the EO-OPE-1(C3) case is also consistent with the hypothesized mechanism. In this case, the oligomer penetrates the outer cell membrane, causing channel formation that ultimately results in cell death. A series of real-time AFM images of live *E. coli* cells exposed to EO-OPE-1(C3) in solution shows increasing cell surface disruption with length of time after the introduction of EO-OPE-1(C3).

Following experiments with solution-based PEs, the biocidal action of surface bound PPEs was explored. As part of the multi-university effort under the DTRA project, mixed surfaces of PNIPAAm and PPE bilayers were fabricated and characterized. At the University of New Mexico, the mixed surface of primary interest consisted of a 3-layer film of PPE-DABCO, PPE-SO3, and PPE-DABCO (in that order), followed by PNIPAAM polymerization. This produced a surface with a random mixture of PPE and SRP materials, which was characterized by AFM imaging and its biocidal properties were tested using live/dead assays.

8.2 Experimental Setup

8.2.1 PPEs

The antimicrobial materials used in this study were synthesized as previously reported (see Chapter 5.3).[274, 275] The exact molecular weight of the CPE polymer is not known, but the average molar mass value is estimated to be within the range of 20-30 kDa. *Escherichia coli* (ATCC 11303) was obtained from the American Type Culture Collection ATCC (Manassas, VA) and grown in standard Luria broth. A fresh bacterial culture was inoculated from an overnight culture followed by ~3 h of incubation at 37°C, which stimulated the exponential growth phase, after which the cells were collected by centrifugation. The collected cell pellet was washed twice with 10 mM phosphate-buffered saline (PBS) (138 mM NaCl and 2.7 mM KCl at pH 7.4) and then was resuspended in distilled water for AFM imaging.

8.2.2 Lipid bilayers

4 μg/ml DMPC (1,2-ditetradecanoyl-sn-glycero-3-phosphocholine) liposomes were suspended in a solution of 10 mM MgCl2 and pipetted onto freshly cleaved mica. The solution was allowed sit in a humid environment for 15 min.

Liposomes of 4 μg/ml *E. coli* lipids (mixtures of phosphatidylethanolamines (~57%) phosphatidylglycerol (~15%) and cardiolipin(~10%) and other (~18%) lipids) were suspended in a solution of 10 mM MgCl2 1 mM PBS and pipetted onto freshly cleaved mica. The solution was allowed sit in humid environment for 15 min.

8.2.3 Electron Microscopy

Fresh bacterial cells in the exponential growth phase ((1–4) × 10^8 colony forming units (CFU)/mL) were incubated in a 0.85% NaCl sterile solution and various amounts of CPEs or OPEs and kept in the dark at 37°C for 1 h before being imaged by TEM as previously described.[240, 273] Briefly, the cell pellets were fixed with 2% glutaraldehyde for 1 day and then stained with 1% osmium tetroxide (a lipid stain) for 1 h at room temperature. The samples were then dehydrated by sequential treatment with increasing concentrations of ethanol, embedded in resin (Spurr's resin kit, Electron Microscopy Sciences, Hatfield, PA), sectioned, and imaged by TEM (Hitachi H7500, Tokyo, Japan).

8.2.4 Cleaning

Glass coverslips (VWR microglass 12 mm no. 2) were placed in piranha solution (3:1 H2SO4/H2O2 stock concentrations) for 2 h. The coverslips were then rinsed with nanopure water and dried under a flow of N2.

8.2.5 Air Imaging

Air-dried samples were prepared by pipetting 25 μL of 10^8 cells/mL *E. coli* in distilled water solution onto a cleaned glass coverslip. The cells were allowed to physisorb in a closed Petrie dish at 100% humidity (to prevent evaporation) for 1 h before being gently rinsed with 0.5 mL of nanopure water. The sample was then thoroughly dried under N2 gas. Imaging was performed using a Nanoscope IIIa atomic force microscope (AFM) in tapping mode under a constant flow of dry N2 gas using a rectangular silicon cantilever with a spring constant of 40 N/m (Veeco model RTESPAW). Standard Veeco imaging software (Nanoscope V531r117) was used to capture and analyze the images.

8.2.6 Underwater Imaging

For underwater imaging of the bacterial cells, cleaned coverslips were first coated with Cell-Tak adhesive protein.[276] The Cell-Tak solution[276] was 57:2:1 NaHCO3(0.1 M)/Cell-Tak(stock)/NaOH(1 M). The Cell-Tak solution (50 μL) was pipetted onto a cleaned glass coverslip. The sample was allowed to absorb for 1 h (in a closed container with 100% humidity) before being gently rinsed with 0.5 mL of nanopure water. The slides were then thoroughly dried under N2 gas. To deposit cells, a solution containing 10^8 cells/mL *E. coli* in distilled water solution was pipetted onto the Cell-Tak-covered slides. The sample was allowed to dry in air until approximately two-thirds of the initial droplet evaporated. The sample was then mounted for imaging in an AFM fluid cell. Before imaging, the fluid cell was flushed with nanopure water to remove loose cells. All fluid images were taken with triangular silicon nitride cantilevers (Veeco model SNL-10

with force constant 0.32 N/m) in a fluid cell containing either nanopure water or 30 μg/mL EO-OPE-1(C3) in water. Standard Veeco imaging software (Nanoscope V531r117) was used to capture and analyze the images.

For underwater imaging of supported lipid bilayers, the samples were mounted for imaging in an AFM fluid cell. For the DMPC lipids, initial images were obtained with triangular silicon nitride cantilevers (Veeco model SNL-10 with force constant 0.32 N/m) in a fluid cell containing 10 mM $MgCl_2$. Subsequent images were obtained after 5 or 20 μg/mL of PPE-NMe3-Th in 10 mM $MgCl_2$ was injected into the fluid cell via a tube system that minimized possible movement on the sample. For the *E. coli* lipids, initial images were obtained with same setup described above where the fluid cell was filled with 10 mM $MgCl_2$ 1 mM PBS. Subsequent images were obtained after 5 or 50 μg/mL of OPE-2 in 10 mM $MgCl_2$ 1 mM PBS was injected into the fluid cell. Standard Veeco imaging software (Nanoscope V531r117) was used to capture and analyze the images.

8.2.7 Image Processing

All postcapture image processing was performed using the Veeco Nanoscope V531r1 imaging software.[277] All images except those in Figure 70 first underwent an initial plane fit (order 3, no threshold). Then every image was passed through a lowpass filter to smooth feedback noise and artifacts. Images in Figure 67-Figure 69 without a scale bar were passed through an additional Spectrum2D (Fourier) filter to enhance the image contrast. To highlight sharper features and eliminate gross surface curvature, a Gaussian highpass was applied to Figure 70d−m. In this dissertation the term real-time zoom means a higher-resolution image created by reducing the AFM scan size while

capturing data, but the term software zoom means a higher-magnification image created by interpolation from a previously captured image. A real-time zoom thus has higher resolution while a software zoom has only higher magnification. The histogram in Figure 67d was calculated from the AFM image by highlighting select features by hand (with an approximate threshold height of 8 nm relative to the local background). A binary image was created by setting the highlighted features to one and the nonhighlighted surroundings to zero. The binary image was analyzed in ImageJ, which output the pixel-by-pixel areas of all nonzero features. The pixel areas were then converted to physical areas for the histogram in Figure 67d.

8.3 Experimental Results

8.3.1 Lipid Bilayers

Figure 65 shows a pair of before and after images detailing the effects of PPE-NMe3-Th on supported DMPC lipid bilayers at two concentrations. Figure 65a is a 1 μm × 1 μm image of a lipid bilayer island. The island shows two differe nt height levels, suggesting that either the bilayer is not fully attached to mica (more likely) or the island is a monolayer in some places. The same lipid island is shown again in Figure 65b approximately 4 minutes after exposure to 5 μm/mL PPE-NMe3-Th. Disruption of the bilayer is clearly evident in increased roughness of the island's outer edge, the formation of holes in the bilayers, and an overall loss of surface area. This disruption is even more dramatic with a higher polymer concentration.

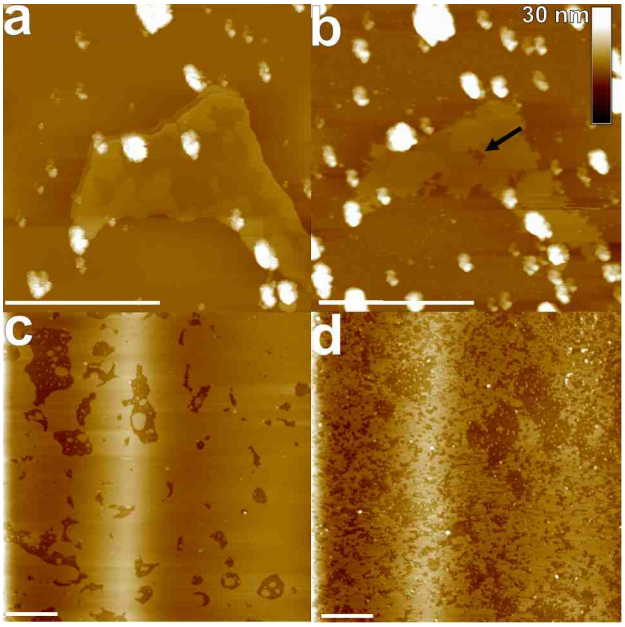

Figure 65: AFM underwater scans of DMPC lipid bilayers exposed to PPE- NMe3-Th. (a) 1 µm × 1 µm image of a DMPC lipid bilayer island. (b) 1 µm × 1 µm scan of the same lipid island after exposure to 5 µm/mL PPE-NMe3-Th showing bilayer removal and holes (arrow). (c) 3 µm × 3 µm image of nearly complete DMPC lipid bilayer coverage. (d) 3 µm × 3 µm scan of the same lipid area after exposure to 20 µm/mL PPE-NMe3-Th showing increased bilayer removal. All scale bars are 500 nm. The height scale in the upper right applies to all the images. The bright, high bar region in (c) and (d) is an artifact of the AFM image processing.

Figure 65c shows a 3 µm × 3 µm image of a surface mostly covered in a DMPC lipid bilayer. While this surface was prepared using the same method in Figure 65a, this particular region happened to have a high lipid coverage with smooth-edged holes exposing the mica surface underneath. Figure 65d is a 3 µm × 3 µm image of roughly the same lipid covered area (the image is slightly shifted to the right) approximately 4 minutes after exposure to 20 µm/mL PPE-NMe3-Th. In this case the polymer has caused clear disruption to the bilayer. Edges are no longer smooth and many new holes have appeared in the lipid coverage (arrow in Figure 65b).

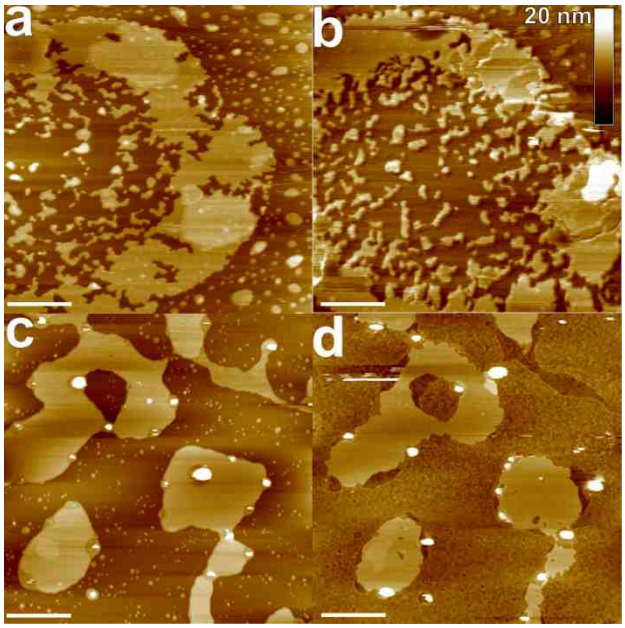

Figure 66: AFM underwater scans of *E. coli* lipid bilayers exposed to OPE-2. (a) 2 μm × 2 μm image of *E. coli* lipid bilayers. (b) 2 μm × 2 μm scan of the same lipid area immediately after exposure to 5 μm/mL OPE-2 showing reduced bilayer coverage. (c) 2 μm × 2 μm image of *E. coli* lipid bilayer islands. (d) 2 μm × 2 μm scan of the same lipid islands immediately after exposure to 50 μm/mL OPE-2 showing increased bilayer removal. All scale bars are 500 nm. The height scale in the upper right applies to all the images.

Figure 66 shows a pair of before and after images detailing the effects of the oligomer OPE-2 on supported *E. coli* lipid bilayers at two different concentrations. Figure 66a is a 2 μm × 2 μm image of lipid bilayer islands. As in Figure 65a, these islands display two height levels. The same area is shown again in Figure 66b approximately 4 minutes after exposure to 5 μm/mL OPE-2. While some disruption of the bilayers is evident in reduced area coverage, the effect is not as dramatic as in the PPE polymer example. Figure 66c shows a 3 μm× 3 μm image of an unexposed area of *E. coli* lipid islands. These islands are shown again at the same scale in Figure 66d approximately 4 minutes after the introduction of 50 μm/mL OPE-2. In this case, the OPE not only caused the formation of holes in the bilayers and an overall loss of surface area, but also increased the roughness of the mica surface. The increased background roughness is

likely due to excess oligomer or lipid-oligomer complexes in the surrounding solution. Again the results for the biocidal oligomer are not as dramatic as the polymer case, but these images utilized the more biologically-relevant *E. coli* lipids. Still, it is evident both the polymer and the oligomer can act as surfactants to supported lipid bilayers; though they may operate through different mechanisms.

These polymer and oligomer experiments served as an initial step in determining the dark biocidal mechanism of the PE biocides. They indicated that the lipid membrane was a possible target for these materials. In further studies, Wang et al.[273] showed that PPE polymers and oligomers have different mechanisms for the dark killing of Gram-negative bacteria. The oligomer EO-OPE-1(C3) causes fusion and membrane failure in large unilamellar vesicles (LUVs), along with significant cell envelope disruptions and time-dependent cell cytoplasm release in TEM images of exposed *E. coli*. In contrast, the PPE polymer causes LUV degradation and, in TEM images, forms large surface debris on bacterial cell envelopes. Longer PPE polymers cause sudden ruptures of LUVs and roughen the outer cell surface with the formation of aggregate clumps. PPE-Th is thought to cause major disruption of the cellular membrane, possibly through an ion-exchange process. Alongside that work, studies utilizing the AFM imaged the effects of PE biocides on native bacterial surfaces both in air and underwater.

8.3.1 Air Images: Cells Only

Figure 67a shows a 5 μm× 5 μm AFM scan of a continuous layer of air-dried *E. coli* cells. The drying process concentrates the cells, producing a solid layer that is self-supporting and hence able to withstand AFM imaging forces despite weak individual attachments to the substrate. The images resemble previously reported AFM images of

dried *E. coli*.[218, 278-281] For example, Razatos et al.[281] show a similar lawn of *E. coli* cells. In both Razatos et al. and in Figure 67a, a majority of cells appear to have intact outer membranes, but Razatos et al. fixed their cells with glutaraldehyde, preserving the original cell shape. As we did not use any fixing agents, our cells have a flattened appearance and contain surface wrinkles and other large-scale deformations. In addition, some cells may also have been destroyed in the drying process (as evidenced by the small, thin cellular features in Figure 67a). However, the absence of fixing agents was thought to better preserve the small-scale native surface structure of the cell, an important feature when exploring the effects of the biocides.

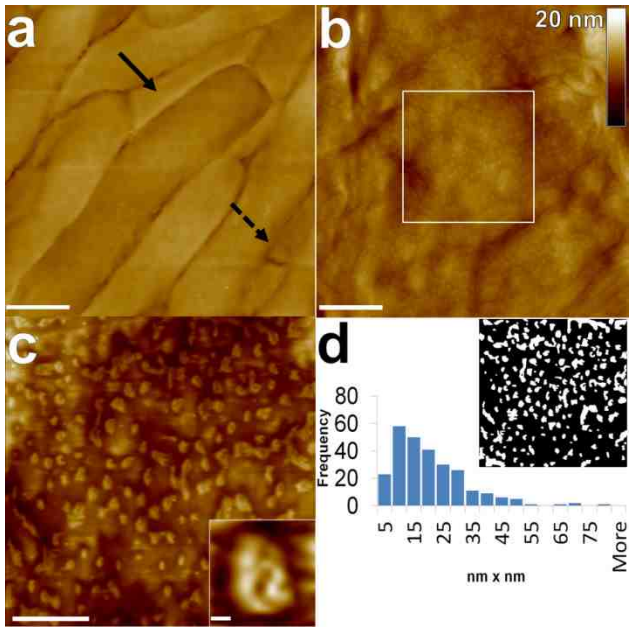

Figure 67: AFM scans of air-dried *E. coli* cells. (a) 5 µm× 5 µm continuous layer of *E. coli* cells. The scale bar is 1.0 µm. Some cells have been distorted or destroyed from the drying process (arrows). (b) 0.5 µm× 0.5 µm scan of a single *E. coli* cell surface. The scale bar is 100 nm. The white box marks the area of increased resolution shown in panel c. (c) 200 nm × 200 nm high-resolution scan of the cell surface. The scale bar is 50 nm. The bump features dominating the surface are interpreted as porins. (Inset) Software zoom of a single porin with a scale bar of 2.5 nm. (d) Histogram of the porin areas shown in panel c, with a peak area of 10 nm2. (Inset) Inverted binary image where the white areas were used to determine the porin areas.

The dried cells have an average thickness of 0.8 μm and ranged in length between 2 and 5 μm. The cells have a homogeneous appearance and are relatively free of debris. Figure 67b is a 0.5 μm × 0.5 μm AFM scan of a bacterial surface from a sample similar to the one shown in Figure 2a. The image shows a surface containing large deformations covered by small bump features. Due to their size and shape variation, the large deformations are believed to be creases caused by the drying process. The sizes and shapes of the smaller features are consistent with porin protein channels on the *E. coli* outer membrane surface. These features are better seen in Figure 67c, which is a 200 nm × 200 nm scan of a part of the same region shown in Figure 67b. The bump features dominating Figure 67c are fairly regularly spaced across the image and in many cases appear to contain holes in their centers, consistent with porin molecules.[207, 282-284] This interpretation is further supported by the histogram of the nominal porin areas shown in Figure 67d, which has a peak at about 10 nm2. In very high resolution AFM images of 2D crystals of the outer membrane porin OmpG,[282] the average diameter at the highest ridge around the porin channel is about 3.2 nm, giving an area of 8.0 nm^2, consistent with the approximate size found here.

8.3.2 Air Images: Cells and Biocides

Figure 68a shows a 10 μm× 10 μm image of *E. coli* cells which were dried after exposure to 30 μg/mL PPE-Th for 1 h under dark conditions. These images therefore show the effects of PPE-Th without light-induced biocidal activity. In contrast to Figure 67a, many cells now appear to be physically damaged, and some parts of the image shows fields of debris. Figure 68b is a 2 μm× 2 μm image of the cells in a seemingly

debris-free area that reveals a radically different surface from the untreated cell images above. On the smallest scale the surfaces now show a roughened appearance, and on larger scales, they are marked by high "aggregate" features. These features are also seen in Figure 68c, which is a 500 nm × 500 nm scan of the same region of the exposed *E. coli* surface. Small aggregates dominate the surface. The porins and other surface features from Figure 67c are no longer visible.

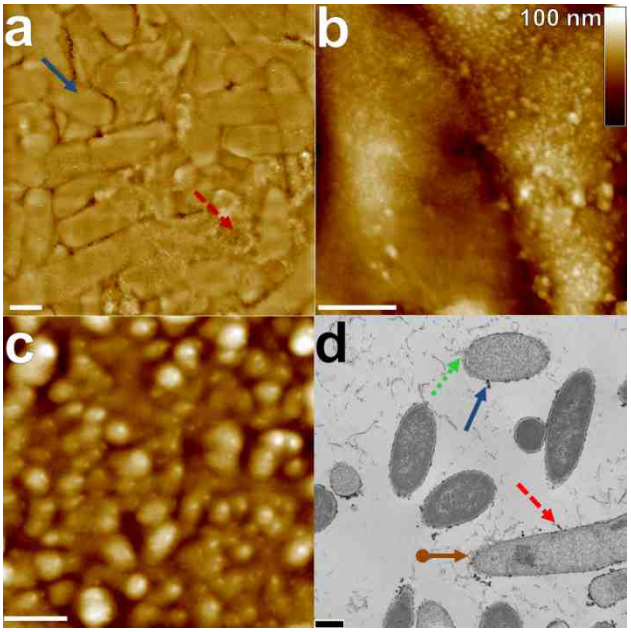

Figure 68: *E. coli* cells exposed to PPE-Th. (a) 10 μm× 10 μm continuous layer of *E. coli* cells that has been dried after dark exposure to 30 μg/mL PPE-Th for 1 h. The scale bar is 1.0 μm. Debris from cell destruction is spread across the image (red, dashed arrow), but intact *E. coli* cells are still present (blue, solid arrow). (b) 2 μm x 2μm real-time zoom of the cells in a seemingly debris-free area. The scale bar is 100 nm. (c) 500 nm × 500 nm real-time zoom of the exposed *E. coli* surface. The scale bar is 100 nm. (d) TEM image of *E. coli* cells after 1 h of dark exposure to 10 μg/mL PPE-Th. The scale bar is 500 nm. Similar to the AFM images, high-density aggregates are visible on the outer cell membrane (blue, solid arrow and red, dashed arrow). Significant disruption of the cell envelope is also visible (green, short dotted arrow, and brown, circle-line arrow).

These features can be interpreted either as a disrupted outer membrane or as a coating by the PPE-Th polymer itself (or both). It is possible to estimate whether there is enough PPE-Th in solution to coat the surfaces of the cells. We approximate a typical cell shape as a cylinder of 1.5 μm length and 0.5 μm diameter, capped by two hemispheres of

the same diameter (giving a cell with a total length 2 μm). The average area per cell is then about 2.7 μm^2. For concentrations of 10^8 cells/cm^3 and 30 μg/cm^3 PPE-Th, each cell could be coated with up to 3×10^{-7} μg of PPE-Th. The density of this coating is not known, but most organic polymer solids have densities of less than 1.2 g/mL.[285] This means that there is enough PPE-Th in solution to coat each cell to a depth of (3×10^{-13} g/1.2 g/cm^3)/2.7×10^{-8} cm^3 = 90 nm. Therefore, depending on what fraction of PPE-Th is absorbed, the features seen in Figure 68c could be pure polymer or disrupted outer cell membrane or some combination of these.

Figure 68d is a TEM image of *E. coli* cells that have been exposed in the dark to 10 μg/mL PPE-Th for 1 h under the same conditions as the above AFM images. In agreement with the conclusions of the above paragraph, the cells show obvious regions where the outer membrane is disrupted (arrows) but also regimes where the cell surface seems to be coated. Even though some cells show reduced cytoplasm in their interior (lighter cells), large debris fields are not present.

Figure 69a shows a 10 μm× 10 μm continuous layer of *E. coli* cells which were dried after exposure to 30 μg/mL EO-OPE-1(C3) for 1 h under dark conditions (no light-activated biocidal activity). As with PPE-Th, areas of debris are present (arrows), but they appear to be tighter aggregates, mostly clustered around cell borders, and cell surfaces are smooth, similar to the unexposed *E. coli* in Figure 67. Figure 69b is a 500 nm × 500 nm image of one exposed *E. coli* cell surface. On this scale the surface is generally smooth except for wrinkles due to drying and is similar in appearance to the surfaces of unexposed cells. The surface also shows small-scale features (Figure 69c), similar in size to the porins in Figure 67c. But in Figure 69c these features appear to be linear or

wormlike rather than the compact circles seen in Figure 67c. They cannot therefore be identified as intact porin channels and may represent disrupted porins or possibly aggregates of OPE molecules, lipids, and porin proteins. Figure 69d is a TEM image of *E. coli* cells after 1 h of dark exposure to 10 μg/mL EO-OPE-1(C3). Many of the EO-OPE-1(C3) exposed cells have lost their interior cytoplasm, giving them a lighter appearance. The lack of dark surface aggregates is consistent with the AFM images. The mechanism by which EO-OPE-1(C3) kills cells thus seems very different than the PPE-Th polymer. This is consistent with earlier findings.[273]

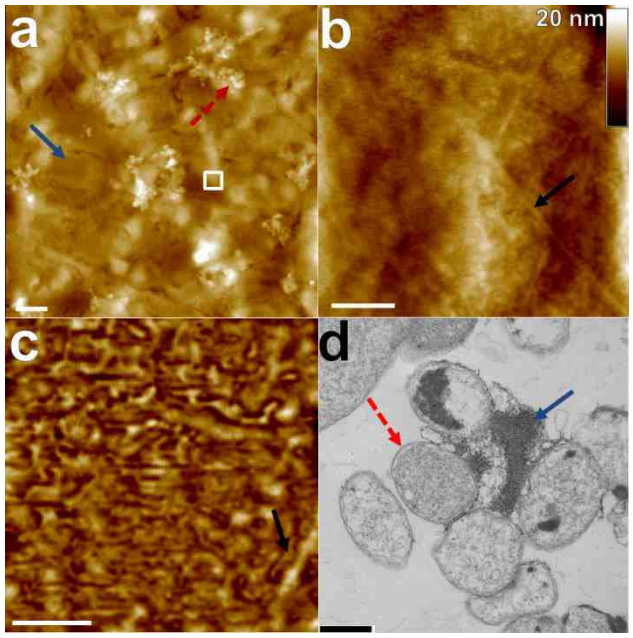

Figure 69: *E. coli* cells exposed to EO-OPE-1(C3). (a) 10 μm× 10 μm continuous layer of *E. coli* cells that has been dried after dark exposure to 30 μg/mL EO-OPE-1(C3) for 1 h. The scale bar is 1.0 μm. Intact *E. coli* are still visible (blue, solid arrow), but clumps of debris from cell destruction are clearly present (red, dashed arrow). The white box marks the area of a real-time zoom for panel b. (b) 500 nm × 500 nm scan of the cells in a seemingly debris-free area. The scale bar is 100 nm. Wrinkles from the drying process are also visible (arrow). (c) 200 nm × 200 nm software zoom of the exposed *E. coli* surface. The scale bar is 50 nm. The circular porin structures are now absent, replaced by linear, wormlike features (arrow). (d) TEM image of *E. coli* cells after 1 h of dark exposure to 10 μg/mL EO-OPE-1(C3). The scale bar is 500 nm. Amorphous materials outside the cells are observed (blue, solid arrow), but the cellar envelope does not show the clear disruption of the previous polymer case (red, dashed arrow).

8.3.3 Imaging Live Cells by AFM

Imaging live bacterial cells by AFM has often proven to be challenging. The cells usually do not adhere to glass or mica substrates strongly enough to keep them stationary under tip forces. Several different techniques have been developed to address this issue.[276] One method, developed in 1995 by Kasas and Ikai,[286] utilizes isopore polycarbonate membranes with pore sizes similar to the cell size needed to trap bacteria mechanically. Once trapped, the top portion of a cell can be imaged by AFM without risk of bacterial movement. A few groups have adopted this technique,[270, 287] or employed close variants,[276] for imaging spherical cells. Another approach uses treated surfaces to immobilize cells, such as glass treated with poly(ethyleneimide),[272] glass treated with poly-l-lysine,[271] or mica treated with poly-l-lysine.[288, 289] Some authors[281] used glutaraldehyde fixation to preserve cell shape.

We were able to image fields of live cells by (a) coating a cover glass with adhesion protein Cell-Tak[276] to increase cell–surface attachment and (b) allowing approximately two-thirds of the initial droplet to evaporate, thus concentrating the cells into a self-supporting packed layer. Because the evaporation process would concentrate any dissolved salts present, the cells were deposited from distilled water. Attempts to pack the surface by simply using a high cell concentration were not successful, either because the cells did not attach strongly enough or because a large number of loosely bound cells fouled the cantilever. Allowing the solution to partially evaporate provided a strongly attached, tightly packed cell layer without a large excess of loose cells. This method enables AFM imaging of cells without using fixing agents or mechanical trapping.

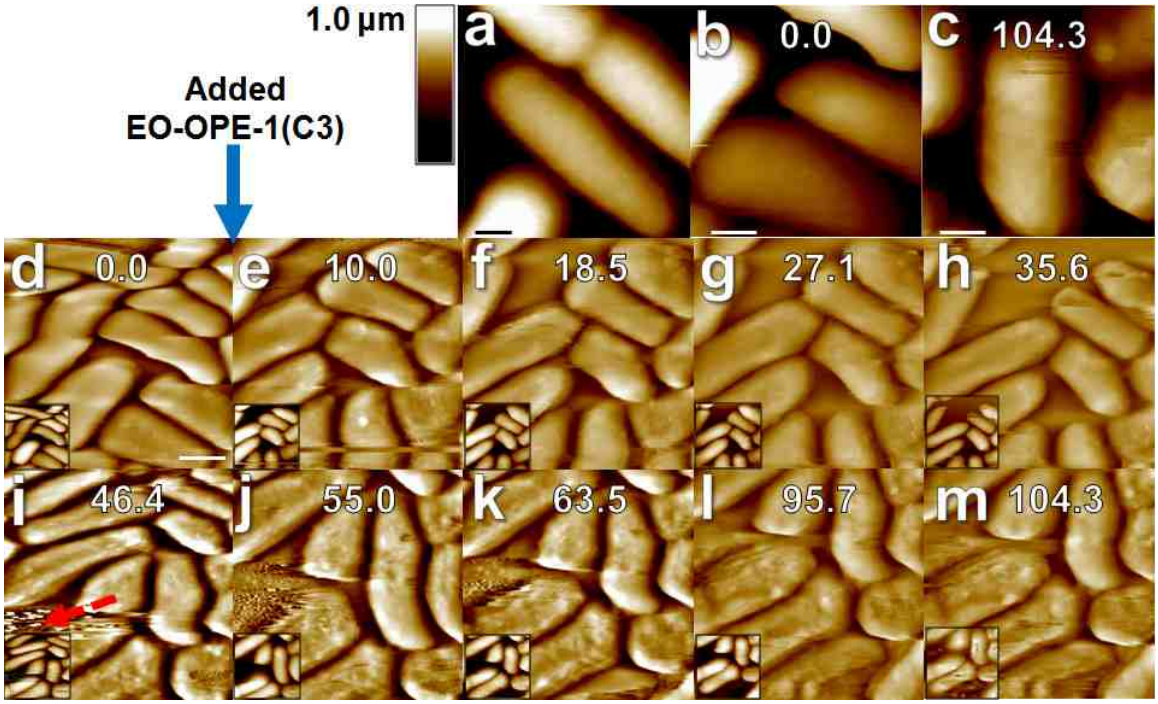

Figure 70: Underwater AFM scans of *E. coli* cells. (a) 3.2 µm × 3.2 µm AFM scan of *E. coli* cells in nanopure water. (b) A software zoom from the initial image in panel d. (c) A software zoom from the final image, panel m, 104.3 min after EO-OPE-1(C3) exposure. Scale bars for panels a–c are 500 nm. (d) Initial AFM scan before the addition of EO-OPE-1(C3). The scale bar is 1.0 µm. (e–h) Consecutive AFM scans after the addition of 30 µg/mL EO-OPE-1(C3) to the water solution surrounding the cells (blue, solid arrow). (i) The surrounding solution was refreshed with more 30 µg/mL EO-OPE-1(C3). The image disruption in the lower left corner is a result of the biocide refreshment (red, dashed arrow). This also causes a slight downward shift in the AFM scan area. The upper area of these images corresponds to the lower region of the initial scan as the AFM drifted during the experiment. (j–m) Consecutive AFM scans after the oligomer refreshment. Images (d–m) have been passed through a Gaussian filter to minimize height differences. The unprocessed image is visible in the lower left inset for images d–m. Time stamps mark the time of capture in minutes from the initial scan.

Figure 70 shows *E. coli* cells in nanopure water as 30 µg/mL EO-OPE-1(C3) is introduced into the surrounding solution. (Attempts to introduce PPE-Th solutions caused tip fouling and were not successful.) Figure 70a is a 2 µm × 2 µm AFM co ntrol image of *E. coli* cells in nanopure water alone, without biocide. The image resembles earlier published images of *E. coli* in solution,[288, 289] with visible surface features and no artifacts or debris. Figure 70b is a 500 nm × 500 nm image of an *E. coli* cell before the biocide had been added at the beginning of the experiment, and Figure 70c is a 500 nm × 500 nm

image of nearby *E. coli* cells 104.3 min after the biocide had been added, at the end of the experiment. Together, Figure 70b,c shows the increased cell surface roughness that results from exposure to 30 μg/mL EO-OPE-1(C3) in solution. Figure 70d–m shows the AFM time series over the course of that exposure. (These images have been passed through a Gaussian filter to minimize height differences.) As time progresses, cell surfaces demonstrate visible changes and increased roughness. At the 46.4 min mark, the solution within the fluid cell was refreshed with more 30 μg/mL EO-OPE-1(C3). After the solution refresh, *E. coli* show a dramatic increase in cell surface roughness, but no internal cell contents are exposed during this series.

8.3.4 Effects of Biocides in Solution

The changes to the cell morphology caused by the PPE-Th polymer resemble (at least superficially) the effects of antimicrobial peptides such as NK-2.[268, 279, 290] In both cases, aggregates of polymer and cellular material bind to the *E. coli* cell wall envelope, making the entire surface appear rougher in the AFM height images. However, the biocidal mechanism of the polymer is not a simple removal of the outer membrane. Images obtained by Amro et al.[278] show the effect on *E. coli* caused by metal depletion via EDTA, and the pattern of damage (with holes appearing on an otherwise smooth surface) clearly differs from the observed effects of the PPE-Th polymer on the cells. A proposed dark killing mechanism is illustrated in Figure 71. The polymer forms aggregates with the bacterium's outer membrane, causing damage via partial emulsification with large surface disruptions. When enough disruption of the cell surface has occurred, the cellular contents are released.[291] The EO-OPE-1(C3) oligomer does not

coat the cell surface, but changes are still apparent in the organization of proteins and, presumably, other outer-membrane components. This observation is consistent with Figure 71b, in which the EO-OPE-1(C3) oligomer is a much smaller biocide that can associate with the outer membrane, causing the reorganization of membrane components without wholesale loss of integrity.[292, 293] Using the AFM, we observed changes in *E. coli* surfaces caused by exposure to the biocides PPE-Th polymer and EO-OPE-1(C3) oligomer. Control images established that the dried *E. coli* cells can be imaged with enough resolution to identify porins on the surface. The PPE-Th polymer causes the formation of large aggregates on the surfaces of dried cells. The high aggregate density relative to the polymer concentration in solution favors a primarily PPE-Th composition. The aggregates obscure surface features such as the porins, indicating possible major disruption or even partial removal of the outer membrane. This disruption is the assumed dark killing mechanism of the PPE-Th polymer. After EO-OPE-1(C3) exposure, cellular debris is apparent but the surface remains largely intact. Porins are no longer identifiable as the surface is dominated by linear bump features, likely aggregated protein or protein-lipid-OPE complexes. This observation suggests that the mechanism for oligomer dark biocidal killing involves surface association or possible insertion of EO-OPE-1(C3) into the cell envelope. In solution, the oligomer caused the surface of *E. coli* to increase in roughness over time.

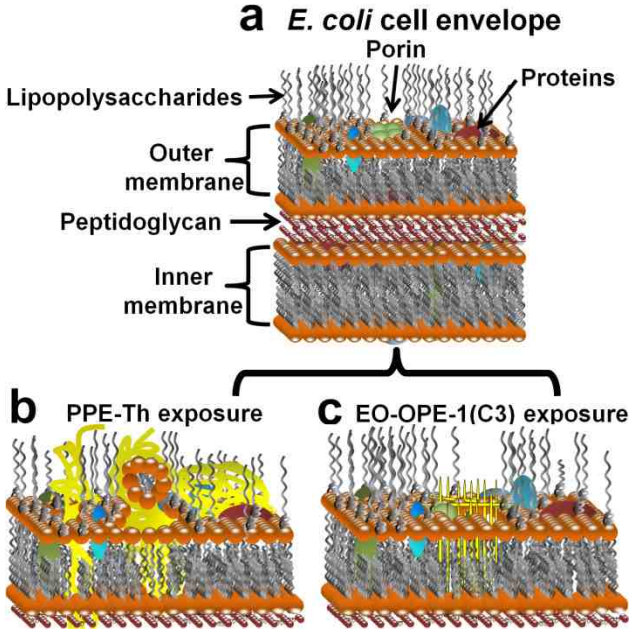

Figure 71: Hypothesized mechanism for the dark antimicrobial action of PPE-Th and EO-OPE-1(C3). (a) Structure of unexposed cell envelope with lipid bilayers (orange lipid heads with gray tails), lipopolysaccharides (gray), peptidoglycan (dark red), membrane proteins (blue, dark green, and dark red), and porins (light green). (b) The PPE-Th polymer (yellow) forms micelle-like aggregates with the outer membrane of the *E. coli* cells. The formation of these polymer aggregates disrupts the integrity of the membrane, leading to cell death. (c) The oligomer (yellow) is a much smaller molecule and can associate with, or perhaps penetrate, the outer cell membrane of *E. coli*. Instead of forming visible aggregates, the oligomer forms pores that disrupt the chemical gradient, leading to cell death.

8.4 Randomly Patterned Multifunctional Surfaces

In a complementary approach to the work done by the López group at Duke University (see Chapter 5), the Schanze lab at Florida State University fabricated surfaces with random patterns of poly(N-isopropylacrylamide) (PNIPAAm) and PPE bilayers. These mixed surfaces utilized the above mentioned ATRP to grow PNIPAAm from the glass surfaces (see Chapter 5). These samples also contained varying depths of physisorped PPE layers. The order of PPE deposition vs PNIPAm deposition varied depending on the sample. For one type of surface, a 3-layer PPE film was deposited on cover glass where the layers were (from bottom to top) PPE-DABCO, PPE-SO3, and

PPE-DABCO. PNIPAAm was grown after the PPE deposition to create a randomly ordered mixed surface.[294]

8.4.1 AFM Results

AFM surface characterization was performed on the random mixed surfaces. Figure 72 shows 5 μm by 5 μm images of a 3-layer PPE film and PNIPAAm surface, along with two control surfaces. Figure 72a shows a film formed from layers of PPE-DABCO, PPE-SO_3, and PPE-DABCO in that order. Total film thickness is estimated to be about 5 nm as measured by AFM scratching. Ideally, the top surface of the control is positively-charged PPE-DABCO but AFM images suggest the polymer is not a continuous layer but sometimes contains small "holes" that expose deeper PPE layers or the glass substrate. Almost all deposited PPEs appear as small spheres or "granules" in AFM images of sufficient resolution. In contrast, surface polymerized PNIPAAm (Figure 72b) has a very smooth appearance and lacks the granule signature of the PPE layers. Figure 72c shows the results of graphing PNIPAAm onto a 3-layer PPE film. A unique pattern is created where "plumes" of relatively high material exist on top of the distinct PPE granular pattern. These plumes are interpreted to be PNIPAAm that was grown from the glass slide via small holes, or seed sites, in the PPE layer coverage. During the polymerization process, the polymer was first linked to the glass using silane chemistry and then thoroughly rinsed. Therefore, PNIPAAm should only appear in the mixed surfaces at sites where the glass was exposed. While sizes of these plumes vary, their coverage appears roughly uniform at the bacterial scale (~2 μm by 2 μm). Figure 73

shows a model for the mixed surface. Figure 73c highlights the plume nature of the PNIPAAm as it is polymerized from the glass substrate.

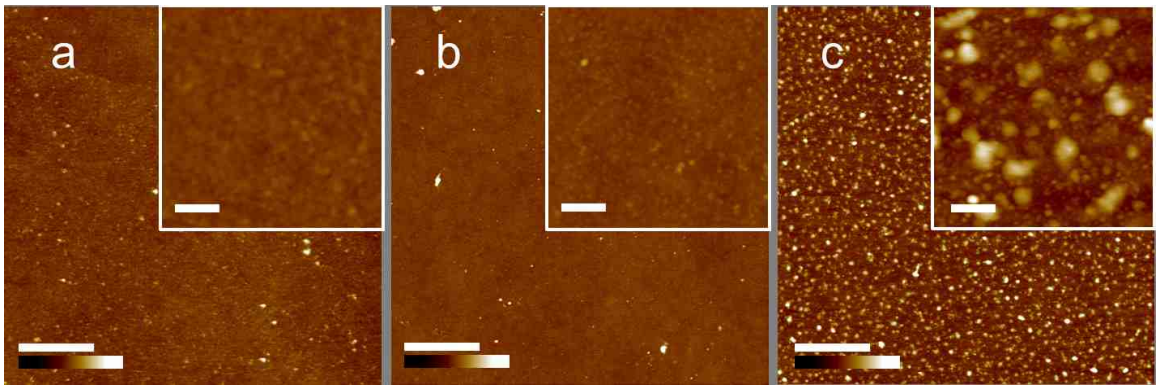

Figure 72: AFM tapping mode height images of the mixed surfaces. (a) A 3-layer film formed from a bottom layer of PPE-DABCO, a middle layer of PPE-SO_3, and a top layer of PPE-DABCO. (b) Surface-polymerized film of PNIPAAm only. (c) Full mixed surface of PNIPAAm deposited after the 3-layer PPE deposition described in (a). Height scale is 25 nm. The main images are 5 μm by 5 μm (scale bar 1 μm). The inset images are 500 nm by 500 nm (scale bar 100 nm).

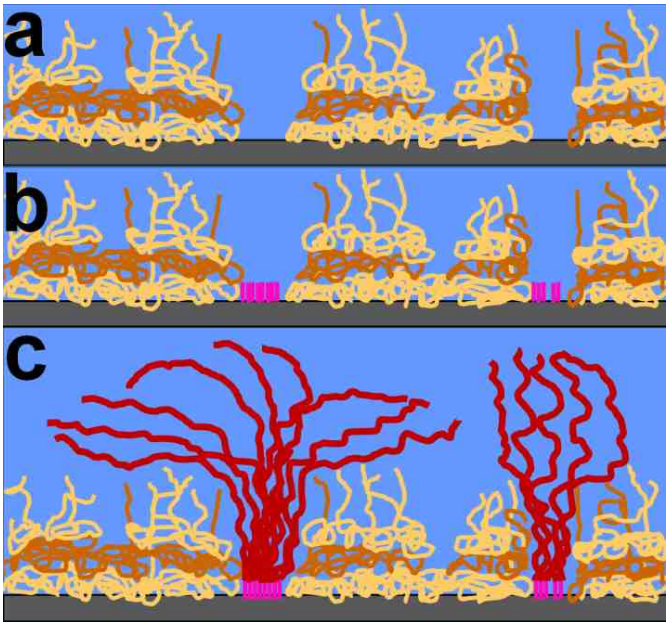

Figure 73: Structure of the random mixed PPE and PNIPAAm surfaces. (a) Layer-by-layer film formed from PPE-DABCO (light brown) and PPE-SO3 (orange) on a glass surface (gray). (b) Three-layer PPE surface with polymerization initiators (pink) attached to the glass substrate via gaps in the PPE coverage. (c) PNIPAAm (red) polymerized from the initiators. The PNIPAAm extends beyond the PPE layers to create the plumes and surface coverage observed in the AFM images.

The PNIPAAm in the random mixed samples can also cover a much larger fraction of the surface area. Figure 74a shows a 5 μm by 5 μm image of another 3-layer PPE-only film. This surface was made using the same procedure as Figure 72a, but here the image focuses on a circular bubble in the PPE film. In this bubble, the single upper PPE-DABCO layer seems to be absent, exposing the lower PPE-SO3 layer. (A height difference of ~2 nm is consistent with only one PPE layer.) Similar irregularities are also present in the mixed sample (Figure 74b), but in this case the bubble areas have clearly been partially filled in. In and around these areas, the PNIPAAm addition is very apparent, but the polymer covers a much larger proportion of the surface. This more extensive PNIPAAm coverage could be a result of increased seed sites where PPE coverage is reduced. More available sites for PNIPAAm attachment may not force the polymer into the plume arrangement observed elsewhere.

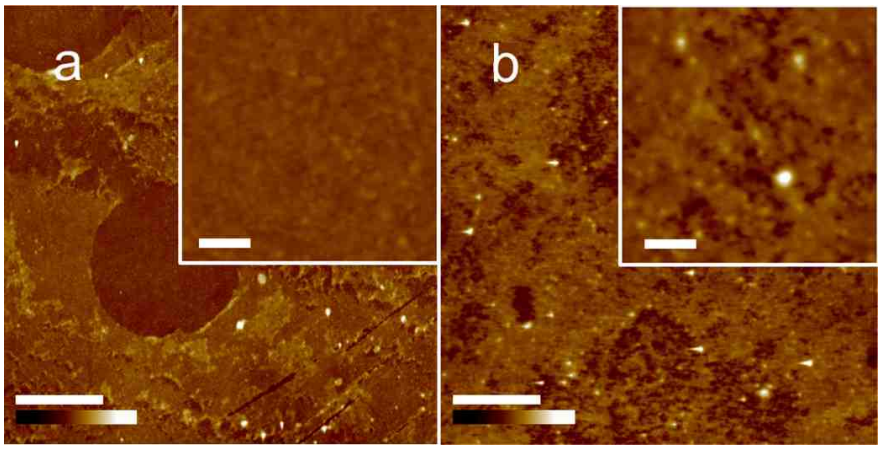

Figure 74: AFM tapping mode height images of the mixed surfaces: (a) LbL PPE film formed from a bottom layer of PPE-DABCO, a middle layer of PPE-SO_3, and a top layer of PPE-DABCO. (b) Surface-polymerized film of PNIPAAm alone. (c) Full mixed surface of PNIPAAm deposited after the 3-layer PPE deposition. Height scale color bars are 25 nm. The main images are 5 μm by 5 μm (scale bar 1 μm). The inset images are 500 nm by 500 nm (scale bar 100 nm).

8.4.2 Testing for Release and Cell Killing

Bacterial release studies on this random mixed surface were done with both *E. coli* and *S. aureus* and followed a similar procedure to the nanopatterned surfaces in Chapter 5. Bacteria were exposed to the random mixed surface at 37 °C for 2 h (in buffer) before being rinsed with cold water. Prior to the rinse, the mixed surface showed increased attachment density compared to blank glass (~56% increase for *E. coli* and ~80% for *S. aureus*) and compared to unpatterned PNIPAAm surfaces (~40% increase for *E. coli* and ~80% for *S. aureus*). After the cold rinse, nearly 80% of both *E. coli* and *S. aureus* were released, in relatively good agreement with the release rates from the mixed patterened surfaced tested by the Lopez group.[294] A water rinse above the LCST for PNIPAAm did not cause a noticeable release of bacteria presumably because it did not cause a change in hydrophobicity.

Approximately 65% of the surface bound *E. coli* cells and 62% of the surface bound *S. aureus* cells (with an initial concentration of 10^5 cells/mL) were inactivated after exposure to 420 nm light for 1 hr (see Figure 75 and Figure 76). In contrast, the same surfaces left in the dark only caused a 10% killing of either *E. coli* or *S. aureus* cells. On the surface with only PPE and no PNIPAAm, the inactivation ratios were similar.

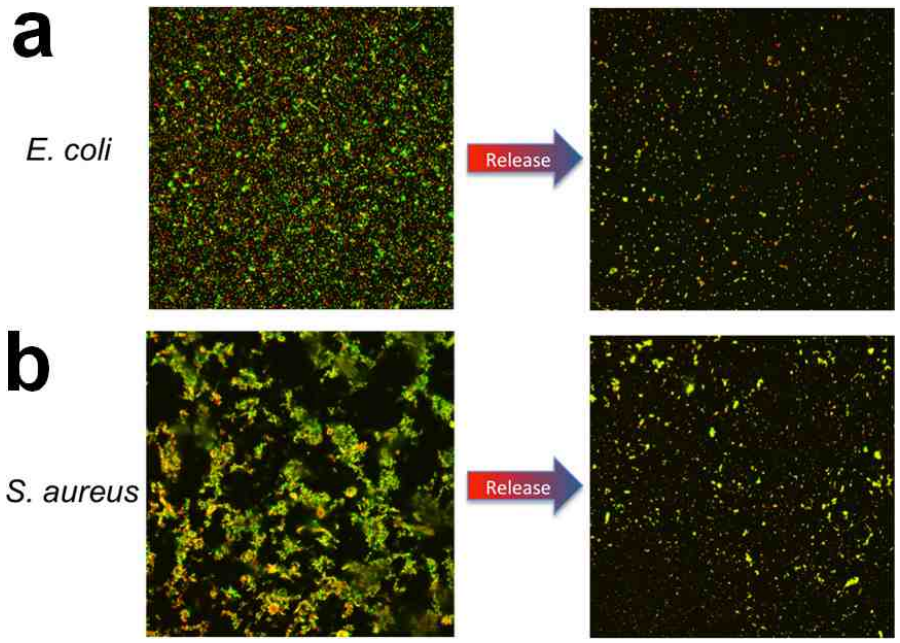

Figure 75: Confocal Microscopy images showing the inactivation and release of (a) *E. coli* and (b) *S. aureus* bacteria for a surface with a 3-layer film of PPE-DABCO, PPE-SO_3, and PPE-DABCO followed by grafted PNIPAAm. Bacteria were exposed to 420 nm near-visible light in a photoreactor for 1 hr at 37°C and rinsed with 4C water. The green stain (SYTO) shows living cells while the red stain (Propidium iodide) shows inactivated cells (with yellow representing dying cells).[294]

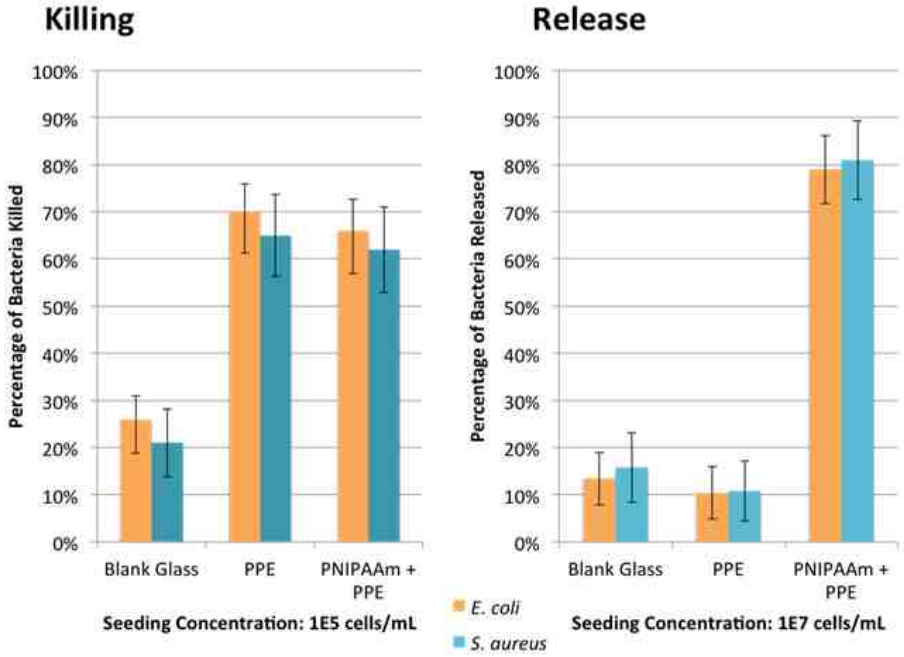

Figure 76: Bacterial killing and release percentages for the random mixed surfaces (a) Killing percentages after one hour exposure to light comparing the blank and PPE controls to the mixed surface after . (b) Release percentages comparing the blank and PPE controls to the mixed surface.[294]

8.4.3 Mixed Surface Model

As the AFM images show, there are areas of PNIPAAm coverage randomly distributed between areas where the characteristic granular PPE structure is visible. While the sizes of these areas vary, a typical size of either a PPE area or a PNIPAAm area is approximately 25 to 50 nm. Figure 77 below shows the bacterial surface and a rough model of the mixed surface approximately to scale. The bacterium is assumed to be a 2 μm by 500 nm lozenge that comes into contact with multiple PNIPAAm plumes (varying in length from 60 nm to 20 nm) and exposed PPE regions. Release studies show that this degree of coverage by PNIPAAm is enough to facilitate cell release at low temperatures. As live/dead assays confirm, the random mixed surfaces exhibit good killing of *E. coli* and *S. aureus*. Therefore, there is also enough PPE to facilitate cellular disruption. More specifically, the addition of PNIPAAm does not greatly reduce the biocidal efficacy of the surface, even though, as AFM images show, in some cases PNIPAAm covers large a percentage of the surface. This suggests the possibility that the PPE layers are able to disrupt bacterial cells even when not in direct contact with their surfaces. If so, the generation of singlet oxygen (as described in Chapter 5) may be the dominant biocidal mechanism when the PEs are exposed to light (versus the disruption seen in the dark). This is consistent with the results above where it was found that one hour of light exposure resulted in a high degree of inactivation, but one hour in the dark resulted in little inactivation.

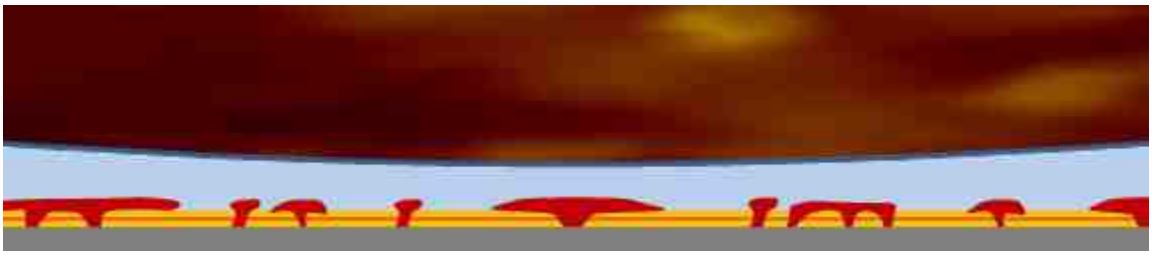

Figure 77: Large-scale structure of the random mixed PPE and PNIPAAm surface. Three layers of the PPE film are PPE-DABCO (light brown) and PPE-SO3 (orange) on a glass surface (gray). The PNIPAAm (red) extends beyond the PPE layers to create islands of coverage. An incoming bacterium (brown) will be exposed to multiple PNIPAAm islands along with the PPE film.

8.5 Conclusions

The many experiments detailed above show the disruptive effects of the PE biocides. The PEs have a dramatic direct effect on supported lipid bilayers, acting in a similar manor as surfactants. Disruption of the lipid membranes is also observed when *E. coli* cells are exposed to the biocides in solution. However, the mechanisms of inactivation of bacterial cells in the dark is different for PPEs and OPEs and is also different from other surfactants. The polymer forms aggregates with the cell's outer membrane while the smaller oligomer disrupts surface protein organization. Real –time solution AFM imaging confirms this disruption. In the presence of light, the killing mechanism was also explored with the randomly mixed PPE and PNIPAAm surfaces. The AFM images show these surfaces are characterized by mixed areas of the biocide and the non-biocidal PNIPAAm (limiting the area of direct contact between the PPEs and the cell). While such multifunctional mixed surfaces exhibit good levels of bacterial inactivation when exposed to light, much less inactivation is observed in the dark. This supports the theory that the killing mechanism for the surface bound PEs is likely due mainly to singlet oxygen formation and so depends less on direct contact between the cellular surface and the PE.

These experimental results can also help improve future PWA Simulator and PWA Initiator models. AFM images of the *E. coli* surface provide an accurate view of the composition and distribution of materials. Experimental measurements of bound cell surface concentrations can be modeled by PWA Simulator and PWA Integrator once the correct input parameters (such as surface tension values) are found. This feedback to the PWA programs could in turn increase the predictive accuracy of these models and provide direction for better optimization of the biocides and biocidal surfaces.

9. REFERENCES CITED

1. The nobel prize in chemistry 2013 - advanced information. http://www.nobelprize.org/nobel_prizes/chemistry/laureates/2013/advanced.html (Dec. 3, **2014**),

2. Schlick, T., *Molecular modeling and simulation: An interdisciplinary guide*. Springer-Verlag New York, Inc.: **2002**; p 656.

3. Schlick, T., The 2013 nobel prize in chemistry celebrates computations in chemistry and biology. *SIAM News* **2013,** 46, (10).

4. Lifson, S.; Warshel, A., Consistent force field for calculations of conformations, vibrational spectra, and enthalpies of cycloalkane and n-alkane molecules. *J. Chem. Phys.* **1968,** 49, (11), 5116-5129.

5. Levitt, M., The birth of computational structural biology. *Nat. Struct. Biol.* **2001,** 8, (5), 392-3.

6. Levitt, M.; Lifson, S., Refinement of protein conformations using a macromolecular energy minimization procedure. *J. Mol. Biol.* **1969,** 46, (2), 269-279.

7. Warshel, A.; Karplus, M., Calculation of ground and excited state potential surfaces of conjugated molecules. I. Formulation and parametrization. *J. Am. Chem. Soc.* **1972,** 94, (16), 5612-5625.

8. Levitt, M.; Warshel, A., Computer simulation of protein folding. *Nature* **1975,** 253, (5494), 694-698.

9. Warshel, A.; Levitt, M., Theoretical studies of enzymic reactions: Dielectric, electrostatic and steric stabilization of the carbonium ion in the reaction of lysozyme. *J. Mol. Biol.* **1976,** 103, (2), 227-249.

10. McCammon, J. A.; Gelin, B. R.; Karplus, M., Dynamics of folded proteins. *Nature* **1977,** 267, (5612), 585-590.

11. Bahar, I.; Rader, A. J., Coarse-grained normal mode analysis in structural biology. *Curr. Opin. Struct. Biol.* **2005,** 15, (5), 586-592.

12. Balaeff, A.; Koudella, C. R.; Mahadevan, L.; Schulten, K., Modelling DNA loops using continuum and statistical mechanics. *Phil. Trans. R. Soc. Lond* **2004,** 362, 1355–1371.

13. Bojin, M. D.; Schlick, T., A quantum mechanical investigation of possible mechanisms for the nucleotidyl transfer reaction catalyzed by DNA polymerase β. *J. Phys. Chem. B* **2007,** 111, (38), 11244-11252.

14. Cheatham, T. E., III; Miller, J. L.; Fox, T.; Darden, T. A.; Kollman, P. A., Molecular dynamics simulations on solvated biomolecular systems: The particle mesh ewald method leads to stable trajectories of DNA, rna, and proteins. *J. Am. Chem. Soc.* **1995,** 117, (14), 4193-4194.

15. Cuesta-López, S.; Errami, J.; Falo, F.; Peyrard, M., Can we model DNA at the mesoscale? *J. Biol. Phys.* **2005,** 31, 273–301.

16. Ding, F.; Sharma, S.; Chalasani, P.; Demidov, V. V.; Broude, N. E.; Dokholyan, N. V., Ab initio rna folding by discrete molecular dynamics: From structure prediction to folding mechanisms. *RNA* **2008,** 14, (6), 1164-1173.

17. Graham, M. D., Fluid dynamics of dissolved polymer molecules in confined geometries. *Annu. Rev. Fluid Mech.* **2011,** 43, (1), 273-298.

18. Han, W.; Wan, C.-K.; Wu, Y.-D., Toward a coarse-grained protein model coupled with a coarse-grained solvent model: Solvation free energies of amino acid side chains. *J. Chem. Theory Comput.* **2008,** 4, (11), 1891-1901.

19. Hirshberg, M.; Levitt, M., Simulating the dynamics of the DNA double helix in solution. In *Dynamics and the problem of recognition in biological macromolecules*, Springer US: **1996**; Vol. 288, pp 173-191.

20. Jorgensen, W. L.; Chandrasekhar, J.; Madura, J. D.; Impey, R. W.; Klein, M. L., Comparison of simple potential functions for simulating liquid water. *J. Chem. Phys.* **1983,** 79, (2), 926-935.

21. Knotts IV, T. A.; Rathore, N.; Schwartz, D. C.; de Pablo, J. J., A coarse grain model for DNA. *J. Chem. Phys.* **2007,** 126.

22. Lyman, E.; Pfaendtner, J.; Voth, G. A., Systematic multiscale parameterization of heterogeneous elastic network models of proteins. *Biophys. J.* **2008,** 95, (9), 4183-4192.

23. Noid, W. G.; Chu, J.-W.; Ayton, G. S.; Krishna, V.; Izvekov, S.; Voth, G. A.; Das, A.; Andersen, H. C., The multiscale coarse-graining method. I. A rigorous bridge between atomistic and coarse-grained models. *J. Chem. Phys.* **2008,** 128, (24), -.

24. Phillips, J. C.; Braun, R.; Wang, W.; Gumbart, J.; Tajkhorshid, E.; Villa, E.; Chipot, C.; Skeel, R. D.; Kalé, L.; Schulten, K., Scalable molecular dynamics with namd. *J. Comput. Chem.* **2005,** 26, (16), 1781-1802.

25. Vologodskii, A., Brownian dynamics simulation of knot diffusion along a stretched DNA molecule. *Biophys. J.* **2006,** 90, (5), 1594-1597.

26. Wang, W.; Donini, O.; Reyes, C. M.; Kollman, P. A., Biomolecular simulations: Recent developments in force fields, simulations of enzyme catalysis, protein-ligand, protein-protein, and protein-nucleic acid noncovalent interactions. *Annu. Rev. Biophys. Biomol. Struct.* **2001,** 30, (1), 211-243.

27. Dror, R. O.; Dirks, R. M.; Grossman, J. P.; Xu, H.; Shaw, D. E., Biomolecular simulation: A computational microscope for molecular biology. *Annu. Rev. Biophys.* **2012,** 41, (1), 429-452.

28. Brooks, B. R.; Brooks, C. L.; Mackerell, A. D.; Nilsson, L.; Petrella, R. J.; Roux, B.; Won, Y.; Archontis, G.; Bartels, C.; Boresch, S.; et_al., Charmm: The biomolecular simulation program. *J. Comput. Chem.* **2009,** 30, (10), 1545-1614.

29. Case, D. A.; Babin, V.; Berryman, J. T.; Betz, R. M.; Cai, Q.; Cerutti, D. S.; Cheatham III, T. E.; Darden, T. A.; Duke, R. E.; Gohlke, H.; et_al. *Amber 14*, UCSF: San Francisco, C.A., **2014**.

30. Lindahl, E.; Hess, B.; van der Spoel, D., Gromacs 3.0: A package for molecular simulation and trajectory analysis. *J Mol Model* **2001,** 7, (8), 306-317.

31. Phillips, J. C.; Braun, R.; Wang, W.; Gumbart, J.; Tajkhorshid, E.; Villa, E.; Chipot, C.; Skeel, R. D.; Kalé, L.; Schulten, K., *Namd*. 2.7 b1 ed.; Theoretical Biophysics Group: University of Illinois and Beckman Institute, Urbana, IL, **2009**.

32. Voth, G. A., Introduction: Coarse-graining in molecular modeling and simulation. *J. Comput. Chem.* **2006,** 2, 463.

33. Shaw, D., E.; Deneroff, M., M. ; Dror, R., O.; Kuskin, J., S.; Larson, R., H.; Salmon, J., K.; Young, C.; Batson, B.; Bowers, K., J.; Chao, J., C.; _al., e., Anton, a special-purpose machine for molecular dynamics simulation. *Commun. ACM* **2008,** 51, (7), 91-97.

34. Shaw, D., E.; Dror, R., O.; Salmon, J., K.; Grossman, J. P.; Mackenzie, K., M.; Bank, J., A.; Young, C.; Deneroff, M., M.; Batson, B.; Bowers, K., J.; et_al., Millisecond-scale molecular dynamics simulations on anton. In *Proceedings of the Conference on High Performance Computing Networking, Storage and Analysis*, ACM: Portland, Oregon, **2009**.

35. Basdevant, N.; Borgis, D.; Ha-Duong, T., A coarse-grained protein-protein potential derived from an all-atom force field. *J. Phys. Chem. B* **2007,** 111, 9390-9399.

36. Bond, P. J.; Sansom, M. S. P., Insertion and assembly of membrane proteins via simulation. *J. Am. Chem. Soc.* **2006,** 128, (8), 2697-2704.

37. Cadoni, M.; De Leo, R.; Gaeta, G., Composite model for DNA torsion dynamics. *Phys. Rev. E* **2007,** 75.

38. Chen, Y. L.; Graham, M. D.; de Pablo, J. J.; Randall, G. C.; Gupta, M.; Doyle, P. S., Conformation and dynamics of single DNA molecules in parallel-plate slit microchannels. *Phys. Rev. E* **2004,** 70, (6), 4.

39. Cuesta-López, S.; Peyrard, M.; Graham, D. J., Model for DNA hairpin denaturation. *Eur. Phys. J. E* **2005,** 16, 235-246.

40. Dans, P. D.; Zeida, A.; Machado, M. a. R.; Pantano, S., A coarse grained model for atomic-detailed DNA simulations with explicit electrostatics. *J. Chem. Theory Comput.* **2010,** 6, (5), 1711-1725.

41. de Pablo, J. J., Coarse-grained simulations of macromolecules: From DNA to nanocomposites. *Annu. Rev. Phys. Chem.* **2011,** 62, (1), 555-574.

42. Drukker, K.; Schatz, G. C., A model for simulating dynamics of DNA denaturation. *J. Phys. Chem. B* **2000,** 104, (26), 6108-6111.

43. Gaeta, G., Solitons in the yakushevich model of DNA beyond the contact approximation. *Phys. Rev. E* **2006,** 74.

44. Graham, R. S.; Larson, R. G., Coarse-grained brownian dynamics simulations of electrophoresis of DNA molecules from generalized reptation models. *Macromolecules* **2007,** 40, 366-378.

45. Huertas, M. L.; Navarro, S.; Lopez Martinez, M. C.; Garcia de la Torre, J., Simulation of the conformation and dynamics of a double-helical model for DNA. *Biophys. J.* **1997,** 73, 3142-3153.

46. Izvekov, S.; Swanson, J. M. J.; Voth, G. A., Coarse-graining in interaction space: A systematic approach for replacing long-range electrostatics with short-range potentials. *J. Phys. Chem. B* **2008,** 112, (15), 4711-4724.

47. Izvekov, S.; Voth, G. A., A multiscale coarse-graining method for biomolecular systems. *J. Phys. Chem. B* **2005** 109, 2469-2473.

48. Jonikas, M. A.; Radmer, R. J.; Laederach, A.; Das, R.; Pearlman, S.; Herschlag, D.; Altman, R. B., Coarse-grained modeling of large rna molecules with knowledge-based potentials and structural filters. *RNA* **2009,** 15, (2), 189-199.

49. Linak, M. C.; Tourdot, R.; Dorfman, K. D., Moving beyond watson--crick models of coarse grained DNA dynamics. *J. Chem. Phys.* **2011,** 135, (20), 205102-12.

50. Marrink, S. J.; de Vries, A. H.; Mark, A. E., Coarse grained model for semiquantitative lipid simulations. *J. Phys. Chem. B* **2003,** 108, (2), 750-760.

51. Mergell, B.; Ejtehadi, M. R.; Everaers, R., Modeling DNA structure, elasticity, and deformations at the base-pair level. *Phys. Rev. E* **2003,** 68.

52. Morriss-Andrews, A.; Rottler, J.; Plotkin, S. S., A systematically coarse-grained model for DNA and its predictions for persistence length, stacking, twist, and chirality. *J. Chem. Phys.* **2010,** 132, (3), 035105-18.

53. Ouldridge, T. E.; Louis, A. A.; Doye, J. P. K., Structural, mechanical, and thermodynamic properties of a coarse-grained DNA model. *J. Chem. Phys.* **2011,** 134, (8), 085101-22.

54. Peyrard, M., Nonlinear dynamics and statistical physics of DNA. *Nonlinearity* **2004,** 17, (2), R1.

55. Peyrard, M.; Cuesta-López, S.; James, G., Modelling DNA at the mesoscale: A challenge for nonlinear science? *Nonlinearity* **2008,** 21.

56. Poulain, P.; Saladin, A.; Hartmann, B.; Prévost, C., Insights on protein-DNA recognition by coarse grain modelling. *J. Comput. Chem.* **2008,** 0.

57. Reith, D.; Meyer, H.; Müller-Plathe, F., Mapping atomistic to coarse-grained polymer models using automatic simplex optimization to fit structural properties. *Macromolecules* **2001,** 34, 2335-2345.

58. Reith, D.; Pütz, M.; Müller-Plathe, F., Deriving effective mesoscale potentials from atomistic simulations. *J. Comput. Chem.* **2003,** 24, (13), 1624–1636.

59. Sambriski, E. J.; Schwartz, D. C.; de Pablo, J. J., A mesoscale model of DNA and its renaturation. **2009,** 96, (5), 1675-1690.

60. Sayar, M.; Avşaroğlu, B.; Kabakçıoğlu, A., Twist-writhe partitioning in a coarse-grained DNA minicircle model. *Phys. Rev. E* **2010,** 81, (4), 041916.

61. Srinivas, G.; Shelley, J. C.; Nielsen, S. O.; Discher, D. E.; Klein, M. L., Simulation of diblock copolymer self-assembly, using a coarse-grain model. *J. Phys. Chem. B* **2004,** 108, (24), 8153-8160.

62. Steve, O. N.; Carlos, F. L.; Goundla, S.; Michael, L. K., Coarse grain models and the computer simulation of soft materials. *J. Phys.: Condens. Matter* **2004,** 16, (15), R481.

63. Stoneham, A. M.; Harding, J. H., Not too big, not too small: The appropriate scale. *Nature* **2003,** 2.

64. Tepper, H. L.; Voth, G. A., A coarse-grained model for double-helix molecules in solution: Spontaneous helix formation and equilibrium properties. *J. Chem. Phys.* **2005,** 122.

65. Tozzini, V.; Rocchia, W.; McCammon, J. A., Mapping all-atom models onto one-bead coarse-grained models: General properties and applications to a minimal polypeptide model. *J. Chem. Theory Comput.* **2006,** 2, 667-673.

66. Venturoli, M.; Maddalena Sperotto, M.; Kranenburg, M.; Smit, B., Mesoscopic models of biological membranes. *Phys. Rep.* **2006,** 437, (1-2), 1-54.

67. Voltz, K.; Trylska, J.; Tozzini, V.; Kurkal-Siebert, V.; Langowski, J.; Smith, J., Coarse-grained force field for the nucleosome from self-consistent multiscaling. *J. Comput. Chem.* **2008,** 29, (9), 1429–1439.

68. Xia, Z.; Gardner, D. P.; Gutell, R. R.; Ren, P., Coarse-grained model for simulation of rna three-dimensional structures. *J. Phys. Chem. B* **2010,** 114, (42), 13497-13506.

69. Zacharias, M., Protein-protein docking with a reduced protein model accounting for side-chain flexibility. *Prot. Sci.* **2003,** 12, (6), 1271-1282.

70. Zacharias, M., Attraact: Protein-protein docking in capri using a reduced protein model. *Proteins: Struct., Funct., Bioinf.* **2005,** 60, (2), 252-256.

71. Zhang, F.; Collins, M. A., Model simulations of DNA dynamics. *Phys. Rev. E* **1995,** 52, (4), 4217-4224.

72. Lazaridis, T.; Karplus, M., Effective energy function for proteins in solution. In *Proteins: Struct. Funct. Genet.*, Wiley-Liss, Inc.: **1999**; Vol. 35, pp 133-152.

73. Lu, M.; Poon, B.; Ma, J., A new method for coarse-grained elastic normal-mode analysis. *J. Chem. Theory Comput.* **2006,** 2, 464-471.

74. Zheng, W.; Doniach, S., A comparative study of motor-protein motions by using a simple elastic-network model. *Proc. Natl. Acad. Sci.* **2003,** 100, (23), 13253–13258.

75. Ermak, D. L.; McCammon, J. A., Brownian dynamics with hydrodynamic interactions. *J. Chem. Phys.* **1978,** 69, (4), 1352-1360.

76. Beard, D. A.; Schlick, T., Inertial stochastic dynamics. Ii. Influence of inertia on slow kinetic processes of supercoiled DNA. *J. Chem. Phys.* **2000,** 112, (17), 7323-7338.

77. Sottas, P.-E.; Larquet, E.; Stasiak, A.; Dubochet, J., Brownian dynamics simulation of DNA condensation. *Biophys. J.* **1999,** 77, (4), 1858-1870.

78. van Kampen, N. G., *Stochastic processes in physics and chemistry*. Elsevier: Amsterdam, The Netherlands, **1992**.

79. Sugita, Y.; Okamoto, Y., Replica-exchange molecular dynamics method for protein folding. *Chem. Phys. Lett.* **1999,** 314, (1-2), 141-151.

80. Isard, B. P. C. Theory and practice in replica-exchange molecular dynamics simulation. Dissertation, Duke University, **2008**.

81. Sugita, Y.; Kitao, A.; Okamoto, Y., Multidimensional replica-exchange method for free-energy calculations. *J. Chem. Phys.* **2000,** 113.

82. Sugita, Y.; Okamoto, Y., Replica-exchange multicanonical algorithm and multicanonical replica-exchange method for simulating systems with rough energy landscape. *Chem. Phys. Lett.* **2000**.

83. Ishikawa, Y.; Sugita, Y.; Nishikawa, T.; Okamoto, Y., Ab initio replica-exchange monte carlo method for cluster studies. *Chem. Phys. Lett.* **2001,** 333, (1-2), 199-206.

84. Kumar, S.; Bouzida, D.; Swendsen, R. H.; Kollman, P. A.; Rosenberg, J. M., The weighted histogram analysis method for free energy calculations on biomolecules. *J. Comput. Chem.* **1992,** 13, 1011.

85. Yakovchuk, P.; Protozanova, E.; Frank-Kamenetskii, M. D., Base-stacking and base-pairing contributions into thermal stability of the DNA double helix. *Nuc. Acids Res.* **2006,** 34, (2), 564-574.

86. Friedman, R. A.; Honig, B., A free energy analysis of nucleic acid base stacking in aqueous solution. *Biophys. J.* **1995,** 69, 1528-1535.

87. Olson, W. K.; Bansal, M.; Burley, S. K.; Dickerson, R. E.; Gerstein, M.; Harvey, S. C.; Heinemann, U.; Lu, X.-J.; Neidle, S.; Shakked, Z.; et_al., A standard reference frame for the description of nucleic acid base-pair geometry. *J. Mol. Biol.* **2001,** 313, (1), 229-237.

88. Babcock, M. S.; Pednault, E. P. D.; Olson, W. K., Nucleic acid structure analysis : Mathematics for local cartesian and helical structure parameters that are truly comparable between structures. *J. Mol. Biol.* **1994,** 237, (1), 125-156.

89. Šponer, J.; Gabb, H. A.; Leszczynski, J.; Hobza, P., Base-base and deoxyribose-base stacking interactions in b-DNA and z-DNA: A quantum-chemical study. *Biophys. J.* **1997,** 73, 76-87.

90. Ogawa, T.; Kurita, N.; Sekino, H.; Kitao, O.; Tanaka, S., Hydrogen bonding of DNA base pairs by consistent charge equilibration method combined with universal force field. *Chem. Phys. Lett.* **2003,** 374, (3-4), 271-278.

91. Gould, I. R.; Kollman, P. A., Theoretical investigation of the hydrogen bond strengths in guanine-cytosine and adenine-thymine base pairs. *J. Am. Chem. Soc.* **1994,** 116, (6), 2493-2499.

92. Smith, S. B.; Cui, Y.; Bustamante, C., Overstretching b-DNA: The elastic response of individual double-stranded and single-stranded DNA molecules. *Science* **1996,** 271, 795-799.

93. Zhang, Y.; Zhou, H.; Ou-Yang, Z.-C., Stretching single-stranded DNA: Interplay of electrostatic, base-pairing, and base-pair stacking interactions. *Biophys. J.* **2001,** 81, (2), 1133-1143.

94. Tan, Z.-J.; Chen, S.-J., Nucleic acid helix stability: Effects of salt concentration, cation valence and size, and chain length. *Biophys. J.* **2006,** 90, (4), 1175-1190.

95. Zhi-Jie, T.; Shi-Jie, C., Electrostatic correlations and fluctuations for ion binding to a finite length polyelectrolyte. *J. Chem. Phys.* **2005,** 122, (4), 044903.

96. MacKerell Jr., A. D., Empirical force fields for biological macromolecules: Overview and issues. *J. Comput. Chem.* **2004,** 25, (13), 1584-1604.

97. Bustamante, C.; Marko, J. F.; Siggia, E. D.; Smith, S., Entropic elasticity of lambda-phage DNA. *Science* **1994,** 265, (5178), 1599-600.

98. Geggier, S.; Kotlyar, A.; Vologodskii, A., Temperature dependence of DNA persistence length. *Nuc. Acids Res.* **2010**, 1-8.

99. Olsthoorn, C. S. M.; Bostelaar, L. J.; De Rooij, J. F. M.; Van Boom, J. H.; Altona, C., Circular dichroism study of stacking properties of oligodeoxyadenylates and polydeoxyadenylate. *Eur. J. Biochem* **1981,** 115, (2), 309-321.

100. Tonzani, S.; Schatz, G. C., Electronic excitations and spectra in single-stranded DNA. *J. Am. Chem. Soc.* **2008,** 130, (24), 7607-7612.

101. Klenin, K.; Langowski, J., Computation of writhe in modeling of supercoiled DNA. *Biopolymers* **2000,** 54, 307-317.

102. Beard, W. A.; Wilson, S. H., Structural insights into the origins of DNA polymerase fidelity. *Structure* **2003,** 11, 489-496.

103. Brown, J. A. Kinetic mechanisms of DNA polymerases. 3438164, The Ohio State University, Ann Arbor, **2010**.

104. Florian, J.; Goodman, M. F.; Warshel, A., Free-energy perturbation calculations of DNA destabilization by base substitutions: The effect of neutral guanine.Thymine, adenine.Cytosine and adenine.Difluorotoluene mismatches. *J. Phys. Chem. B* **2000,** 104, (43), 10092-10099.

105. Johnson, S. J.; Taylor, J. S.; Beese, L. S., Processive DNA synthesis observed in a polymerase crystal suggests a mechanism for the prevention of frameshift mutations. *Proc. Natl. Acad. Sci.* **2003,** 100, (7), 3895–3900.

106. Keller, D. J.; Brozik, J. A., Framework model for DNA polymerases. *Biochemistry* **2005,** 44, 6877-6888.

107. McCulloch, S. D.; Kunkel, T. A., The fidelity of DNA synthesis by eukaryotic replicative and translesion synthesis polymerases. *Cell Res* **2008,** 18, (1), 148-161.

108. Radhakrishnan, R.; Arora, K.; Wang, Y.; Beard, W. A.; Wilson, S. H.; Schlick, T., Regulation of DNA repair fidelity by molecular checkpoints: "gates" in DNA polymerase β's substrate selection. *Biochemistry* **2006,** 45, (51), 15142-15156.

109. Johnson, K. A., Conformational coupling in polymerase fidelity. *Annu. Rev. Biochem* **1993,** 62, 685-713.

110. Arora, K.; Beard, W. A.; Wilson, S. H.; Schlick, T., Mismatch-induced conformational distortions in polymerase β support an induced-fit mechanism for fidelity. *Biochemistry* **2005,** 44, (40), 13328-13341.

111. Bebenek, K.; Abbotts, J.; Roberts, J. D.; Wilson, S. H.; Kunkel, T. A., Specificity and mechanism of error-prone replication by human immunodeficiency virus-1 reverse transcriptase. *J. Biol. Chem.* **1989,** 264, (28), 16948-16956.

112. Florian, J.; Goodman, M. F.; Warshel, A., Computer simulation of the chemical catalysis of DNA polymerases: Discriminating between alternative nucleotide insertion mechanisms for t7 DNA polymerase. *J. Am. Chem. Soc.* **2003,** 125, 8165.

113. Furge, L. L.; Guengerich , F. P., Analysis of nucleotide insertion and extension at 8-oxo-7,8-dihydroguanine by replicative t7 polymerase exo - and human immunodeficiency virus-1 reverse transcriptase using steady-state and pre-steady-state kinetics. *Biochemistry* **1997,** 36, 6475-6487.

114. Johnson, S. J.; Beese, L. S., Structures of mismatch replication errors observed in a DNA polymerase. *Cell* **2004,** 116, (6), 803-816.

115. Joyce, C. M.; Benkovic, S. J., DNA polymerase fidelity: Kinetics, structure, and checkpoints. *Biochemistry* **2004,** 43, (45).

116. Kati, W. M.; Johnson, K. A.; Jerva, L. F.; Anderson, K. S., Mechanism and fidelity of hiv reverse transcriptase. *J. Biol. Chem.* **1992,** 267, (36), 25988-25997.

117. Kiefer, J. R.; Mao, C.; Braman, J. C.; Beese, L. S., Visualizing DNA replication in a catalytically active bacillus DNA polymerase crystal. *Nature* **1998,** 391, 304-307.

118. Pop, M.; Biebricher, C. K., Kinetic analysis of pausing and fidelity of human immunodeficiency virus type 1 reverse transcriptase. *Biochemistry* **1996,** 35, 5054-5062.

119. Radhakrishnan, R.; Schlick, T., Fidelity discrimination in DNA polymerase β: Differing closing profiles for a mismatched (g:A) versus matched (g:C) base pair. *J. Am. Chem. Soc.* **2005,** 127, (38), 13245-13252.

120. Seki, M.; Masutani, C.; Yang, L. W.; Schuffert, A.; Iwai, S.; Bahar, I.; Wood, R. D., *High-efficiency bypass of DNA damage by human DNA polymerase θ*. **2004**; Vol. 23, p 4484-4494.

121. Steitz, T. A., DNA polymerases: Structural diversity and common mechanisms. *J. Biol. Chem.* **1999,** 274, (25), 17395-17398.

122. Steitz, T. A.; Yin, Y. W., Accuracy, lesion bypass, strand displacement and translocation by DNA polymerases. *Phil. Trans. R. Soc. Lond* **2003,** 359, 17-23.

123. Woodside, A. M.; Guengerich, F. P., Effect of the o6 substituent on misincorporation kinetics catalyzed by DNA polymerases at o 6 -methylguanine and o 6 -benzylguanine. *Biochemistry* **2002,** 41, 1027-1038.

124. Woodside, A. M.; Guengerich , F. P., Misincorporation and stalling at o 6 -methylguanine and o 6 -benzylguanine: Evidence for inactive polymerase complexes. *Biochemistry* **2002,** 41, 1039-1050.

125. Wu, S.; Beard, W. A.; Pedersen, L. G.; Wilson, S. H., Structural comparison of DNA polymerase architecture suggests a nucleotide gateway to the polymerase active site. *Chem. Rev.* **2013,** 114, (5), 2759-2774.

126. Beard, W. A.; Wilson, S. H., Structure and mechanism of DNA polymerase β. *Chem. Rev.* **2006,** 106, 361-382.

127. Filée, J.; Forterre, P.; Sen-Lin, T.; Laurent, J., Evolution of DNA polymerase families: Evidences for multiple gene exchange between cellular and viral proteins. *J. Mol. Evol.* **2002,** 54, (6), 763-773.

128. Seki, M.; Marini, F.; Wood, R. D., Polq (pol θ), a DNA polymerase and DNA-dependent atpase in human cells. *Nucl. Acids Res.* **2003,** 31, (21), 6117-6126.

129. Doublie, S.; Tabor, S.; Long, A. M.; Richardson, C. C.; Ellenberger, T., Crystal structure of a bacteriophage t7 DNA replication complex at 2.2 a resolution. *Nature* **1998,** 391, 251-258.

130. Wuite, G. J. L.; Smith, S. B.; Young, M.; Keller, D. J.; Bustamante, C., Single-molecule studies of the effect of template tension on t7 DNA polymerase activity. *Nature* **2000,** 404, 103-106.

131. Brieba, L. G.; Ellenberger, T., Hold tight (but not too tight) to get it right: Accurate bypass of an 8-oxoguanine lesion by DNA polymerase ß. *Structure* **2003,** 11, 1-6.

132. Pelletier, H.; Sawaya, M. R.; Wolfle, W.; Wilson, S. H.; Kraut, J., Crystal structures of human DNA polymerase beta complexed with DNA: Implications for catalytic mechanism, processivity, and fidelity. *Biochemistry* **1996,** 35, (39), 12742-12761.

133. Xiang, Y.; Goodman, M. F.; Beard, W. A.; Wilson, S. H.; Warshel, A., Exploring the role of large conformational changes in the fidelity of DNA polymerase β. *Proteins: Struct., Funct., Bioinf.* **2008,** 70, (1), 231-247.

134. Lin, P.; Pedersen, L. C.; Batra, V. K.; Beard, W. A.; Wilson, S. H.; Pedersen, L. G., Energy analysis of chemistry for correct insertion by DNA polymerase β. *Proc. Natl. Acad. Sci.* **2006,** 103, (36), 13294-13299.

135. Joyce, C. M.; Steitz, T. A., Function and structure relationships in DNA polymerases. . *Annu. Rev. Biochem* **1994,** 63, 777-822.

136. Beese, L. S.; Derbyshire, V.; Steitz, T. A., Structure of DNA polymerase i klenow fragment bound to duplex DNA. *Science* **1993,** 260, 352-355.

137. Jacobo-Molina, A.; Ding, J.; Nanni, R. G.; Clark, A. D.; Lu, X.; Tantillo, C.; Williams, R. L.; Kamer, G.; Ferris, A. L.; Clark, P., Crystal structure of human immunodeficiency virus type 1 reverse transcriptase complexed with double-stranded DNA at 3.0 a resolution shows bent DNA. *Proc. Natl. Acad. Sci.* **1993,** 90, (13), 6320-6324.

138. Kim, Y.; Eom, S. H.; Wang, D. L.; Suh, S. W.; Steitz, T. A., Crystal structure of thermus aquaticus DNA polymerase. *Nature* **1995,** 376, 612-616

139. Lu, H.; Macosko, J.; Habel-Rodriguez, D.; Keller, R. W.; Brozik, J. A.; Keller, D. J., Closing of the fingers domain generates motor forces in the hiv reverse transcriptase. *J. Biol. Chem.* **2004,** 279, (52), 54529-54532.

140. Yin, Y. W.; Steitz, T. A., The structural mechanism of translocation and helicase activity in t7 rna polymerase. *Cell* **2004,** 116, 393–404.

141. Deval, J.; Navarro, J. M.; Selmi, B.; Courcambeck, J.; Boretto, J.; Halfon, P.; Garrido-Urbani, S.; Sire, J.; Canard, B., A loss of viral replicative capacity correlates with altered DNA polymerization kinetics by the human immunodeficiency virus reverse transcriptase bearing the k65r and l74v dideoxynucleoside resistance substitutions *J. Biol. Phys.* **2004,** 279, 25489-25496.

142. Florian, J.; Goodman, M.; Warshel, A., Computer simulation studies of the fidelity of DNA polymerases. *Biopolymers* **2003,** 68, 286-299.

143. Furge, L. L.; Guengerich , F. P., Explanation of pre-steady-state kinetics and decreased burst amplitude of hiv-1 reverse transcripate at sites of modified DNA bases with an additional nonproductive enzyme-DNA-nucleotide complex. *Biochemistry* **1999,** 38, 4818-4825.

144. Furman, P. A.; Painter, G. R.; Anderson, K. S., An analysis of the catalytic cycle of hiv-1 reverse transcriptase: Opportunities for chemotheraputic intervention based on enzyme inhibition. *Curr. Pharm. Des.* **2000,** 6, 547-567.

145. Hsieh, J.; Zinnen, S.; Modrich, P., Kinetic mechanism of the DNA-dependent DNA polymerase activity of human immunodeficiency virus reverse transcriptase. *J. Biol. Chem.* **1993,** 268, 24607-24613.

146. Madrid, M.; Lukin, J. A.; Madura, J. D.; Ding, J.; Arnold, E., Molecular dynamics of hiv-1 reverse transcriptase indicates increased flexibility upon DNA binding. *Proteins: Struct. Funct. Genet.* **2001,** 45, 176-182.

147. Ortiz, T. P.; Marshall, J. A.; Meyer, L. A.; Davis, R. W.; Macosko, J.; Keller, D. J.; Brozik, J. A., Stepping statistics of single hiv-1 reverse transcriptase molecules during DNA polymerization. *J. Phys. Chem. B* **2005,** 109, 16127-16131.

148. Rungrotmongkol, T.; Hannongbua, S.; Mulholland, A., Mechanistic study of hiv-1 reverse transcriptase at the active site based on qm/mm method. *J. Theor & Comp. Chem.* **2004,** 3, 491-500.

149. Sarafianos, S. G.; Clark, A. D.; Tuske, S.; Squire, C.; Das, K.; Sheng, D.; Ilankumaran, P.; Ramesha, A. R.; Kroth, H.; Sayer, J. M.; Jerina, D. M.; Boyer, P. L.; Hughes, S. H.; Arnold, E., Trapping hiv-1 reverse transcriptase before and after translocation on DNA. *J. Biol. Chem.* **2003,** 278, (18), 16280–16288.

150. Wohrl, B. M.; Krebs, R.; Thralli, S. H.; Le Grice, S. F. J.; Scheidig, A. J.; Goody, R. S., Kinetic analysis of four hiv-1 reverse transcriptase enzymes mutated in the primer grip region of p66 *J. Biol. Chem.* **1997,** 272, (28), 17581–17587.

151. Castro, C.; Smidansky, E.; Maksimchuk, K. R.; Arnold, J. J.; Korneeva, V. S.; Götte, M.; Konigsberg, W.; Cameron, C. E., Two proton transfers in the transition state for nucleotidyl transfer catalyzed by rna- and DNA-dependent rna and DNA polymerases. *Proc. Natl. Acad. Sci.* **2007,** 104, (11), 4267-4272.

152. Bustamante, C.; Keller, D. J.; Oster, G., The physics of molecular motors. *Acc. Chem. Res* **2001,** 34, 412-420.

153. Dessinges, M. N.; Maier, B.; Zhang, Y.; Peliti, M.; Bensimon, D.; Croquette, V., Stretching single stranded DNA, a model polyelectrolyte. *Phys. Rev. Lett.* **2002,** 89, (24).

154. Keller, D. J.; Bustamante, C., Mechanochemistry of molecular motors. *Biophys. J.* **1999,** 78, 541-556.

155. Kerr, S. G.; Anderson, K. S., Pre-steady-state kinetic characterization of wild type and 3-azido-3-deoxythymidine (azt) resistant human immunodeficiency virus type 1 reverse transcriptase: Implication of rna directed DNA polymerization in the mechanism of azt resistance. *Biochemistry* **1997,** 36, 14064-14070.

156. Krebs, R.; Immendorfer, U.; Thrall, S. H.; Wohrl, B. M.; Goody, R. S., Single-step kinetics of hiv-1 reverse transcriptase mutants responsible for virus resistance to nucleoside inhibitors zidovudine and 3-tc. *Biochemistry* **1997,** 36, 10292-10300.

157. Patel, S. S.; Wong, I.; Johnson, K. A., Pre-steady-state kinetic analysis of processive DNA replication including complete characterization of an exonuclease-deficient mutant. *Biochemistry* **1991,** 30, (2), 511-525.

158. Jeffrey, J. L.; Feng, J. Y.; Richard, C. C.; Anderson, K. S.; Furman, P. A., Dioxolane guanosine 5-triphosphate, an alternative substrate inhibitor of wild-type and mutant hiv-1 reverse transcriptase. *J. Biol. Chem.* **2003,** 278, (21), 18971–18979.

159. Marchand, B.; Gotte, M., Site-specific footprinting reveals differences in the translocation status of hiv-1 reverse transcriptase - implications for polymerase translocation and drug resistance. *J. Biol. Chem.* **2003,** 278, 35362-35372.

160. Cazals, F.; Dreyfus, T., Multi-scale geometric modeling of ambiguous shapes with : Oleranced balls and compoundly weighted α-shapes. *Comput. Graph Forum* **2010,** 29, (5), 1713-1722.

161. Cazals, F.; Dreyfus, T.; Sachdeva, S.; Nisarg, S. *Greedy geometric optimization algorithms for collection of balls*; Carnegie Mellon University **2013**; p 36.

162. Jüttler, B.; Poteaux, A.; Song, X., Medial axis computation using a hierarchical spline approximation of the signed distance function. In *FSP Report No. 105*, Technical report: Industrial Geometry, **2010**.

163. Huang, H.; Chopra, R.; Verdine, G. L.; Harrison, S. C., Structure of a covalently trapped catalytic complex of hiv-1 reverse transcriptase: Implications for drug resistance. *Science* **1998,** 282, (5394), 1669-1675.

164. Can, T.; Chen, C.-I.; Wang, Y.-F., Efficient molecular surface generation using level-set methods. *J. Mol. Graphics Modell.* **2006,** 25, (4), 442-454.

165. Pettersen, E. F.; Goddard, T. D.; Huang, C. C.; Couch, G. S.; Greenblatt, D. M.; Meng, E. C.; Ferrin, T. E., Ucsf chimera—a visualization system for exploratory research and analysis. *J. Comput. Chem.* **2004,** 25, (13), 1605-1612.

166. Richards, F. M., Areas, volumes, packing, and protein structure. *Annu. Rev. Biophys. Bioeng.* **1977,** 6, (1), 151-176.

167. Goddard, T. Solvent accessible surface area. http://www.cgl.ucsf.edu/chimera/data/sasa-nov2013/sasa.html (November 17, 2014),

168. Goler, A.; Brozik, J. A.; Keller, D., Functional properties of hiv1 reverse transcriptase from the anisotropic network model and essential dynamics. *J. Phys. Chem. B* **In Prep**.

169. Bahar, I.; Atilgan, A. R.; Erman, B., Direct evaluation of thermal fluctuations in proteins using a single-parameter harmonic potential. *Fold. Des.* **1997,** 2, (3), 173-181.

170. Tirion, M. M., Large amplitude elastic motions in proteins from a single-parameter, atomic analysis. *Physical Review Letters* **1996,** 77, (9), 1905-1908.

171. Haider, S.; Parkinson, G. N.; Neidle, S., Molecular dynamics and principal components analysis of human telomeric quadruplex multimers. *Biophys. J.* **2008,** 95, (1), 296-311.

172. Rueda, M.; Chacón, P.; Orozco, M., Thorough validation of protein normal mode analysis: A comparative study with essential dynamics. *Structure* **2007,** 15, (5), 565-575.

173. Amadei, A.; Linssen, A. B. M.; Berendsen, H. J. C., Essential dynamics of proteins. *Proteins: Structure, Function and Genetics* **1993,** 17, 412-425.

174. Atilgan, A. R.; Durell, S. R.; Jernigan, R. L.; Demirel, M. C.; Keskin, O.; Bahar, I., Anisotropy of fluctuation dyanmics of proteins with an elastic network model. *Biophysical Journal* **2001,** 80, 505-515.

175. Bahar, I.; Atilgan, A. R.; Erman, B., Direct evaluation of thermal fluctuations in proteins using a single-parameter harmonic potential. *Folding and Design* **1997,** 2, (3), 173-181.

176. Bahar, I.; Erman, B.; Jernigan, R. L.; Atilgan, A. R.; Covell, D. G., Collective motions in hiv-1 reverse transcriptase: Examination of flexibility and enzyme function. *J. Mol. Biol.* **1999,** 285, 1023-1037.

177. Delarue, M.; Sanejouand, Y. H., Simplified normal mode analysis of conformational transitions in DNA-dependent polymerases: The elastic network model. *J. Mol. Biol.* **2002,** 320, (5), 1011-1024.

178. Eichinger, B. E., Elasticity theory. I. Distribution functions for perfect phantom networks. *Macromolecules* **1972,** 5, (4), 496-505.

179. Eyal, E.; Yang, L.-W.; Bahar, I., Anisotropic network model: Systematic evaluation and a new web interface. *Bioinformatics* **2006,** 22, (21), 2619-2627.

180. Hinsen, K., Analysis of domain motions by approximate normal mode calculations. *Proteins: Structure, Function and Genetics* **1998,** 33, 417-429.

181. Rueda, M.; Cha\'con, P.; Orozco, M., Thorough validation of protein normal mode analysis: A comparative study with essential dynamics. *Structure* **2007,** 15, 565-575.

182. *Antimicrobial resistance: Global report on surveillance 2014*; World Health Organization: April **2014**; p 257.

183. Song, X.; Cogen, J.; Singh, N., Incidence of methicillin-resistant staphylococcus aureus infection in a children/'s hospital in the washington metropolitan area of the united states, 2003 - 2010. *Emerg. Microbes. Infect.* **2013,** 2, e69.

184. Lu, L.; Rininsland, F. H.; Wittenburg, S. K.; Achyuthan, K. E.; McBranch, D. W.; Whitten, D. G., Biocidal activity of a light-absorbing fluorescent conjugated polyelectrolyte *Langmuir* **2005,** 21, (22), 10154-10159.

185. Pappas, H. C.; Lovchik, J. A.; Whitten, D. G., Assessing the sporicidal activity of oligo-p-phenylene ethynylenes and their role as bacillus germinants. *Langmuir* **Submitted**.

186. Wang, Y.; Canady, T. D.; Zhou, Z.; Tang, Y.; Price, D. N.; Bear, D. G.; Chi, E. Y.; Schanze, K. S.; Whitten, D. G., Cationic phenylene ethynylene polymers and oligomers exhibit efficient antiviral activity. *ACS Appl. Mater. Interfaces* **2011,** 3, (7), 2209-2214.

187. Wang, Y.; Schanze, K. S.; Chi, E. Y.; Whitten, D. G., When worlds collide: Interactions at the interface between biological systems and synthetic cationic conjugated polyelectrolytes and oligomers. *Langmuir* **2013,** 29, (34), 10635-10647.

188. Wilde, K. N. In vitro cytotoxicity and skin irritation testing of antimicrobial conjugated electrolytes: Interactions with mammalian cells. University of New Mexico, Albuquerque, NM, **2012**.

189. Wang, Y. Antimicrobial activity and mechanistic study for the poly(phenylene ethynylene) (ppe)-based cationic conjugated polyelectrolytes and oligo-phenylene ethynylenes. University of New Mexico, Albuquerque, NM, **2013**.

190. Corbitt, T. S.; Ding, L.; Ji, E.; Ista, L. K.; Ogawa, K.; López, G. P.; Schanze, K. S.; Whitten, D. G., Light and dark biocidal activity of cationic poly(arylene ethynylene) conjugated polyelectrolytes. *Photochem. Photobiol. Sci.* **2009,** 8, (7), 998-1005.

191. Chemburu, S.; Corbitt, T. S.; Ista, L. K.; Ji, E.; Fulghum, J.; López, G. P.; Ogawa, K.; Schanze, K. S.; G. Whitten, D., Light-induced biocidal action of conjugated polyelectrolytes supported on colloids. *Langmuir* **2008,** 24, (19), 11053-11062.

192. Funston, A. M.; Silverman, E. E.; Schanze, K. S.; Miller, J. R., Spectroscopy and transport of the triplet exciton in a terthiophene end-capped poly(phenylene ethynylene). *J. Phys. Chem. B* **2006,** 110, (36), 17736-17742.

193. Walters, K. A.; Dattelbaum, D. M.; Ley, K. D.; Schoonover, J. R.; Meyer, T. J.; Schanze, K. S., Photophysics of phenyleneethynylene metal-organic oligomers. Probing the lowest excited state by time-resolved ir spectroscopy. *Chem. Commun.* **2001**, (18), 1834-1835.

194. Ji, E.; Corbitt, T. S.; Parthasarathy, A.; Schanze, K. S.; Whitten, D. G., Light and dark-activated biocidal activity of conjugated polyelectrolytes. *ACS Appl. Mater. Interfaces* **2011,** 3, (8), 2820-2829.

195. Dahl, T. A.; Midden, W. R.; Hartman, P. E., Comparison of killing of gram-negative and gram-positive bacteria by pure singlet oxygen. *J. Bacteriol.* **1989,** 171, (4), 2188-2194.

196. Davies, M. J., Singlet oxygen-mediated damage to proteins and its consequences. *Biochem. Biophys. Res. Commun.* **2003,** 305, (3), 761-770.

197. Xing, C.; Xu, Q.; Tang, H.; Liu, L.; Wang, S., Conjugated polymer/porphyrin complexes for efficient energy transfer and improving light-activated antibacterial activity. *J. Am. Chem. Soc.* **2009,** 131, (36), 13117-13124.

198. Beveridge, T. J., Structures of gram-negative cell walls and their derived membrane vesicles. *J. Bacteriol.* **1999,** 181, (16), 4725-4733.

199. Beveridge, T. J.; Graham, L. L., Surface layers of bacteria. *Microbiol Rev* **1991,** 55, (4), 684-705.

200. Neuhaus, F. C.; Baddiley, J., A continuum of anionic charge: Structures and functions of d-alanyl-teichoic acids in gram-positive bacteria. *Microbiol. Mol. Biol. Rev.* **2003,** 67, (4), 686-723.

201. Young, K. D., Bacterial cell wall. In *Els*, John Wiley & Sons, Ltd: **2001**.

202. Archibald, A. R.; Armstrong, J. J.; Baddiley, J.; Hay, J. B., Teichoic acids and the structure of bacterial walls. *Nature* **1961,** 191, (4788), 570-572.

203. Armstrong, J. J.; Baddiley, J.; Buchanan, J. G.; Carss, B., Nucleotides and the bacterial cell wall. *Nature* **1958,** 181, (4625), 1692-1693.

204. Armstrong, J. J.; Baddiley, J.; Buchanan, J. G.; Davison, A. L.; Kelemen, M. V.; Neuhaus, F. C., Teichoic acids from bacterial walls: Composition of teichoic acids from a number of bacterial walls. *Nature* **1959,** 184, (4682), 247-248.

205. Doyle, R. J.; McDannel, M. L.; Streips, U. N.; Birdsell, D. C.; Young, F. E., Polyelectrolyte nature of bacterial teichoic acids. *J. Bacteriol.* **1974,** 118, (2), 606-615.

206. Hill, E. H.; Whitten, D. G.; Evans, D. G., Computational study of bacterial membrane disruption by cationic biocides: Structural basis for water pore formation. *J. Phys. Chem. B* **2014,** 118, (32), 9722-9732.

207. Meroueh, S. O.; Bencze, K. Z.; Hesek, D.; Lee, M.; Fisher, J. F.; Stemmler, T. L.; Mobashery, S., Three-dimensional structure of the bacterial cell wall peptidoglycan. *Proc. Natl. Acad. Sci. U. S. A.* **2006,** 103, (12), 4404-4409.

208. Umeda, A.; Ueki, Y.; Amako, K., Structure of the staphylococcus aureus cell wall determined by the freeze-substitution method. *J. Bacteriol.* **1987,** 169, (6), 2482-2487.

209. Gross, M.; Cramton, S. E.; Götz, F.; Peschel, A., Key role of teichoic acid net charge instaphylococcus aureus colonization of artificial surfaces. *Infect. Immun.* **2001,** 69, (5), 3423-3426.

210. Swoboda, J. G.; Campbell, J.; Meredith, T. C.; Walker, S., Wall teichoic acid function, biosynthesis, and inhibition. *ChemBioChem* **2010,** 11, (1), 35-45.

211. Doyle, R. J.; Chatterjee, A. N.; Streips, U. N.; Young, F. E., Soluble macromolecular complexes involving bacterial teichoic acids. *J. Bacteriol.* **1975,** 124, (1), 341-347.

212. Heptinstall, S.; Archibald, A. R.; Baddiley, J., Teichoic acids and membrane function in bacteria. *Nature* **1970,** 225, (5232), 519-521.

213. Knox, K. W.; Wicken, A. J., Immunological properties of teichoic acids. *Bacteriol. Rev.* **1973,** 37, (2), 215-257.

214. Sanderson, A. R.; Strominger, J. L.; Nathenson, S. G., Chemical structure of teichoic acid from staphylococcus aureus, strain copenhagen. *J. Bio. Chem.* **1962,** 237, (12), 3603-3613.

215. Schäffer, C.; Messner, P., The structure of secondary cell wall polymers: How gram-positive bacteria stick their cell walls together. *Microbiology* **2005,** 151, (3), 643-651.

216. Vinogradov, E.; Sadovskaya, I.; Li, J.; Jabbouri, S., Structural elucidation of the extracellular and cell-wall teichoic acids of staphylococcus aureus mn8m, a biofilm forming strain. *Carbohydr. Res.* **2006,** 341, (6), 738-743.

217. Ward, J. B., Teichoic and teichuronic acids - biosynthesis, assembly, and location. *Microbiol. Rev.* **1981,** 45, (2), 211-243.

218. Eaton, P.; Fernandes, J. o. C.; Pereira, E. l.; Pintado, M. E.; Xavier Malcata, F., Atomic force microscopy study of the antibacterial effects of chitosans on escherichia coli and staphylococcus aureus. *Ultramicroscopy* **2008,** 108, (10), 1128-1134.

219. Bayer, M. E.; Thurow, H., Polysaccharide capsule of escherichia coli: Microscope study of its size, structure, and sites of synthesis. *J. Bacteriol.* **1977,** 130, (2), 911-936.

220. Sleytr, U. B.; Beveridge, T. J., Bacterial s-layers. *Trends Microbiol.* **1999,** 7, (6), 253-260.

221. Wang, Y.; Zhou, Z.; Zhu, J.; Tang, Y.; Canady, T. D.; Chi, E. Y.; Schanze, K. S.; Whitten, D. G., Dark antimicrobial mechanisms of cationic phenylene ethynylene polymers and oligomers against escherichia coli. *Polymers* **2011,** 3, (3), 1199-1214.

222. Corbitt, T. S.; Zhou, Z.; Tang, Y.; Graves, S. W.; Whitten, D. G., Rapid evaluation of the antibacterial activity of arylene-ethynylene compounds. *ACS Appl. Mater. Interfaces* **2011,** 3, (8), 2938-2943.

223. Shatalin, K.; Gusarov, I.; Avetissova, E.; Shatalina, Y.; McQuade, L. E.; Lippard, S. J.; Nudler, E., Bacillus anthracis-derived nitric oxide is essential for pathogen virulence and survival in macrophages. *Proc. Natl. Acad. Sci. U.S.A.* **2008,** 105, (3), 1009-1013.

224. Holty, J.-E. C.; Bravata, D. M.; Liu, H.; Olshen, R. A.; McDonald, K. M.; Owens, D. K., Systematic review: A century of inhalational anthrax cases from 1900 to 2005. *Ann. Intern. Med.* **2006,** 144, (4), 270-280.

225. Choudhury, B.; Leoff, C.; Saile, E.; Wilkins, P.; Quinn, C. P.; Kannenberg, E. L.; Carlson, R. W., The structure of the major cell wall polysaccharide of bacillus anthracis is species-specific. *J. Bio. Chem.* **2006,** 281, (38), 27932-27941.

226. Turnbull, P. C. B., Bacillus. In *Medical microbiology*, 4th ed.; Baron, S., Ed. University of Texas Medical Branch at Galveston: Galveston, TX, **1996**.

227. Welkos, S. L.; Friedlander, A. M., Pathogenesis and genetic control of resistance to the sterne strain of bacillus anthracis. *Microb. Pathog.* **1988,** 4, (1), 53-69.

228. Henriques, A. O.; Moran Jr, C. P., Structure and assembly of the bacterial endospore coat. *Methods* **2000,** 20, (1), 95-110.

229. Goldstein, A. L.; McCusker, J. H., Development of saccharomyces cerevisiae as a model pathogen: A system for the genetic identification of gene products required for survival in the mammalian host environment. *Genetics* **2001,** 159, (2), 499-513.

230. Klis, F. M.; Mol, P.; Hellingwerf, K.; Brul, S., Dynamics of cell wall structure in saccharomyces cerevisiae. *FEMS Microbiol. Lett.* **2002,** 26, (3), 239-256.

231. Lesage, G.; Bussey, H., Cell wall assembly in saccharomyces cerevisiae. *Microbiol. Mol. Biol. Rev.* **2006,** 70, (2), 317-343.

232. Wang, Y.; Chi, E. Y.; Natvig, D. O.; Schanze, K. S.; Whitten, D. G., Antimicrobial activity of cationic conjugated polyelectrolytes and oligomers against saccharomyces cerevisiae vegetative cells and ascospores. *ACS Appl. Mater. Interfaces* **2013,** 5, (11), 4555-4561.

233. Allison, D. G., The biofilm matrix. *Biofouling* **2003,** 19, (2), 139 - 150.

234. Dascier, D.; Ji, E.; Parthasarathy, A.; Schanze, K. S.; Whitten, D. G., Efficacy of end-only-functionalized oligo(arylene-ethynylene)s in killing bacterial biofilms. *Langmuir* **2012,** 28, (31), 11286-11290.

235. Wilde, K. N.; Whitten, D. G.; Canavan, H. E., In vitro cytotoxicity of antimicrobial conjugated electrolytes: Interactions with mammalian cells. *ACS Appl. Mater. Interfaces* **2013,** 5, (19), 9305-9311.

236. Ista, L. K.; Perez-Luna, V. H.; López, G. P., Surface-grafted, environmentally sensitive polymers for biofilm release. *Appl. Environ. Microbiol.* **1999,** 65, (4), 1603-1609.

237. Shivapooja, P.; Ista, L. K.; Canavan, H. E.; López, G. P., Arget-atrp synthesis and characterization of pnipaam brushes for quantitative cell detachment studies. *Biointerphases* **2012,** 7, (1-4), 32.

238. Yu, Q.; Cho, J.; Shivapooja, P.; Ista, L. K.; López, G. P., Nanopatterned smart polymer surfaces for controlled attachment, killing, and release of bacteria. *ACS Appl. Mater. Interfaces* **2013,** 5, (19), 9295-9304.

239. Ista, L. K.; Mendez , S.; López, G. P., Attachment and detachment of bacteria on surfaces with tunable and switchable wettability. *Biofouling* **2009,** 26, (1), 111-118.

240. Wang, Y.; Jones, E. M.; Tang, Y.; Ji, E.; López, G. P.; Chi, E. Y.; Schanze, K. S.; Whitten, D. G., Effect of polymer chain length on membrane perturbation activity of cationic phenylene ethynylene oligomers and polymers. *Langmuir* **2011,** 27, (17), 10770-10775.

241. Yu, Q.; Ista, L. K.; López, G. P., Nanopatterned antimicrobial enzymatic surfaces combining biocidal and fouling release properties. *Nanoscale* **2014,** 6, (9), 4750-4757.

242. Capeluto, M. G.; Vaschenko, G.; Grisham, M.; Marconi, M. C.; Luduena, S.; Pietrasanta, L.; Yunfeng, L.; Parkinson, B.; Menoni, C. S.; Rocca, J. J., Nanopatterning with interferometric lithography using a compact λ=46.9-nm laser. *IEEE Trans Nanotechnol.* **2006,** 5, (1), 3-7.

243. Palmer, J.; Flint, S.; Brooks, J., Bacterial cell attachment, the beginning of a biofilm. *J. Ind. Microbiol. Biotechnol* **2007,** 34, (9), 577-588.

244. Petrova, O. E.; Sauer, K., Sticky situations: Key components that control bacterial surface attachment. *Journal of Bacteriology* **2012,** 194, (10), 2413-2425.

245. Cooperstein, M. A.; Canavan, H. E., Biological cell detachment from poly(n-isopropyl acrylamide) and its applications. *Langmuir* **2009,** 26, (11), 7695-7707.

246. Ishida, N.; Kobayashi, M., Interaction forces measured between poly(n-isopropylacrylamide) grafted surface and hydrophobic particle. *J. Colloid Interface Sci.* **2006,** 297, (2), 513-519.

247. Ista, L. K.; Mendez, S.; Balamurugan, S. S.; Balamurugan, S.; Rama Rao, V. G.; López, G. P., Smart surfaces for the control of bacterial attachment and biofilm accumulation. In *Smart coatings ii*, American Chemical Society: **2009**; Vol. 1002, pp 95-110.

248. Yu, Q.; Ge, W.; Atewologun, A.; Stiff-Roberts, A. D.; López, G. P., Antimicrobial and bacteria-releasing multifunctional surfaces: Oligo (p-phenylene-ethynylene)/poly (n-isopropylacrylamide) films deposited by rir-maple. *Colloids Surf., B* **2015,** 126, (0), 328-334.

249. Jayathilake, P. G.; Khoo, B. C.; Zhijun, T., Capsule-substrate adhesion in the presence of osmosis by the immersed interface method. *World. Acad. Sci. Eng. Technol.* **2009,** 36, 412 - 421.

250. Liu, K. K.; Chan, V.; Zhang, Z., Capsule-substrate contact deformation: Determination of adhesion energy. *Med. Biol. Eng. Comput.* **2002,** 40, (4), 491-495.

251. Liu, K.-K.; Foo, J.-J.; Chan, V., Contact deformation of liposome in the presence of osmosis. *Ann. Biomed. Eng.* **2003,** 31, (10), 1279-1286.

252. Liu, P.; Zhang, Y. W.; Cheng, Q. H.; Lu, C., Simulations of the spreading of a vesicle on a substrate surface mediated by receptor-ligand binding. *J. Mech. Phys. Solids* **2007,** 55, (6), 1166-1181.

253. Pauchard, L.; Rica, S., Contact and compression of elastic spherical shells: The physics of a'ping-pong' ball. *Philos. Mag. B* **1998,** 78, (2), 225-233.

254. Shi, J. Adhesion-detachment mechanics of thin shells in the presence of intrinsic surface forces. Northeastern University, Boston, MA, USA, **2012**.

255. Wan, K. T.; Liu, K. K., Contact mechanics of a thin-walled capsule adhered onto a rigid planar substrate. *Med. Biol. Eng. Comput.* **2001,** 39, (5), 605-608.

256. *Bacterial adhesion: Molecular and ecological diversity*. Wiley-Liss Inc.: **1996**; p 361.

257. Norouzi, D.; Muller, M. M.; Deserno, M., How to determine local elastic properties of lipid bilayer membranes from atomic-force-microscope measurements: A theoretical analysis. *Phys. Rev. E: Stat., Nonlinear, Soft Matter Phys.* **2006,** 74, (6), 061914-12.

258. Bennig, G. K., Atomic force microscope and method for imaging surfaces with atomic resolution. In Google Patents: **1988**.

259. Binnig, G.; Quate, C. F.; Gerber, C., Atomic force microscope. *Phys. Rev. Lett.* **1986,** 56, (9), 930-933.

260. Binnig, G. Nobel lecture: Scanning tunneling microscopy – from birth to adolescence. http://www.nobelprize.org/nobel_prizes/physics/laureates/1986/binnig-lecture.html (11 Aug **2014**),

261. Giessibl, F. J., Atomic resolution of the silicon (111)-(7x7) surface by atomic force microscopy. *Science* **1995,** 267, (5194), 68-71.

262. Giessibl, F. J., Advances in atomic force microscopy. *Rev. Mod. Phys.* **2003,** 75, (3), 949-983.

263. Afm/lfm instruction manual. In Group, V. M., Ed. **1999**; Vol. 4.22ce.

264. Miyahara, Y.; Fujii, T.; Watanabe, S.; Tonoli, A.; Carabelli, S.; Yamada, H.; Bleuler, H., Lead zirconate titanate cantilever for noncontact atomic force microscopy. *Appl. Surf. Sci.* **1999,** 140, (3-4), 428-431.

265. Haugstad, G., *Atomic force microscopy*. John Wiley and Sons: Hoboken, New Jersey, USA, **2012**.

266. Morris, V. J.; Kirby, A. R.; Gunning, A. P., *Atomic force microscopy for biologists*. 1st ed.; Imperial College Press: London, **1999**; p 332.

267. Hutter, J. L.; Bechhoefer, J., Calibration of atomic-force microscope tips. *Rev. Sci. Instrum.* **1993,** 64, (7), 1868-1873.

268. Alves, C. S.; Melo, M. N.; Franquelim, H. G.; Ferre, R.; Planas, M.; Feliu, L.; Bardaji, E.; Kowalczyk, W.; Andreu, D.; Santos, N. C.; Fernandes, M. X.; Castanho, M. A. R. B., Escherichia coli cell surface perturbation and disruption induced by antimicrobial peptides bp100 and pepr. *J. Bio. Chem.* **2010,** 285, (36), 27536-27544.

269. Dufrêne, Y. F., Application of atomic force microscopy to microbial surfaces: From reconstituted cell surface layers to living cells. *Micron* **2001,** 32, (2), 153-165.

270. Dufrêne, Y. F.; Boonaert, C. J. P.; van der Mei, H. C.; Busscher, H. J.; Rouxhet, P. G., Probing molecular interactions and mechanical properties of microbial cell surfaces by atomic force microscopy. *Ultramicroscopy* **2001,** 86, 113-120.

271. Vadillo-Rodriguez, V.; Beveridge, T. J.; Dutcher, J. R., Surface viscoelasticity of individual gram-negative bacterial cells measured using atomic force microscopy. *J. Bacteriol.* **2008,** 190, (12), 4225-4232.

272. Velegol, S. B.; Logan, B. E., Contributions of bacterial surface polymers, electrostatics, and cell elasticity to the shape of afm force curves. *Langmuir* **2002,** 18, (13), 5256-5262.

273. Wang, Y.; Jett, S. D.; Crum, J.; Schanze, K. S.; Chi, E. Y.; Whitten, D. G., Understanding the dark and light-enhanced bactericidal action of cationic conjugated polyelectrolytes and oligomers. *Langmuir* **2012,** 29, (2), 781-792.

274. Zhao, X.; Pinto, M. R.; Hardison, L. M.; Mwaura, J.; Müller, J.; Jiang, H.; Witker, D.; Kleiman, V. D.; Reynolds, J. R.; Schanze, K. S., Variable band gap poly(arylene ethynylene) conjugated polyelectrolytes. *Macromolecules* **2006,** 39, (19), 6355-6366.

275. Zhou, Z.; Corbitt, T. S.; Parthasarathy, A.; Tang, Y.; Ista, L. K.; Schanze, K. S.; Whitten, D. G., "end-only" functionalized oligo(phenylene ethynylene)s:Synthesis, photophysical and biocidal activity. *J. Phys. Chem. Lett.* **2010,** 1, (21), 3207-3212.

276. Louise Meyer, R.; Zhou, X.; Tang, L.; Arpanaei, A.; Kingshott, P.; Besenbacher, F., Immobilisation of living bacteria for afm imaging under physiological conditions. *Ultramicroscopy* **2010,** 110, (11), 1349-1357.

277. Nanoscope *Nanoscope software* 531r1; Veeco Instruments Inc: **2004**.

278. Amro, N. A.; Kotra, L. P.; Wadu-Mesthrige, K.; Bulychev, A.; Mobashery, S.; Liu, G.-y., High-resolution atomic force microscopy studies of the escherichia coli outer membrane: Structural basis for permeability. *Langmuir* **2000,** 16, (6), 2789-2796.

279. Meincken, M.; Holroyd, D. L.; Rautenbach, M., Atomic force microscopy study of the effect of antimicrobial peptides on the cell envelope of escherichia coli. *Antimicrob. Agents Chemother.* **2005,** 49, (10), 4085-4092.

280. Peng, L.; Yi, L.; Zhexue, L.; Juncheng, Z.; Jiaxin, D.; Daiwen, P.; Ping, S.; Songsheng, Q., Study on biological effect of la3+ on escherichia coli by atomic force microscopy. *J. Inorg. Biochem.* **2004,** 98, (1), 68-72.

281. Razatos, A.; Ong, Y.-L.; Sharma, M. M.; Georgiou, G., Molecular determinants of bacterial adhesion monitored by atomic force microscopy. *Proc. Natl. Acad. Sci. U. S. A.* **1998,** 95, (19), 11059-11064.

282. Mari, S. A.; Köster, S.; Bippes, C. A.; Yildiz, Ö.; Kühlbrandt, W.; Muller, D. J., Ph-induced conformational change of the î²-barrel-forming protein ompg reconstituted into native e. Coli lipids. *J. Mol. Biol.* **2010,** 396, (3), 610-616.

283. Schabert, F. A.; Engel, A., Reproducible acquisition of escherichia coli porin surface topographs by atomic force microscopy. *Biophys. J.* **1994,** 67, (6), 2394-2403.

284. Schabert, F. A.; Henn, C.; Engel, A., Native escherichia coli ompf porin surfaces probed by atomic force microscopy. *Science* **1995,** 268, (5207), 92-94.

285. Scientific Instrument Services, I. Santovac 5 polyphenyl ether vacuum pump fluid. http://www.sisweb.com/vacuum/sis/satovc5p.htm (Feb. 12, **2014**),

286. Kasas, S.; Ikai, A., A method for anchoring round shaped cells for atomic force microscope imaging. *Biophys. J.* **1995,** 68, (5), 1678-1680.

287. Touhami, A.; Jericho, M. H.; Beveridge, T. J., Atomic force microscopy of cell growth and division in staphylococcus aureus. *J. Bacteriol.* **2004,** 186, (11), 3286-3295.

288. Colom, A.; Casuso, I.; Rico, F.; Scheuring, S., A hybrid high-speed atomic force optical microscope for visualizing single membrane proteins on eukaryotic cells. *Nat. Commun.* **2013,** 4.

289. Fantner, G. E.; Barbero, R. J.; Gray, D. S.; Belcher, A. M., Kinetics of antimicrobial peptide activity measured on individual bacterial cells using high-speed atomic force microscopy. *Nat. Nano.* **2010,** 5, (4), 280-285.

290. Hammer, M. U.; Brauser, A.; Olak, C.; Brezesinski, G.; Goldmann, T.; Gutsmann, T.; Andrä, J., Lipopolysaccharide interaction is decisive for the activity of the antimicrobial peptide nk-2 against escherichia coli and proteus mirabilis. *Biochem. J.* **2010,** 427, (3), 477-488.

291. Wang, Y.; Corbitt, T. S.; Jett, S. D.; Tang, Y.; Schanze, K. S.; Chi, E. Y.; Whitten, D. G., Direct visualization of bactericidal action of cationic conjugated polyelectrolytes and oligomers. *Langmuir* **2011,** 28, (1), 65-70.

292. Hill, E. H.; Stratton, K.; Whitten, D. G.; Evans, D. G., Molecular dynamics simulation study of the interaction of cationic biocides with lipid bilayers: Aggregation effects and bilayer damage. *Langmuir* **2012,** 28, (42), 14849-14854.

293. Li, Y.; Guo, H., Atomistic simulations of an antimicrobial molecule interacting with a model bacterial membrane. *Theor.Chem. Acc.* **2013,** 132, (1), 1-8.

294. Pappas, H. C.; Edens, L. E.; Yoon, S.; Phan, S.; Meng, X.; Keller, D. J.; Schanze, K. S.; Whitten, D. G., Synthesis, characterization, and biocidal activities of mixed poly(phenylene-ethynylene)/poly(n-isopropylacrylamide) multifunctional surfaces. *Langmuir* **In Prep.**